Singlet fission in linear π-conjugated systems



Darren Valentine

Thesis submitted for the degree of Doctor of Philosophy

Balliol College, University of Oxford

Trinity 2020

Declaration of Authorship

The work presented in this thesis is my own, except where otherwise stated. No part of this thesis has been submitted for any other degree at this or any other university.

Darren Valentine

August 2020

Abstract

Singlet fission (SF) is a process in which a singlet excitation splits into two uncoupled triplet excitations. SF represents one strategy to overcome the Shockley-Queisser efficiency limit of solar cells, with photovoltaic devices utilising singlet fission having achieved quantum yields of over 100%. The singlet fission process is thought to involve triplet-pair singlet intermediates: one such intermediate is the $^1(TT)$ state which forms after the initial photoexcitation, and another example is the $^1(T\cdots T)$ state which is produced when the constituent triplets of the $^1(TT)$ state lose electronic interaction and only spin coherences persist.

One of the major classes of SF materials is conjugated linear polymers. In these systems, the first optically active excitation is to the $1^1B_u^+$ singlet state. However, this state is not the lowest energy singlet state. The $2^1A_g^-$, $3^1A_g^-$, $1^1B_u^-$ states can fall below the optical $1^1B_u^+$ state depending on electronic screening and conjugation length. These states have triplet-pair character and this thesis explores which of the eigenstates contribute to the $^1(TT)$ and $^1(T\cdots T)$ states.

Firstly, using density matrix renormalisation group (DMRG) calculations of the Pariser-Parr-Pople-Peierls Hamiltonian, the Hellmann-Feynman relaxed geometries of the eigenstates are found. The $2^1A_g^-$, $1^1B_u^-$ and $3^1A_g^-$ states' triplet-triplet characters are confirmed by calculations of bond dimerization, spin-spin correlation and wavefunction overlap with products of triplet states.

It is found that there is a family of singlet excitations (i.e., $2^1A_g^-$, $1^1B_u^-$, $3^1A_g^-$, $\cdots$), composed of both triplet-pair and electron-hole character, which are fundamentally the same excitation, but have different centre-of-mass energies. The lowest energy member of this family, the $2^1A_g^-$ state, cannot undergo singlet fission. However, higher energy members (e.g., the $3^1A_g^-$) state, owing to their increased kinetic energy and reduced electron-lattice relaxation, can undergo singlet fission for specific chain lengths, with the $1^1B_u^-$ and $3^1A_g^-$ states being candidates for the $^1(TT)$ state.

Following on from these calculations, the first step of singlet fission, where the photoexcited state evolves into the $^1(TT)$ correlated triplet pair state, is probed. This step is referred to as state interconversion. Both Ehrenfest dynamics and dynamics with quantised phonons were performed for the UV-Peierls model using time-dependent density matrix renormalisation group (t-DMRG). State interconversion was found to be ultrafast, occurring in 10s fs. Additionally, it was found that the electronic environment determines to which triplet-pair eigenstate the photoexcited state evolves. Changing the Coulombic parameter, U, causes state interconversion shift from $1^1B_u^+ \rightarrow 2^1A_g^-$ to $1^1B_u^+ \rightarrow 3^1A_g^-$. These are the first dynamics results that show the formation of the $3^1A_g^-$ state and they have important consequences for explaining intramolecular singlet fission observed in carotenoids.

This thesis is dedicated to my mum, Mary Valentine (1964-2017).

All that is good in me can be attributed to her.

Acknowledgements

I wish to thank first and foremost my supervisor, William Barford. Through your support and guidance, I found the PhD process to be a rewarding experience. You showed me particular patience during some tough times, and I know I am lucky to have such an understanding supervisor. I also wish to extend my thanks to our collaborator Jenny Clark and her group for highly productive scientific discussions. Furthermore, I would like to acknowledge the support I received from Balliol College, particularly the generous Foley-Béjar fund.

During my time in Oxford, I had the great pleasure of working with many friends in the Theory Annexe, including Laszlo, Izzy, Dilhan, Jonathan, Tom, Tim, Joe, Lachlan, Matt, David and Dom. However, it was an even greater pleasure to spend hours in your company at the Uni club. A particular shoutout is directed towards Max Marcus, who even in his time away from Oxford encouraged spending in pubs at a level Rishi Sunak dreams of. I want to take this opportunity to thank the members of the Barford group especially.

Thank you to all the friends I made in Oxford beyond Chemistry, in particular, the people who made me 'Honorary SABS'. I also want to thank friends from Cambridge and home, who brought the craic throughout the years. I'm grateful to have you in my life.

To Rachel and Andrew, I cannot thank you enough for taking me into your home during the pandemic. Staying with you gave me the time and space to focus on this thesis, but I also enjoyed the cake.

Thank you to my family Rosaleen, Gerard and Cormac, without your support over the last few years, it has been invaluable.

To my parents, you always encouraged me to pursue my goals, no matter how far it takes me away from Irvinestown. This love and support have helped make me who am I am today.

To Isabel, people often claim that their PhD is their greatest achievement (at least at the point of writing). For me, however, it is a secondary achievement to the loving relationship I have built with you. At times you've been my inspiration and my rock, but most of all you are the person who laughs at all my jokes. Thank you.

Abbreviations

BO	Born-Oppenheimer
CNDO	Complete Neglect of Differential Overlap
CT	Charge Transfer
DMRG	Density Matrix Renormalization Group
DPDC	Diphenyldicyano oligoenes
MPS	Matrix Product State
NRG	Numerical Renormalisation Group
PCE	Power Conversion Efficiency
PES	Potential Energy Surface
PPP	Parsier-Pople-Parr model
PPPP	Parsier-Pople-Parr-Peierls model
PV	Photovoltaic
SF	Singlet Fission
SVD	Singular Value Decomposition
TDSE	Time Dependent Schrödinger equation
TIPS	Tri-isopropylsilylethynyl
UV	UV-model refers to the extended Hubbard model
ZDO	Zero Differential Overlap

Publications

The work presented in this thesis forms the basis of the following publications:

- **Chapter 4:** D. J. Valentine, D. Manawadu, and W. Barford; Higher-energy triplet-pair states in polyenes and their role in intramolecular singlet fission, *Phys. Rev. B*, **102(12)**, 125107 (2020)
- **Chapters 5 and 6:** D. J. Valentine, D. Manawadu, and W. Barford; Bright-state to triplet-pair interconversion in polyenes: A t-DMRG and Ehrenfest study of the UV-Peierls model (In preparation) (2020)

Contents

Declaration of Authorship i
Abstract iii
Acknowledgements vii
Abbreviations ix

1 Introduction **1**
1.1 Motivation 1
1.2 Singlet fission 3
1.2.1 Fundamentals 5
1.2.2 Four electron view of singlet fission 8
1.2.3 Mechanism of singlet fission 11
1.3 Singlet fission materials 13
1.3.1 Acene systems 14
1.3.2 Polyene systems 15
1.4 Aims of this thesis 18

2 Theoretical Background **21**
2.1 Description of π-conjugated polyenes 21
2.1.1 Born-Oppenheimer approximation 22
2.1.2 Treatment of σ and π electrons 24
2.1.3 Electron-nuclear coupling 27
2.1.4 Nuclear-nuclear interactions 28
2.1.5 Symmetries 29
2.2 Electronic states in polyenes 32
2.2.1 Peierls distortion 32
2.2.2 Broken symmetry 34
2.2.3 Solitons 35
2.2.4 Spinons 37

3 Computational Methods **41**
3.1 Density matrix renormalisation group 41
3.1.1 Infinite and finite algorithms 47

3.2 Density matrix truncation and the rotation to the new basis 50
3.2.1 Wave function prediction 52
3.2.2 Excitations 53
3.2.3 Symmetries 54
3.2.4 Why DMRG works: Entanglement, entropy and area law . . . 55
3.2.5 DMRG and MPS 58
3.3 Time-dependent density matrix renormalisation group 59
3.3.1 Suzuki-Trotter decomposition 60
3.3.2 t-DMRG algorithm 62

4 Polyene triplet-pair states and their role in singlet fission 65
4.1 Introduction 65
4.2 Methods 67
4.2.1 Pariser-Parr-Pople-Peierls model 67
4.3 Results 70
4.3.1 Vertical and relaxed energies 70
4.3.2 Soliton structures 73
4.3.3 Spin-spin correlation 80
4.3.4 Excited state wavefunctions 82
4.3.5 Exciton wavefunctions 86
4.3.6 The '$2A_g$ family' 89
4.3.7 Spectra 89
4.4 Discussion and conclusions 93

5 State interconversion: Ehrenfest dynamics 97
5.1 Introduction 97
5.1.1 Singlet fission in carotenoids 97
5.2 Methods 101
5.2.1 UV-Peierls model and Ehrenfest dynamics 101
5.2.2 Symmetry breaking 105
5.3 Results 106
5.3.1 Potential energy surfaces 106
5.3.2 Identification of states 110
5.3.3 Dynamics of the $1^1B_u^+$ state 114
5.4 Conclusions 124

Appendices 127
5.A Velocity Verlet 127
5.B Spin-spin correlation 130
5.C Dynamics of bond dimerisation of low energy states 132

5.D Convergence of t-DMRG parameters 134

6 State interconversion: Quantised nuclear degrees of freedom 137

6.1 Quantisation of the nuclear degrees of freedom 138

6.1.1 Initial state 141

6.2 Results 143

6.2.1 Dynamics of photoexcited state 143

6.3 Summary 149

Appendices 151

6.A Parameter selection for the quantum UV-Peierls model 151

7 Conclusions and future work 153

Bibliography 159

Chapter 1

Introduction

1.1 Motivation

Climate change is one of the most pressing existential risks to society. The IPCC predicts that if warming exceeds 1.5°C above preindustrial levels, the resulting changes to our planet will be detrimental to life as we know it.[1] It is broadly accepted that we must rapidly reduce our carbon emissions, and one of the most effective ways this can be achieved is through the use of renewable energy sources such as wind, solar and hydroelectric power.[2]

Solar cells

Renewable energy technologies, in particular solar cells, have seen a rapid decrease in cost over the past 20 years.[3,4] Whilst further cost reductions are expected, commercially available solar cells currently suffer from low efficiency.

Conventional silicon solar cells contain a mixture of n-type silicon (doped with pentavalent atoms which contribute electrons to the material) and p-type silicon (doped with trivalent atoms which result in electron vacancies, called holes). Migration of electrons and holes between the p- and n-type silicon creates a depletion zone near the p-n interface. A field is created across the junction where the oppositely charged regions meet. When a photon is absorbed, an electron is promoted from

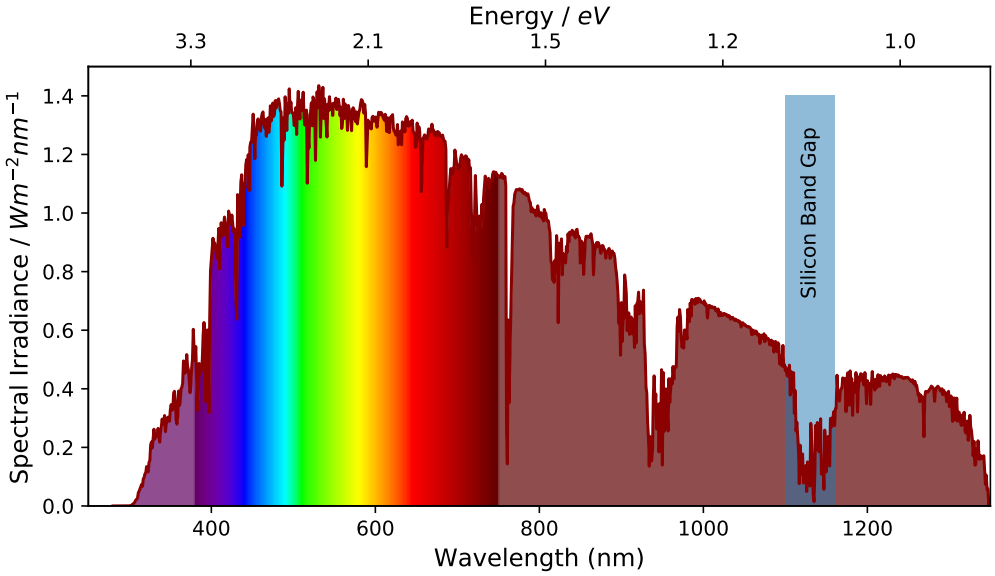


Figure 1.1: The solar spectrum at the surface of the earth with the band gap of silicon highlighted.

the valence band to the conduction band, generating an electron-hole pair which is separated by the presence of the field. Placing a load across the junction leads to the generation of electricity.

Since photons must have energy greater than silicon's band gap ($\approx$ 1.1 eV) to generate the electron-hole pair, photons with insufficient energy are either not absorbed or generate non-electronic excitations. Meanwhile, photons with energy greater than silicon's band gap (the majority of solar radiation, Fig. 1.1) generate electricity but their excess energy is lost as heat and vibrations in the solar cell (known as thermalisation loss). Thus, there is a fundamental limit in efficiency for a single absorber photovoltaic (PV) cell, known as the Shockley–Queisser limit or the detailed balance limit.[5]

This limit puts the theoretical maximum power conversion efficiency (PCE) (the total efficiency with which solar spectrum is converted to electricity) of a silicon solar cell at 29%.[4] The best silicon-based solar cells can currently achieve a PCE of 26.5% in a laboratory setting.[3] This limit has spurred a range of research into strategies to better utilise the solar spectrum.

1.2 Singlet fission

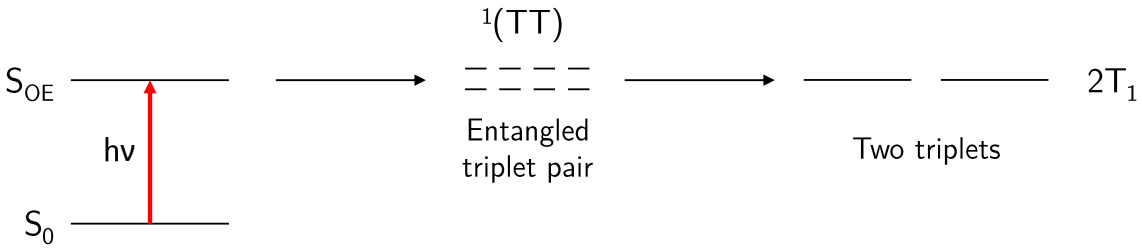


Figure 1.2: A Jablonski diagram of singlet fission. Absorption of a photon by a chromophore leads to the formation a singlet exciton, S_{OE}. S_{OE} then evolves into the entangled/correlated triplet-pair state, $^1(TT)$. Finally, the triplets making up $^1(TT)$ decohere forming two independent triplets. The relative energies of the states are not to scale.

One such strategy is the use of a material that undergoes singlet fission (SF). Singlet fission is a process in which a singlet excitation evolves into two separate independent triplet states, as seen in Fig. 1.2. Coupling of an SF material with an inorganic semiconductor is proposed to increase solar cell efficiency[6,7] by extending the spectrum of light above the band gap which can be used to generate electricity. Optimal choices of the SF and semiconductor materials allow for absorption of high energy photons which are converted to independent triplets with energy greater than the semiconductor band gap, enabling electron-hole pair production in the semiconductor (Fig. 1.3). Therefore, absorption of one higher energy photon can generate two free carriers, increasing the efficiency of the solar cell and decreasing thermalisation losses. The theoretical PCE of a singlet fission solar cell is 45%.[8]

Fast singlet fission is required to out-compete the inefficient transfer of the photoexcited SF singlet excitation to the inorganic material before the generation of the triplets.[9] The external quantum efficiency (EQE) is the fraction of incident photons that are converted into electrons and delivered to the load; in a singlet fission device EQE can be greater than 100%. Currently, the top performing singlet fission solar cells for EQE use pentacene as the SF material and an organic charger-carrier generator, achieving an external quantum efficiency of 126%[10] and an internal quantum

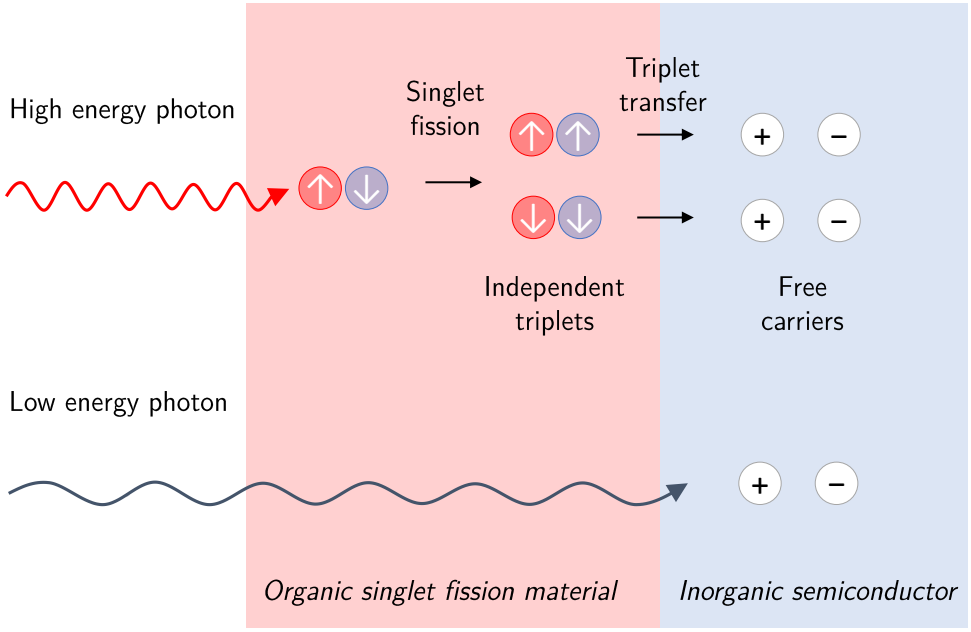


Figure 1.3: Schematic for a singlet fission photovoltaic device. An SF material (with a photo excitation energy of $\approx 2E_g$) is coupled with a semiconductor material (with band gap E_g). Incoming low energy photons ($2E_g > h\nu > E_g$) are absorbed in the semiconductor generating electron hole pairs. High energy photons ($h\nu > 2E_g$) are absorbed by the SF material and the initial photoexcited state evolves into two triplets, $2T_1$. These two triplet excitations can each generate electron hole pairs in the semiconductor. Thus, a single photon of energy $> 2E_g$ generates two electron hole pairs. This increases efficiency (PCE) compared to a single-junction semiconductor PV device.

efficiency (the fraction of absorbed photons that are converted into mobile carriers) of almost 200%.[11] The singlet fission process is not limited to silicon or organic charge-carrier generators but can be coupled with inorganic[8] or perovskite[12] technologies as well.

There is much interest in singlet fission even beyond photovoltaic research. SF has been observed in photosynthetic bacteria, where it may act as a competing pathway to photosynthesis or act as a mechanism to photo-protect the light harvesting complexes.[13–16] Furthermore, since singlet fission is a prototypical ultra-fast process, it is difficult to study with conventional spectroscopies, motivating photophysicists and spectroscopists to design new experimental methodologies such as ultra-fast vibronic spectroscopy[17] or coherent spin manipulation.[18] Finally, the multi-excitonic state involved in singlet fission requires a fundamental understanding of quantum mechanics and electronic structure and dynamics and is therefore of great interest

to theoretical chemists.[9]

1.2.1 Fundamentals

The process of singlet fission whereby an excited singlet state evolves into two independent triplets is often represented by,

$$S_{OE} \rightleftharpoons {}^1(TT) \rightleftharpoons T + T. \tag{1.1}$$

Here, S_{OE} is an optical excited (or bright) state for an absorbing chromophore, which may or may not be lowest energy singlet excitation, depending on the system (discussed in Sec. 1.3). In many organic systems, the lowest energy triplet state, T, lies well below S_{OE}. During the first step of singlet fission, a bound triplet-pair singlet state is formed. This ${}^1(TT)$ state is a multi-exciton state which is difficult to probe experimentally but understanding its role in SF is important for the design of efficient materials. The role of triplet-pair states in singlet fission has been extensively reviewed in recent years elsewhere.[19–22]

As shown in Eq. (1.1), spin angular momentum is conserved during the formation of ${}^1(TT)$. As a result, singlet fission can be viewed as a type of internal conversion and can occur on ultra-fast timescales, $\approx$ 200 fs. In organic SF materials, triplet generation can also occur via intersystem crossing although this is achieved on much longer timescales with smaller triplet yields.[23]

Singlet fission was initially observed in acene materials in the 1960s[24,25] and proposed to be the reverse of triplet-triplet annihilation.[26] A common view of Eq. (1.1) is that S_{OE} is an excitation localised on a single molecule, which then interacts with a nearby molecule in its ground state S_0, leading to the formation of the ${}^1(TT)$ state, which is delocalized over the two molecules.[7,27] This view, however,

is incomplete. Firstly, singlet fission can be an intramolecular process,[28–30] and additionally, the initial photoexcited singlet, S_{OE}, and the $^1(TT)$ state may be delocalized over more than two molecules. This is particularly the case for molecular solids, where singlet fission may take place over many molecular units.[31]

In addition to this shift in viewpoint, many members of the singlet fission community have begun to adopt a more dynamic view of the $^1(TT)$ state.[20] This has led to an understanding of singlet fission as first proposed by Scholes,[32] given by:

$$S_{OE} \overset{1}{\rightleftharpoons} {}^1(TT) \overset{2}{\rightleftharpoons} {}^1(T\cdots T) \overset{3}{\rightarrow} T + T, \tag{1.2}$$

Here, the first step of single fission remains the evolution from an initial photoexcited singlet state to a triplet-pair state. The $^1(TT)$ state is described as having both electronic and spin coherence between the triplets. Loss of the electronic interaction, in step 2, produces $^1(T\cdots T)$. This loss can be facilitated by the physical separation of the triplets, interactions with the environment or with local magnetic fields.[33]

Both of the $^1(TT)$ and $^1(T\cdots T)$ states are multi-excitonic states. Some authors now adopt the convention of referring to the formation of the $^1(T\cdots T)$ state as singlet fission rather than the formation of two independent triplets.[20] This is because spin coherence between the triplets is anticipated to have minimal effect on the photophysical and chemical properties of the individual triplets.[34,35] The model proposed by Scholes is corroborated by an experiment that detected features of two different triplet-pair intermediates, i.e. $^1(TT)$ and $^1(T\cdots T)$ in pentacene derivatives.[36]

Conditions for efficient singlet fission

For a singlet fission material to improve the efficiency of a solar cell, a number of conditions, first discussed by Michl and co-workers, need to be met.[7,27]

Thermodynamic condition It has been generally considered that for efficient singlet fission, the energy of the starting photoexcited singlet state, S_{OE} must be at least twice the energy of the lowest energy triplet excitation, T_1.[7,27] However, this criterion is not strict, with endothermic singlet fission being observed most notably in tetracene systems,[37] and reportedly even when endothermicity is about 300 meV.[38] When evaluating this thermodynamic condition, excited states should be considered in their relaxed geometries, as internal vibrational relaxation is faster than the singlet fission process.[9]

Kinetic condition In addition, the exothermic difference for the thermodynamic condition should not be so large that it inhibits the kinetic formation of the triplet-pair state. Therefore ideally, $E(S_{OE}) \approx 2E(T_1)$.

Efficient avoidance of relaxation pathways For efficient SF, major relaxation pathways including triplet-triplet fusion, non-radiative decay and intersystem crossing must be out-competed. During triplet-triplet fusion, independent triplets can not only rebind to form $^1(TT)$ (reversing SF) but also form quintet, Q, or higher energy triplet states, T_n (discussed further in section 1.2.2). Triplet-triplet fusion can be minimised where $E(Q) \geq 2E(T_1)$ and $E(Q) \geq 2E(T_n)$, however this can be difficult to predict. Meanwhile, non-radiative decay to the ground state is exacerbated in some organic molecules which have many dark states lower in energy than the bright state, facilitating relaxation. In particular, flexible systems such as polyenes suffer from relaxation to the ground state to a greater extent than rigid acene molecules.[9]

1.2.2 Four electron view of singlet fission

The simplest model that can be used to represent the photoexcited state in an organic system is the two electron model. There is one excited singlet state and three excited triplet states, as follows:

$$\begin{aligned}
\left|S_1^{(2)}\right\rangle &= \frac{1}{\sqrt{2}}\left(|\alpha_1\beta_2\rangle - |\beta_1\alpha_2\rangle\right), \\
\left|T_{-1}^{(2)}\right\rangle &= |-\rangle = |\beta_1\beta_2\rangle, \\
\left|T_0^{(2)}\right\rangle &= |0\rangle = \frac{1}{\sqrt{2}}\left(|\alpha_1\beta_2\rangle + |\beta_1\alpha_2\rangle\right), \\
\left|T_{+1}^{(2)}\right\rangle &= |+\rangle = |\alpha_1\alpha_2\rangle .
\end{aligned} \tag{1.3}$$

Here, the $|\alpha_1\rangle$ ($|\alpha_2\rangle$) refers to an up spin in the dimer system HOMO (LUMO) while the label β refers to a down spin. The constituent spin components of the states are represented in Fig. 1.4. The two electron states presented here are the *high-field basis*, since they are the eigenvalue states in the case of an applied external magnetic field B_z. The high field basis uses the notation $|0\rangle, |+\rangle$ and $|-\rangle$ and the spin components of the triplet states are symmetric with respect to exchange. This necessitates that the spatial component is anti-symmetric as per the Pauli exclusion principle. Overall, this leads to triplet excitation being lower in energy than singlet excitations.

Whilst a two electron model is sufficient to describe the initial photoexcited state, a four electron model is needed at a minimum to describe the $^1(TT)$ and $(T\cdots T)$ triplet-pair states. Four electron models have been introduced by Scholes, Kollmar and others to describe triplet-pair states.[9,19–21,32,39] In a four electron model, there are 16 different spin arrangements. By using this 16 spin component basis, we find the 5 distinct eigenstates of the $\hat{S}^2$ operator. These are 2 singlet states, 3 triplet states and one quintet state.

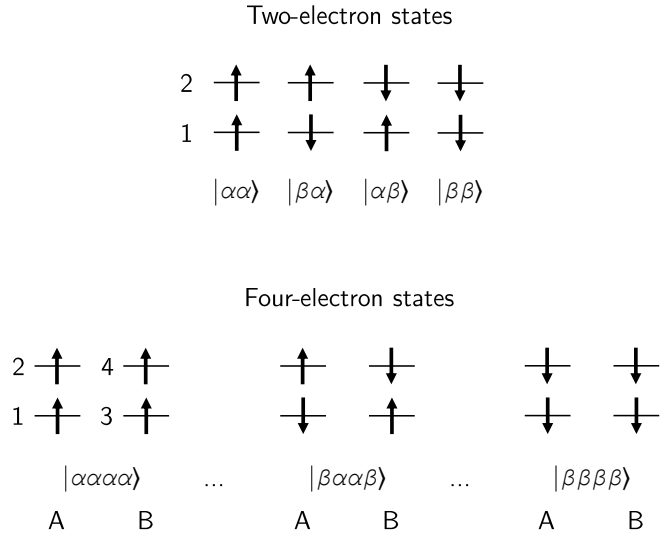


Figure 1.4: The two-electron and four-electron product basis states. $|\alpha\rangle$ and $|\beta\rangle$ represent the spin up and spin down eigenstates to the single electron operator S_1^z.

The states corresponding to the $M_S = 0$ sector are as follows:

$$
\begin{aligned}
\text{Singlet 1}: \ |S_1\rangle &= \frac{1}{\sqrt{12}}\left(2\,|\alpha\alpha\beta\beta\rangle + 2\,|\beta\beta\alpha\alpha\rangle - |\alpha\beta\alpha\beta\rangle - |\beta\alpha\alpha\beta\rangle - |\alpha\beta\beta\alpha\rangle - |\beta\alpha\beta\alpha\rangle\right), \\
\text{Singlet 2}: \ |S_2\rangle &= \frac{1}{2}\left(|\alpha\beta\alpha\beta\rangle - |\beta\alpha\alpha\beta\rangle - |\alpha\beta\beta\alpha\rangle + |\beta\alpha\beta\alpha\rangle\right), \\
\text{Triplet 1}: \ |T_1\rangle &= \frac{1}{\sqrt{2}}\left(-\,|\alpha\alpha\beta\beta\rangle + |\beta\beta\alpha\alpha\rangle\right), \\
\text{Triplet 2}: \ |T_2\rangle &= \frac{1}{\sqrt{2}}\left(-\,|\alpha\beta\alpha\beta\rangle + |\beta\alpha\beta\alpha\rangle\right), \\
\text{Triplet 3}: \ |T_3\rangle &= \frac{1}{\sqrt{2}}\left(-\,|\alpha\beta\beta\alpha\rangle + |\beta\alpha\alpha\beta\rangle\right), \\
\text{Quintet}: \ |Q\rangle &= \frac{1}{\sqrt{6}}\,|\alpha\alpha\beta\beta\rangle + |\beta\beta\alpha\alpha\rangle + |\alpha\beta\alpha\beta\rangle + |\beta\alpha\alpha\beta\rangle + |\alpha\beta\beta\alpha\rangle + |\beta\alpha\beta\alpha\rangle\,,
\end{aligned}
\tag{1.4}
$$

where we have dropped the molecular orbital label for the one electron states and MOs 1 (2) and 3 (4) are the HOMOs (LUMOS) for dimers A and B, respectively. The first singlet state is a triplet-pair state. By considering the high field basis, S_1 can be written as $|S_1\rangle = \frac{1}{\sqrt{3}}\left(|00\rangle - |{+}{-}\rangle - |{-}{+}\rangle\right)$. S_1 is a correlated triplet-pair state and in four electron models is considered equivalent to the ${}^1(TT)$ state.

The quintet state can similarly be written as a correlated triplet-pair state, $|Q\rangle = \frac{1}{\sqrt{6}}(|+-\rangle + |-+\rangle + 2|00\rangle)$. The second singlet state S_2 can be considered as being formed of a pair of singlet states, $^1(SS)$.[19]

The exact energy ordering of these states is interaction dependent and in spin-only systems, inter- and intra-triplet dipole couplings need to be considered. In more realistic models, these spin states will mix with charge transfer (CT) or ionic states, leading to large changes in energy. These states will also couple to the nuclear lattice and lower their energies via geometry relaxation.[19] Even in a four soliton electron model, predicting the kinetic pathway between different states becomes very difficult.

As mentioned, the triplet-pair states can stabilise through mixing with ionic and charge transfer states. The singlet triplet-pair state is more readily stabilised due to its energetic proximity to ionic states of singlet character. The quintet state, however, retains much more of its radical spin character as ionic quintet states are much higher in energy. This leads to the approximation that $E(Q) \approx 2E(T_1)$.[9,19] This is particularly useful when investigating a system in which the relaxed triplet energy is difficult to observe.

The transient and multi-excitonic nature of the $^1(TT)$ means it is extremely difficult to characterise experimentally. Indeed, this state has only been directly observed a handful of times.[40–42]

The singlet triplet-pair state may not be the only intermediate. In addition, the quintet $^5(TT)$ state has also been proposed as a singlet fission intermediate.[43] The mixing of spin components of the $^1(TT)$ with the $^5(TT)(S_z = 0)$ state can be allowed via spin dipole-dipole interactions. Indeed, this mixing of states was proposed by Merrifield,[44] while the quintet triplet-pair state has been observed in tetracene films, via ESR experiments.[18] Moreover, the quintet state has also been detected during

singlet fission in pentacene dimers[43,45] via transient EPR experiments. Many of the experiments in the literature are not able to distinguish between the different triplet-pair states. This and the fact that singlet-quintet mixing is viable have led some authors to refer to the SF intermediate multi-exciton state as ${}^{m}(TT)$, as its precise spin nature is difficult to ascertain.[22]

1.2.3 Mechanism of singlet fission

Difficulties in observing singlet fission dynamics has fuelled debate regarding the mechanism of the intermediate triplet-pair state.[9,20] As singlet fission is a ultra-fast process, it can be difficult to track its evolution accurately and as there are multiple states involved, interpreting spectroscopic data can be challenging. In addition, assumptions made to keep theoretical mechanism studies tractable often do not generalise very well. These challenges have complicated elucidation of the mechanism of singlet fission.

One of the most prevalently proposed mechanisms is the direct mechanism, in which the rate of ${}^{1}(TT)$ formation is entirely determined by the coupling between the initial singlet and the multi-exciton state.[7,27] This mechanism involves the simultaneous transfer of two electrons as depicted in Fig. 1.5.

The majority of theoretical work on modelling the SF mechanism has focused on acene systems. In an early study, Zimmerman et. al. used a model Hamiltonian to investigate the direct mechanism, finding the direct coupling between the singlet and ${}^{1}(TT)$ to be quite low, ≈ 5 meV, in pentacene and tetracene dimers.[46] Despite this small coupling, it was sufficient to replicate some experimental observations of singlet fission. However, subsequent experimental and theoretical studies support an alternative mediated mechanism.[3]

The mediated mechanism (also called the two-step mechanism) involves the use

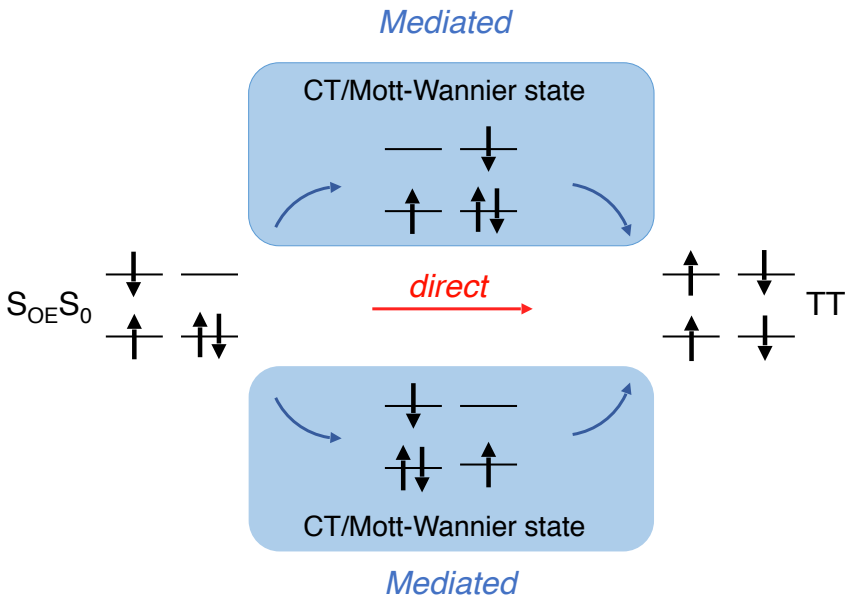


Figure 1.5: The models for triplet-pair state formation. The direct mechanism (red) is solely controlled by coupling between the $S_{OE}S_O$ and TT states. The mediated mechanism (blue) involves the coupling to nearby charge transfer (CT) or Mott Wannier states.

of intermediate charge transfer states. The charge transfer states are more commonly known as Mott-Wannier states in extended polyene systems, due to their propensity for intramolecular charge transfer rather than intermolecular.

During the mediated mechanism, an electron first transfers from the excited singlet to a neighbouring molecule, forming the charge transfer state. Next, a second electron transfer forms the $^1(TT)$ state. This process is determined by two couplings, the coupling of the initial singlet to the charge transfer state and from the charge transfer state to the $^1(TT)$ state. This mediation, in most cases, is virtual with some studies finding that singlet fission can proceed via a virtually mediated mechanism even in the case when the CT transfer state is 1 eV higher in energy than the singlet and triplet-pair state.[47,48] The coupling between states being mediated by virtual intermediates is termed super exchange.[48]

Experimentally distinguishing between the direct mechanism and the virtual mediated mechanism remains difficult as in both cases there are no observable intermediates. In addition, as mentioned above, both the initial photoexcited state and

the triplet-pair states themselves may have some charge transfer character. However, at present, the consensus is that the mediated mechanism dominates in singlet fission.[3]

Vibronic coupling

All previously discussed models assume static nuclei and static coupling between states, which can be convenient and give qualitative insight into quantum systems. However, electronic states in most organic molecules exhibit strong electronic phonon coupling, affecting the dynamics of the system, which must therefore be included in any accurate and realistic model. The effect of molecular vibrations on electronic coupling can be treated both quantum mechanically and classically. Beyond singlet fission, vibronic coupling is thought to play a role in a number of ultrafast processes in organic molecules including photosynthesis.[49] Using ultrafast 2D electronic measurements, Stern and co-workers observed vibronic coupling between the S_{OE} and $^1(TT)$ in a pentacene system.[37] Work by Musser and co-workers using ultrafast vibronic spectroscopy on pentacene dimers showed that strong vibronic couplings induce the conversion of S_{OE} to $^1(TT)$ and that this process resembles the internal conversion observed in polyenes.[50]

1.3 Singlet fission materials

Initial studies of singlet fission were limited to more tractable acene materials, however in recent decades singlet fission research has broadened to a number of different organic molecules. Systems found to undergo singlet fission include polyacenes, polyacene dimers, polyacetylene, carotenoids and charge-transfer polymers. Whether singlet fission has a universal mechanism amongst these materials is an open question,[19] as there are differences in their excited state landscapes. In this

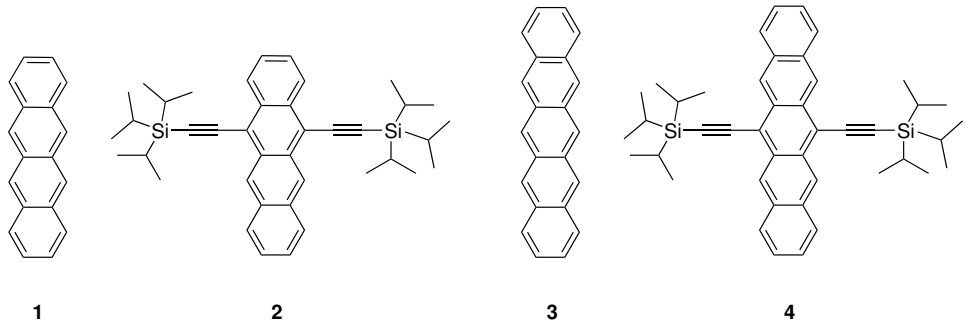


Figure 1.6: Acene systems that undergo singlet fission. Tetracene, **1**; TIPS(triisopropylsilylethynyl)-tetracene, **2**; pentacene, **3** and TIPS-pentacene, **4**.

section, the two broad classes of molecules that undergo singlet fission, the acenes and the polyenes/conjugated polymer systems, will be reviewed.[27]

1.3.1 Acene systems

Tetracene **1**, pentacene **3** and their TIPS (triisopropylsilylethynyl) variants (**2**, **4**; Fig. 1.6) represent the most widely studied singlet fission materials. In these materials, the first optical excited singlet state is also the lowest energy singlet state, i.e. $S_1 = S_{OE}$ for a single molecule. Studies of pentacene have found that this singlet state lies above the multi-chromophore $^1(TT)$ state, making SF exothermic. Pentacene has been shown to undergo very rapid singlet fission, on the order 80 fs.[51,52]

Tetracene also undergoes singlet fission, but here, it is thought to be endothermic with an activation barrier of 200 meV. Wilson and co workers studied SF in tetracene via transient absorption spectrometry for temperatures 10-270 K.[53] They found the rate of formation of the triplet-pair to be temperature independent. However, lower temperatures impeded the formation of independent triplet and increased the rate of triplet-triplet recombination.

Overall, studies have concluded that SF proceeds via the mediated mechanism for acene materials. Lukman and co-workers investigated a range of TIPS-pentacene derivatives,[53] showing that changes in the energy of the charge transfer states shifted

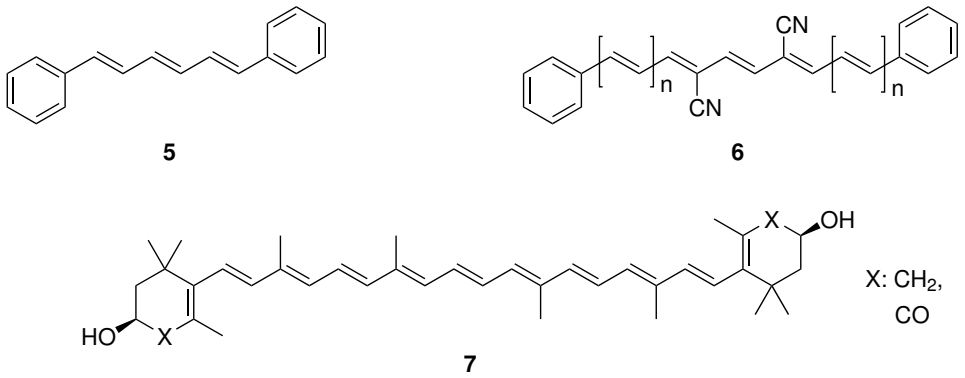
the mechanism between virtual mediated and real mediated. In the latter case, they observed a charge transfer state intermediate forming during singlet fission. In the systems in which a CT intermediate did not form, SF fission was shown to depend on the solvent polarity, indicating that a virtual mediated mechanism was the mechanism of SF for these molecules.

In the acene materials, singlet fission is assumed to be an intermolecular process, however recently there has been a great deal of interest in covalently linked acene dimers.[38,45,54] Systems such as tetracene and pentacene form molecular crystals that contain defects. These defects can have a large effect on SF and decay pathways,[55] but by using covalently linked dimers these decay pathways can be avoided. Indeed, the mode of covalent linkage can determine whether singlet fission can proceed in these systems, with recent theoretical studies providing insight into structure property relationships[56] with Khan and co-workers finding that the triplet-pair state does not dissociate into triplets in para-linked pentacene dimers.

Whilst the triplet-pair state readily forms in dilute dimer solutions, independent triplet formation can be hindered by extensive triplet-triplet fusion, as triplets cannot diffuse from one another. However, examples of free triplets in solution have been reported, such as in pentacene dimers.[43]

1.3.2 Polyene systems

Although singlet fission in polyene systems was first reported in carotenoids in photosynthetic bacteria in the 1980s,[57] interest in the phenomenon emerged only in the 2000s. Unlike acene systems, the optical excited singlet state in polyenes is not the lowest energy singlet state. The bright state has ${}^1B_u^+$ symmetry (symmetry labels of polyene systems is discussed in section 2.1.5). Often the $1{}^1B_u^+$ state is labelled the S_2 state, but this energy ordering is system and conjugation length dependent.[58] Below



5 6 7

Figure 1.7: Polyene systems that undergo singlet fission. 1,6-diphenylhexatriene, **5**; diphenyldicyano oligoenes (DPDC), **6**; carotenoids **7**, X=CH_2: zeaxanthin, X=CO: astaxanthin

the $^1B_u^+$ state there is the $2^1A_g^-$ state, which has significant triplet-pair character but its role in singlet fission remains unclear.[59,60] In addition, there are a number of other dark states which may contribute to singlet fission intermediates.[61] This complicated electronic landscape is one reason the polyene and conjugate polymer systems have been studied less than the acenes, and that their mechanism of SF is still unknown.

Carotenoids and other short polyenes

In short polyene systems (e.g. **5** and **6**, Fig. 1.7), it is assumed that singlet fission is intermolecular.[27] However, a recent study on diphenyldicyano oligoenes (DPDC) **6** found that an intramolecular triplet-pair state initially forms, followed by an intermolecular process leading to two free triplets.[62] In this system, the electron-withdrawing cyano groups are thought to enhance the CT character of the involved states.

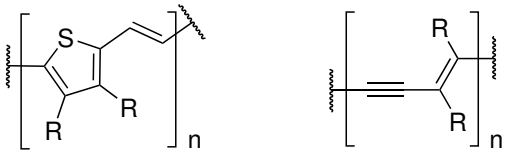
In longer polyenes such as carotenoids **7**, singlet fission has only been observed in aggregates[30,63] and in the photosynthetic reaction centre of cyanobacteria.[13–16,64–67] Wang and co-workers investigated singlet fission in zeaxanthin aggregates using time-resolved resonance Raman spectroscopy. Despite the strong triplet-pair character of the lower lying $2^1A_g^-$ state, they concluded that it was not involved in SF.[63] In a

further study, they embedded zeaxanthin molecules in a lipid bilayer membrane at various separation distances and surmised the SF process to be intermolecular.[68]

Musser and co-workers also conducted work into carotenoid aggregates, studying astaxanthin systems.[59] Using transient absorption measurements, they found signatures of intermolecular singlet fission. In dilute solution, when the carotenoid is assumed to be monomeric, they observed only internal conversion from the $1^1B_u^+$ to the $2^1A_g^-$ singlet state. In aggregates, they found singlet fission to proceed directly from the $1^1B_u^+$ with no signature of the $2^1A_g^-$ or other triplet-pair intermediate states. The nature of carotenoid singlet fission is further discussed in Chapter 5.

Extended conjugated polyenes

Extended conjugated polymer systems (N > 50) allow the possibility of two excitations to exist within one chain and therefore allow for intramolecular singlet fission. Conjugated polymers show much stronger coupling between chromophoric units than aggregates,[58] and could therefore provide a pathway to efficient singlet fission. Much like the covalent dimers, intramolecular singlet fission in polymers may allow the development of structural relationships that can be fine-tuned for singlet fission.[9,38,69]



8 **9**

Figure 1.8: Conjugated polymers that undergo singlet fission.
Poly(thienylenevinylene), **8**; polydiacetylene (R=H) and derivatives, **9**.

Singlet fission in extended π-conjugate systems is often found to require photoexcitation to a hot (vibrationally excited) bright state to proceed in an intramolecular fashion. This has been found in poly(thienylenevinylene) **8**[30,70] and polydiacetylene

9[71] (Fig. 1.8) and is further discussed in Chapter 4.

Since charge transfer states are found to mediate singlet fission in the acene materials, there has been interest in push-pull or donor acceptor polymers made up of alternating electron donating and electron withdrawing groups with the hope of imbuing charge transfer character to the low-lying states.[72] Busby and co-workers created push-pull co-polymers and by differing the strength of intrachain donor-acceptor interactions, they were able to increase the localization of triplets. However, as with other strongly coupled intramolecular systems, triplet-triplet fusion remained a problem.[72]

1.4 Aims of this thesis

This thesis aims to study the low energy triplet-pair states of polyenes and gain insight into which are most important in singlet fission. In particular, the state interconversion process, where the initial bright state evolves into a triplet-pair state, is probed.

In order to gain insight into singlet fission, a range of theoretical methods and models, introduced in Chapter 2, will be employed.

The computational workhorse of this thesis is the density matrix renormalisation group, which is introduced in the Chapter 3. The discussion is extended to the time-dependent density matrix renormalisation group, which is used extensively in later chapters to probe the dynamics of state interconversion.

In Chapter 4, characteristics of the $2^1A_g^-$, $3^1A_g^-$, $1^1B_u^-$ and $1^5A_g^-$ triplet-pair states are considered. Using a Hellmann-Feynman procedure, their relaxed energies and structures are found. The spin-density-wave and electron-hole character of these states are investigated using spin-spin correlations and exciton wavefunction projections, respectively, and candidate states for singlet fission are proposed based

on energetics.

In shorter polyenes, an open question is whether singlet fission is intramolecular and intermolecular. For instance, intramolecular singlet fission in carotenoids has only been detected in photosynthetic bacteria, and not in carotenoid aggregates. This suggests that the electronic environment could play a role in singlet fission, and in Chapter 5, this is investigated using an Ehrenfest framework. The state interconversion process, and to which triplet-pair state the photoexcited state evolves is probed.

While Ehrenfest dynamics can give qualitative insights, the theoretical assumptions of this method breakdown in the region near conical intersections, which are likely to play an essential role in singlet fission. To address these concerns state interconversion was again probed in Chapter 6, however, this time quantised phonons were used.

The thesis concludes with a summary of results, in Chapter 7, and future possibilities of research are then discussed.

Chapter 2

Theoretical Background

Having introduced singlet fission, and polyenes as candidate singlet fission materials, this chapter aims to provide a concise description of the theoretical models and methods used to probe the SF phenomena. The polyene systems that undergo SF contain a large number of nuclei and electrons. Large complex systems, such as these, require the many-body Hamiltonian (presented below) to be simplified or the use of approximate solutions. The following sections introduce the assumptions that lead to the π-conjugated electron models used throughout this thesis. Starting with the Born-Oppenheimer approximation, which explicitly decouples the electrons and nuclei, the discussion then turns to the separation of σ and π electronic degrees of freedom and how this leads to semi-empirical effective Hamiltonians. Finally, the reintroduction of electron-nuclear coupling into these models is discussed.

2.1 Description of π-conjugated polyenes

The many-body Hamiltonian describing a system of interacting electrons and nuclei can be written as

$$\hat{H} = \hat{H}_{n-n}(\mathbf{R}) + \hat{H}_{e-e}(\mathbf{r}) + \hat{H}_{e-n}(\mathbf{r}, \mathbf{R}), \tag{2.1}$$

where $\mathbf{R}$ is the set of nuclear coordinates and $\mathbf{r}$ is the set of electronic coordinates. The nuclear-nuclear term is given by

$$\hat{H}_{n-n}(\mathbf{R}) = \sum_{\alpha} \frac{\mathbf{P}_{\alpha}^2}{2M_{\alpha}} + \frac{1}{2} \sum_{\alpha \neq \beta} \frac{Z_{\alpha} Z_{\beta} e^2}{4\pi\epsilon_0 |\mathbf{R}_{\alpha} - \mathbf{R}_{\beta}|}, \tag{2.2}$$

which describes the nuclear kinetic energy and the Coulombic repulsive potential between nuclei. For the αth nucleus, $\mathbf{R}_{\alpha}$ is the coordinate vector, M_{α} is the mass and Z_{α} is the nuclear charge number. e is the elemental charge. The electron-electron interaction,

$$\hat{H}_{e-e}(\mathbf{r}) = \sum_{i} \frac{\mathbf{p}_i^2}{2m} + \frac{1}{2} \sum_{i \neq j} \frac{e^2}{4\pi\epsilon_0 |\mathbf{r}_i - \mathbf{r}_j|}, \tag{2.3}$$

describes the kinetic energy of the electrons and their electron-electron Coulombic energy. $\mathbf{r}_i$ is the coordinate of the ith electron while m is the mass of a single electron. Finally,

$$\hat{H}_{e-n}(\mathbf{r}, \mathbf{R}) = -\sum_{\alpha, i} \frac{Z_{\alpha} e^2}{4\pi\epsilon_0 |\mathbf{R}_{\alpha} - \mathbf{r}_i|}, \tag{2.4}$$

describes the Coulombic attraction between electrons and nuclei.

2.1.1 Born-Oppenheimer approximation

The Born-Oppenheimer (BO) approximation makes use of the fact that nuclear motion is much slower than electron dynamics. Under the BO approximation, the many-body wavefunction is factorised into a product of electronic and nuclear wavefunctions:

$$\Psi_{BO}(\mathbf{r}, \mathbf{R}) = \Psi_e(\mathbf{r}; \mathbf{R}) \Psi_n(\mathbf{R}), \tag{2.5}$$

where $\mathbf{R}$ is the instantaneous coordinates of the nuclei, Ψ_n is the nuclear wavefunction. Ψ_e is the electronic wavefunction which only depends parametrically on the

position of the nuclei and is an eigenfunction of the time independent electronic Schrödinger equation:

$$\hat{H}_{BO}(\mathbf{r};\mathbf{R})\Psi_e(\mathbf{r};\mathbf{R}) = E_e(\mathbf{R})\Psi_e(\mathbf{r};\mathbf{R}), \tag{2.6}$$

where,

$$\hat{H}_{BO}(\mathbf{r};\mathbf{R}) = \hat{H}_{e-e}(\mathbf{r}) + \hat{H}_{e-n}(\mathbf{r};\mathbf{R}) + \frac{1}{2}\sum_{\alpha,\beta\neq\alpha}\frac{Z_\alpha Z_\beta e^2}{|\mathbf{R}_\alpha - \mathbf{R}_\beta|}. \tag{2.7}$$

The Born Oppenheimer approximation is an adiabatic approximation: it assumes that for small changes in the nuclear geometry, the electronic wavefunction changes smoothly. The eigenvalue of Eq. (2.6) is a function that depends on the nuclear coordinates and is known as the adiabatic potential energy surface. The electrons follow the nuclei trajectories instantaneously and transitions between electronic surfaces due to distortions of the nuclei are not allowed in this framework. The Born-Oppenheimer approximation is used throughout theoretical and computational chemistry as it simplifies the calculation of electronic dynamics and other properties and is generally valid. For example, it has been used to accurately calculate the optical excitation energies of short and mid-length conjugated polymers.[73]

This work primarily focuses on the electronic or fermionic degrees of freedom of conjugated systems. A convenient formalism for fermionic systems is second quantisation. The Born Oppenheimer Hamiltonian, Eq. (2.6), can be recast in second quantisation as,

$$\hat{H}_{BO} = \sum_{i,j,\sigma}\tilde{t}_{ij}(\hat{c}^\dagger_{i\sigma}\hat{c}_{j\sigma} + \hat{c}^\dagger_{j\sigma}\hat{c}_{i\sigma}) + \frac{1}{2}\sum_{i,j,k,l,\sigma,\sigma'}\tilde{V}_{ijkl}\hat{c}^\dagger_{i\sigma}\hat{c}^\dagger_{j\sigma'}\hat{c}_{l\sigma'}\hat{c}_{k\sigma} + \frac{1}{2}\sum_{\alpha\neq\beta}\frac{Z_\alpha Z_\beta}{|\mathbf{R}_\alpha - \mathbf{R}_\beta|}, \tag{2.8}$$

where $\hat{c}^\dagger_{i\sigma}(\hat{c}_{i\sigma})$ creates(destroys) an electron with spin σ in orbital i. Due to the Pauli principle, these fermionic operators satisfy anti-commutation relationships,

which are $\{\hat{c}_i, \hat{c}_j^\dagger\} = \delta_{ij}$, $\{\hat{c}_i, \hat{c}_j\} = 0$ and $\{\hat{c}_i^\dagger, \hat{c}_j^\dagger\} = 0$. $\tilde{t}_{ij}$, is the one-electron integral,

$$\tilde{t}_{ij} = \int d^3\mathbf{r}\psi_i(\mathbf{r}) \left[\frac{\mathbf{p}^2}{2m} - \sum_\alpha \frac{Z_\alpha}{|\mathbf{R}_\alpha - \mathbf{r}|}\right] \psi_j(\mathbf{r}), \tag{2.9}$$

and $\tilde{V}_{ijkl}$ is the two-electron integral,

$$\tilde{V}_{ijkl} = \int\int d^3\mathbf{r}d^3\mathbf{r}'\psi_i^*(\mathbf{r})\psi_j^*(\mathbf{r}')\frac{1}{|\mathbf{r} - \mathbf{r}'|}\psi_k(\mathbf{r})\psi_l(\mathbf{r}'). \tag{2.10}$$

The first term in Eq. (2.8) represents the transfer of a spin σ electron from orbital i to orbital j and in the case where $i = j$, it corresponds to an on-site energy. Meanwhile, the second term in Eq. (2.8) represents the electron-electron interactions. When $i = j$ and $k = l$, this term becomes the direct Coulomb interaction between an electron in orbital i and an electron in orbital k. The other terms are discussed in the following section.

2.1.2 Treatment of σ and π electrons

Eq. (2.8) describes all the electron degrees of freedom for any system regardless of energy or symmetry which differ significantly between σ and π electrons. The carbon atoms that make up π-conjugated systems are usually sp^2 hybridised. In a linear conjugated molecule such as butadiene, the sp^2 orbitals form σ bonds along the chain (Fig. 2.1). The p_z orbitals, centred on each carbon atom, combine throughout the molecule to form a delocalised π-system, limiting rotation around the σ bonds. Neighbouring atoms that interact via σ and π orbitals form double bonds.

Greater orbital overlap in σ bonds leads to greater bond strength than π bonds, with $\sigma \rightarrow \sigma^*$ transitions requiring 10 eV of excitation energy compared to 2-3 eV for $\pi \rightarrow \pi^*$. Excitations of interest are limited to π transitions since the breaking of sigma bonds severely distorts the molecule and can lead to chemical breakdown.

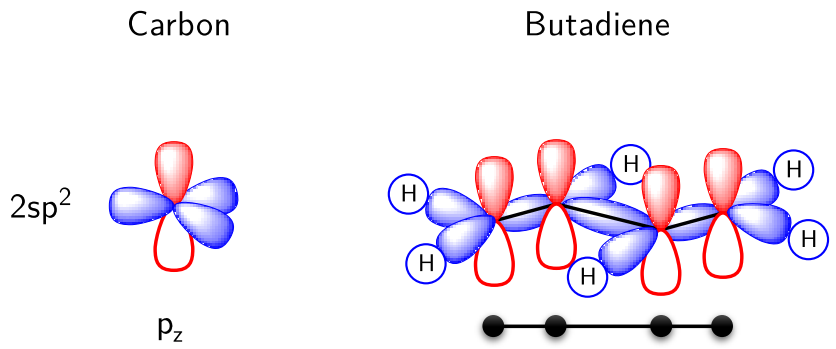


Figure 2.1: An orbital representation of a single carbon atom (left) and butadiene (right), with only large lobes shown for simplicity. Blue shading represents σ orbitals which are in the plane of the molecule, while red shading represents p^z orbitals that are perpendicular to the σ bonds. These combine and form a delocalised π-system over the whole carbon chain. In effective models of π conjugated systems, molecules are represented as a 1D chain of sites (black chain). Each site represents a species or moiety (usually CH) contributing a p_z orbital to the π-system.

The disparity in energy scale is such that σ electrons can be treated implicitly while π-electrons are treated explicitly, leading to simplification of Eq. (2.8). In addition, σ and π electrons span different irreducible representations (symmetry is discussed in Sec. 2.1.5) and therefore contribute to differing blocks of the Hamiltonian.

Effective π-electron models comprise a chain of sites, with each site representing a CH group with one p_z orbital. On average, for a neutral molecule, there is one electron for every site. The σ electrons screen π-π, electron-nuclear and nuclear-nuclear interactions and this screening should be included parametrically in effective π-electron models. $V_p(\mathbf{r};\mathbf{R})$ is defined as a pseudopotential that models the screened interactions between the π-electrons and the nuclei, while $V_{e-e}^{eff}(\mathbf{r}-\mathbf{r}')$ is introduced to describe the electron-electron interactions. Together this leads to the following definitions for the one-electron integral,

$$\tilde{t}_{ij} = \int d^3\mathbf{r}\psi_i(\mathbf{r}) \left[\frac{\mathbf{p}^2}{2m} - V_p(\mathbf{r};\mathbf{R})\right] \psi_j(\mathbf{r}), \tag{2.11}$$

and the two-electron integral,

$$\tilde{V}_{ijkl} = \int\int d^3\mathbf{r}d^3\mathbf{r}'\psi_i^*(\mathbf{r})\psi_j^*(\mathbf{r}')V_{e-e}^{eff}(\mathbf{r}-\mathbf{r}')\psi_k(\mathbf{r})\psi_l(\mathbf{r}'). \tag{2.12}$$

Two-electron integrals are dominated by diagonal terms which include the interaction between two electrons in the same spatial orbital, defined as,

$$U_i = \tilde{V}_{iiii} = \int\int d^3\mathbf{r}d^3\mathbf{r}'|\psi_i(\mathbf{r})|^2V_{e-e}^{eff}(\mathbf{r}-\mathbf{r})|\psi_i(\mathbf{r}')|^2, \tag{2.13}$$

and the interactions between an electron in orbital ψ_i and ψ_j, defined as,

$$V_{ij} = \tilde{V}_{ijij} = \int\int d^3\mathbf{r}d^3\mathbf{r}'|\psi_i(\mathbf{r})|^2V_{e-e}^{eff}(\mathbf{r}-\mathbf{r})|\psi_j(\mathbf{r}')|^2. \tag{2.14}$$

There are additional terms, such as the exchange term ($\tilde{V}_{ijji}$), density-dependent hopping ($\tilde{V}_{iiii+1}$) and bond charge repulsions ($\tilde{V}_{i,i+1,i+1,i}$). However, these terms are small due to the limited wavefunction overlap ($\psi_i^*(\mathbf{r})\psi_j(\mathbf{r})$) and therefore ignored during the fitting of π-model parameters to experimental values. These models which ignore off-diagonal terms are referred to as complete neglect of differential overlap (CNDO) or zero differential overlap (ZDO) models.

Further simplifications can be made by assuming that one-electron integrals are only non-zero for the same or neighbouring orbitals. Thus,

$$\epsilon_i \equiv \tilde{t}_{ii}, \tag{2.15}$$

is defined as the on-site potential energy, and

$$t_i \equiv -\tilde{t}_{ij}, \tag{2.16}$$

is the nearest neighbour (hopping) integral.

Gathering these approximations together, the $\pi-$electron Born-Oppenheimer Hamiltonian is given as:

$$\begin{aligned}\hat{H}^{\pi}_{BO} = &\sum_i \epsilon_i \hat{N}_i - \sum_{i,\sigma} t_i \left(\hat{c}^{\dagger}_{i+1\sigma}\hat{c}_{i\sigma} + \hat{c}^{\dagger}_{i\sigma}\hat{c}_{i+1\sigma}\right) \\ &+U\sum_i \hat{N}_{i\uparrow}\hat{N}_{i\downarrow} + \sum_{i\neq j} V_{ij}\hat{N}_i\hat{N}_j + V_{n-n},\end{aligned} \tag{2.17}$$

where $\hat{N}_i = \sum_\sigma \hat{N}_{i\sigma}$ and $\hat{N}_{i\sigma} = \hat{c}^{\dagger}_{i\sigma}\hat{c}_{i\sigma}$. N_i is the number operator which counts the electrons on site i. Hamiltonians of this basic form will be used throughout this thesis. This implies, we are treating the linear π-conjugated systems as one dimensional. However, despite this simplification the many electron-electron interactions make the model difficult to solve, in addition for realistic models we must include electron-nuclear coupling.

2.1.3 Electron-nuclear coupling

So far this simplified model of the π-electronic degree of freedom neglects the effect of electron-nuclear coupling. Exploiting this Born-Oppenheimer model as a starting point, more sophisticated models can be developed to explicitly considering electron-nuclear coupling.

The effective pseudopotential, $V_p(\mathbf{r}, \mathbf{R})$, describes the effective π-electron-nuclear interactions, including shielding by σ-electrons. This potential can be expanded about a reference geometry, $\mathbf{R^0}$:

$$V_p(\mathbf{r}; \mathbf{R}) = V_p(\mathbf{r}; \mathbf{R^0}) + \sum_l \frac{\partial V_p(\mathbf{R}^0)}{\partial \mathbf{R}_l} \cdot \mathbf{u_l} + \cdots, \tag{2.18}$$

where $\mathbf{u}_l = \mathbf{R}_l - \mathbf{R}^0_l$ is the displacement of the lth nucleus from its reference position. We can then define ϵ^0_i as in Eq. (2.15) at nuclear position $\mathbf{R}^0_i$ and similarly for t^0_i.

The change to one-electron integrals due to changes in geometry is:

$$\alpha_{mnl} = \int \psi_m^*(\mathbf{r}) \left[\frac{\partial V_p(\mathbf{r}; \mathbf{R^0})}{\partial \mathbf{R}_l} \right] \psi_n(\mathbf{r}), \tag{2.19}$$

We further define,

$$\alpha \equiv \alpha_{l,l+1,l} = \alpha_{l+1,l,l} = -\alpha_{l,l+1,l+1} = -\alpha_{l+1,l,l+1}, \tag{2.20}$$

and

$$\beta \equiv \alpha_{l,l,l+1} = -\alpha_{l,l,l-1}, \tag{2.21}$$

the above leads the electron-nuclear interaction in 1D to be given by,

$$\hat{H}_{e-n} = \sum_{i\sigma} \{-\alpha(u_i - u_{i+1})(\hat{c}_{i\sigma}^\dagger \hat{c}_{i+1\sigma} + \hat{c}_{i+1\sigma}^\dagger \hat{c}_{i\sigma}) + \beta(u_{i+1} - u_{i-1})\hat{N}_{i\sigma}\}. \tag{2.22}$$

The first term can be interpreted as the change in electronic kinetic energy due to changes in bond length from their reference values. The second term is the change in electronic potential energy due to the changes in bond length.

2.1.4 Nuclear-nuclear interactions

The contributions from the nuclear-nuclear interactions can be described as,

$$\hat{H}_{n-n} = \sum_\alpha \frac{P_\alpha^2}{2M_\alpha} + V_n(\mathbf{u}_n), \tag{2.23}$$

where $V_n(\mathbf{u}_n)$ represents the effective nuclear-nuclear potential. High energetic barriers mean that distortions from the reference geometry are small, and each bond can therefore be approximated as a spring. Expanding around the average bond

length and keeping only the quadratic and linear terms leads to,

$$V_{\sigma n} = \frac{K}{2}\sum_i (u_{i+1} - u_i)^2 + K\delta r(u_{i+1} - u_i) - \frac{NK(\delta r)^2}{2}, \tag{2.24}$$

where δr is the average change in bond lengths caused by the π-electrons and K is the elastic spring constant of an average bond.

2.1.5 Symmetries

Having established these energetic terms, an effective model must also consider molecular symmetries. While symmetries are approximations for real dynamic systems, they can be useful for distinguishing different states of the model. Both ground and excited states of polyenes can be described as having spatial and electron-hole symmetries, which are introduced in this section.

Spatial symmetries

The majority of even chain length polyene systems possess an axis of two-fold rotation symmetry (C_2) and a centre of inversion (i). The C_2 axis is through the centre and perpendicular to the plane of the molecule. The inversion operator can be described as $\mathbf{r} \mapsto -\mathbf{r}$.

C_{2h}	E	C_2	i	σ_h
A_g	1	1	1	1
B_g	1	-1	1	-1
A_u	1	1	-1	-1
B_u	1	-1	-1	1

Table 2.1: Character table of the C_{2h} point group. E, C_2, i, σ_h are identity, two-fold rotation, inversion and reflection symmetry operations respectively.

Electronic states can be symmetric (eigenvalue 1) or antisymmetric (eigenvalue

-1) with regard to each symmetry operation (Table 2.1). Atomic p_z orbitals of π-conjugated systems are anti-symmetric with respect to the mirror plane and therefore must be of a_u or b_g irreducible representation (Table 2.1). The symmetry character of molecular wavefunctions from combined p_z orbitals must follow the irreducible representation multiplication rules as follows:

$$\begin{aligned} a_u \otimes a_u = b_g \otimes b_g = A_g \\ b_g \otimes a_u = a_u \otimes b_g = B_u \end{aligned} \tag{2.25}$$

Thus, all neutral even chain symmetric polyenes excited states have either A_g or B_u symmetry, while neutral odd chains have either A_u or B_g.

Electron-hole symmetry

Another symmetry that may distinguish between states is electron-hole symmetry, which is an example of particle-hole symmetry. For a Hamiltonian to have electron-hole symmetry, it must be invariant to the transformation of an electron to a hole. This is described by the electron-hole operator, $\hat{J}$:

$$\hat{c}^\dagger_{i\sigma} \mapsto (-1)^i \hat{c}_{i\bar{\sigma}} \equiv (-1)^i \hat{h}^\dagger_{i\sigma}, \tag{2.26}$$

where $\hat{h}^\dagger_{i\sigma}$ creates a hole with spin σ, and $\bar{\sigma}$ refers to spin opposite to σ. Implementation of electron-hole symmetry and, therefore, $\hat{J}$ within DMRG is discussed in the following chapter.

There are requirements on both kinetic energy and electron-electron interactions for a system to possess electron-hole symmetry. The former requires that the model chain or lattice consists of two neighbouring sublattices, i.e. the lattice is required to be bipartite, resulting in the kinetic energy spectrum being symmetric about 0.

The second requirement for electron-hole symmetry is that electron-electron interactions must balance with the electron-nuclei interactions. For an open-chain, electrons in the centre of the chain experience a more substantial nuclear potential due to larger nuclei density. This is balanced by an increase in electron-electron repulsion for the middle sites, resulting in every site across the chain experiencing an equivalent potential. The models considered so far possess electron-hole symmetry which is sometimes referred to as charge-conjugation symmetry.[74]

For the π-conjugated models considered in this thesis, the electron-hole symmetry is exact; however for real systems, it remains an approximation.[75] In particular, the symmetry is strongly disrupted by the presence of heteroatoms, for instance, in donor-acceptor polymers.

State labels and quantum numbers

The convention for describing ground and excited states of π-conjugated systems uses the term symbol $n^{m_s}X^{\pm}$, where:

- n is the overall quantum number of the state.
- m_s is the spin multiplicity of the state, $p = 1, 3, 5$ for singlets, triplets and quintets, respectively.
- X refers to the C_2 spatial symmetry, $X = A_g, B_u$ for even and odd symmetries.
- $\pm$ refers to the electron-hole symmetry. In the literature, there is a difference between the *chemist* notation[74] and the *physicist* notation.[58] This thesis adopts the chemist notation with the even chain ground state labelled "-" and the optical state labelled "+".

2.2 Electronic states in polyenes

Conjugated polyenes can be considered one-dimensional materials. However, this low dimensionality does not mean that understanding their excited states is simple because electron-electron and electron-nuclear interactions cause a multitude of complicated phenomena.[58] This section will provide a qualitative introduction to the low energy states in polyenes which are important for singlet fission, discussing the Peierls distortion and introducing solitons (conjugated bond defects) as a framework to analyse excited states.

2.2.1 Peierls distortion

Electron-nuclear coupling causes the nuclei in conjugated systems to distort from a reference geometry. Early work on nuclear distortions in 1D materials was conducted by Peierls,[76] who found that a 1D metallic chain of uniformly spaced atoms is unstable to nuclear distortions. These distortions break the degeneracy of the chain and belong to a larger class of symmetry-breaking transitions which include the Jahn-Teller effect.[77]

Since polyenes can be represented by a 1D chain of nuclei, Peierls' theory predicts their ground state would undergo transition from a uniform chain (with translational symmetry and repeat unit length of a, Fig. 2.2a, left) to a distorted one (Fig. 2.2a, right). The uniform chain is termed undimerised and the distorted chain dimerised. In undimerised chains, orbitals combine to form a single band with each atom contributing one electron, leaving the band half-filled (Fig. 2.2b).

In dimerised chains, each atom has moved by distance, δ, and the chain now comprises of alternating short (a-δ) and long (a+δ) bonds. The lattice remains periodic; however, the translational symmetry has been reduced with the dimerised

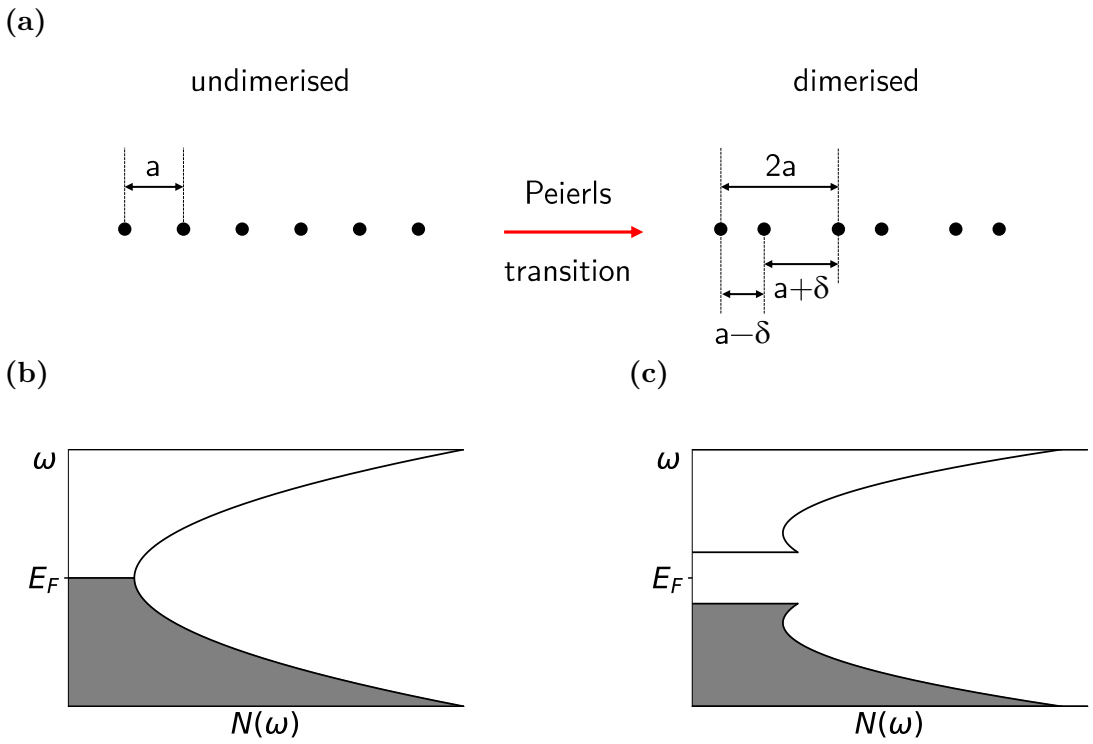


Figure 2.2: **(a)** The Peierls transition proceeds from an undimerised chain with periodicity, a (left) to a dimerised (distorted) chain, with periodicity $2a$ (right). **(b)** Density of states of an uniform chain. **(c)** Density of states of a dimerised chain.

repeat unit length being $2a$ compared to a. This distortion leads to the formation of a gap in the density of states, creating two bands (Fig. 2.2c). All electron states below the gap are filled, and all above are empty, hence the system becomes an insulator.

The electronic energy of the system is lower in the dimerized chain than in the undimerized chain, but is accompanied by an increase in nuclear energy. However, this increase is smaller than the decrease in electronic energy, making the Peierls transition favourable.

Overall, the Peierls transition explains the double bond alternation in linear conjugated systems which gives rise to ground states with $1^1A_g^-$ symmetry.

2.2.2 Broken symmetry

The low-energy states of π-conjugated systems, such as the Peierls distorted ground state, have lower symmetry than that of the Hamiltonian describing the system and are accordingly termed broken symmetry states. Broken symmetry states are widely found throughout nature and lead to interesting phenomena such as superconductivity.[78] The electronic states of polyenes display three main kinds of broken symmetries; spin-density waves, charge-density waves and bond-order waves. For each of the broken symmetries, there is a corresponding observable with long range correlations. For the spin density wave, the observable is,

$$\hat{S}_l^z \equiv \hat{N}_{l\uparrow} - \hat{N}_{l\downarrow}, \tag{2.27}$$

for the charge density wave, the observable is given by,

$$\hat{N}_l \equiv \hat{N}_{l\uparrow} + \hat{N}_{l\downarrow}, \tag{2.28}$$

while for the bond-order wave, the observable is,

$$\hat{T}_l \equiv \left(\hat{c}_{l\sigma}^\dagger \hat{c}_{l+1\sigma} + \hat{c}_{l+1\sigma}^\dagger \hat{c}_{l\sigma}\right). \tag{2.29}$$

These long-range correlations still result in periodicity; however, the periodicity is lower than the that of Hamiltonian of the system. In dimerised 1D systems, bond-order and spin-density waves can co-exist. Mazumdar and Campbell studied the effect of electron-electron interactions in 1D chains; they found the PPP (Pariser-Pople-Parr) model, a commonly used effective π model, used with an Ohno potential (described later) always leads to a bond-order/spin density ground state over a charge-density wave ground state.[79]

2.2.3 Solitons

In polyenes, electronically excited states will lower their energy by distorting from the ground state dimerized geometry. In some cases, the ground state bond alternations can be reduced or reversed over a section of the linear chain. These bond defects in conjugated polymers were first recognised by Ooshika[80] and Longuet-Higgins.[81] These studies probed non-interacting models, but when electron-electron interactions are included, solitons remain important features of excited states.[82,83]

Odd chains

In discussing solitons, it is first worth considering an odd number site chain. In such chains, there can be two phases to the bond alternation along the chain, labelled A and B, shown in Fig. 2.3. End effects mean that short bonds at the ends of chains are preferred, and in an odd site chains it is not possible to meet this preference without a bonding defect. To achieve short bonds at both ends, the bonding phase must change along the chain. In neutral odd chains, this can be done via a neutral soliton, as shown in Fig. 2.3. Solitons in linear conjugated systems can be of two types, radical solitons and ionic solitons. These different types of solitons are associated with varying occupations of mid-gap states.[84]

For an odd site chain of length, N, there are $(N-1)/2$ states in each of the conduction and valence bands. There is an additional mid-band state of energy zero. Single occupation of this state corresponds to a radical neutral soliton while double or zero occupation corresponds to a charged ionic solitons (Fig. 2.4).

Even chains

For even chains, in order to ensure short bonds at either end, the formation of a soliton is accompanied by the creation of a second soliton called an antisoliton (Fig.

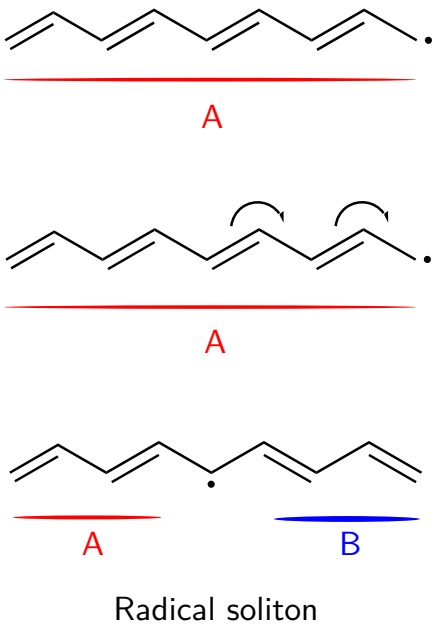


Figure 2.3: The two altering bond phases A and B. The need for double bonds at the end of the chain requires a change in bonding phase. The formation of a neutral soliton from a phase A chain is shown.

2.5). In neutral even chains, both radical and ionic solitons can form (Fig. 2.5). After formation, solitons can migrate through the chain. The soliton-antisoliton pair can also come together again and annihilate to reform a double bond. Ionic solitons are often more bound than radical solitons due to Coulombic interactions, limiting their migration and lattice distortion. Radical solitons, however, can couple to bond order and spin density waves, leading to much stronger lattice relaxation.[58]

Excited states can consist of multiple soliton-antisoliton pairs. In polyenes, the optically excited state is the $1^1B_u^+$ state, which couples to the ground state via the dipole operator. This state is primarily made up of ionic solitons. The lowest triplet state is the $1^3B_u^-$, state and it consists of radical solitons. The lowest energy singlet, $2^1A_g^-$, is a made up of a combination of radical and ionic soliton.

In even site chains, solitons are again associated with mid-gap states. In an even chain, there are two mid-gap states symmetrical spaced about zero; shown in Fig. 2.6, which also shows how the lowest excited electrons occupy these states. Formation of the $1^1B_u^+$ bright singlet state is associated with a single excitation,

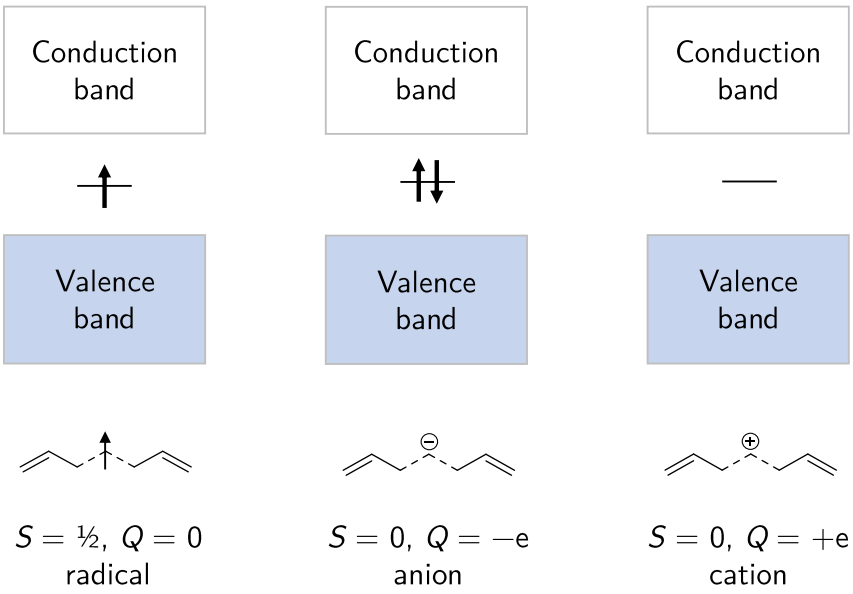


Figure 2.4: The mid-gap state of an odd site chain

while formation of the $2^1A_g^-$ single state is a double excitation event.

2.2.4 Spinons

Solitons represent just one class of fundamental excitation of π-conjugate systems. Other excitations of interest include spinons and magnons, which are particularly important in modelling triplet and triplet-pair states. To motivate these, we consider the strong coupling limit, $U \gg t$, of the PPP Hamiltonian. In this limit, the energies of charge-transfer (ionic) excitation state diverge strongly from the energy of the spin-density-wave (covalent) excitations. The covalent degrees of freedom are described by a low-energy dimerized Heisenberg antiferromagnet model, the effective Hamiltonian of which is given by,

$$\hat{H} = \sum_i J_i \mathbf{S}_i \cdot \mathbf{S}_{i+1}, \tag{2.30}$$

where,

$$\mathbf{S}_i = \sum_{\rho\rho'} c_{i\rho}^\dagger \sigma_{\rho\rho'} c_{i\rho}, \tag{2.31}$$

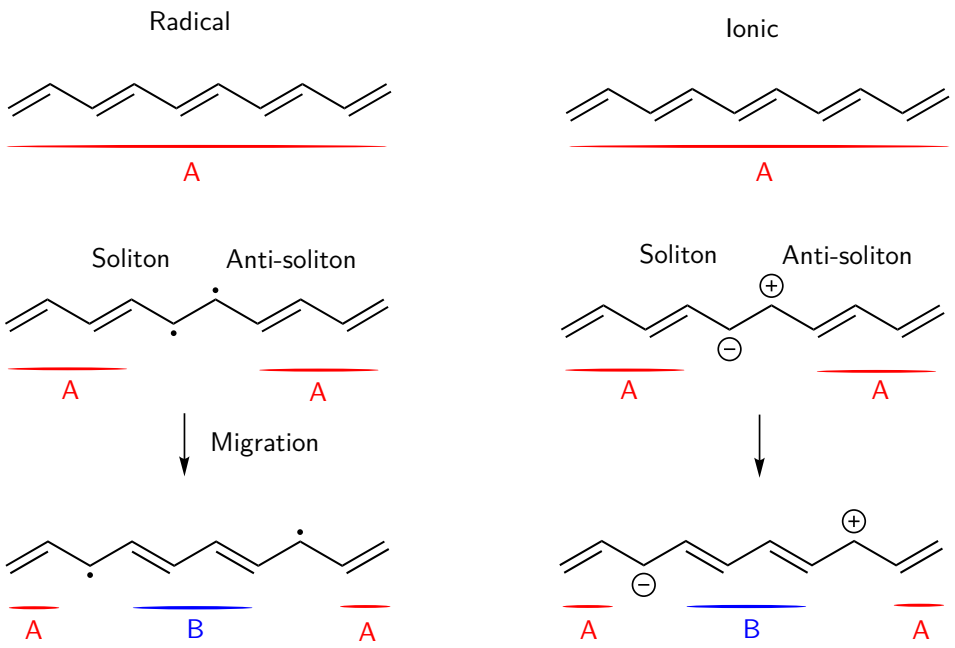


Figure 2.5: Production of soliton and antisoliton pairs in even site chain. Solitons can be radical, which are associated with an unpaired spin, or ionic, which are associated with a charged ion.

σ are Pauli spin matrices,

$$J_i = \frac{4t^2(1 - 2\delta_i + \delta_i^2)}{U - V_1}, \tag{2.32}$$

and δ_i is a measure of the dimerisation of the ith bond, its magnitude ranges from 0 to 1. We consider a fixed geometry with a staggered dimerisation such that $\delta_i = \delta(-1)^i$. We can then define the *dimer limit*, where $0 \ll \delta \lesssim 1$.

In this case, the chain is composed of alternating 'strong' and 'weak' bonds. In the ground state, each strong bond can be considered as a singlet dimer. A triplet or magnon, excitation ($S = 1$) can break a strong bond and has energy cost of J. The triplet excitation comprises of two strongly bound spin-1/2 objects, known as spinons.[85] In polyenes this state is labelled $1^3B_u^-$. The first excited singlet state ($S = 0$) has two broken bonds and costs energy $2J$ and corresponds to the covalent components of the $2^1A_g^-$ state. Both excitations are illustrated in Fig. 2.7.

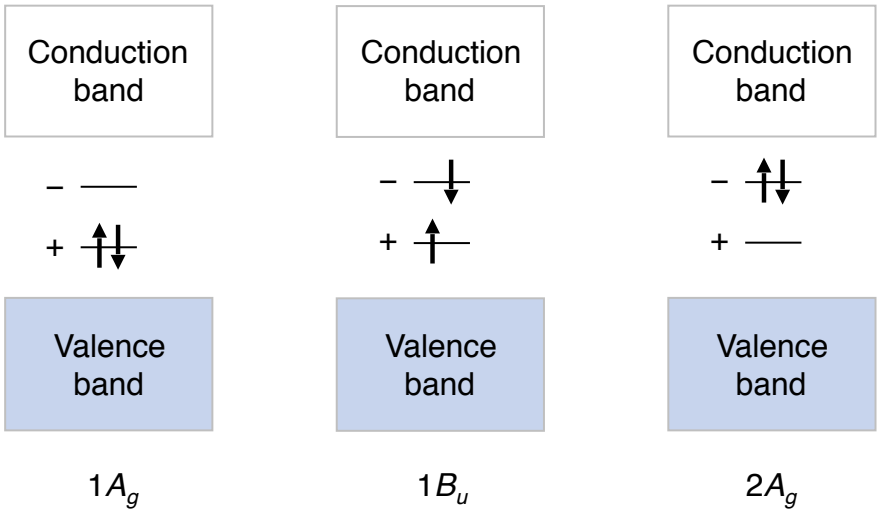


Figure 2.6: The mid-gap state of an even site chain

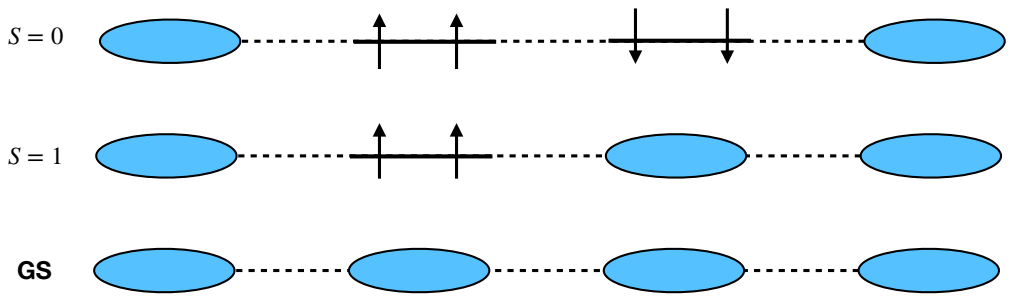


Figure 2.7: A schematic representation of the ground state and the lowest triplet and singlet excitations of the dimerized quantum antiferromagnet. The ovals represent singlet dimers on the strong bonds. This is an example of a valence bond representation.

Chapter 3

Computational Methods

This chapter describes the computational methods used to solve the models introduced in the previous chapter. The single-site basis set for the π-conjugated models has a dimension size of 4, corresponding to the states; $|0\rangle$, $|\uparrow\rangle$, $|\downarrow\rangle$ and $|\uparrow\downarrow\rangle$ and therefore the Hilbert space of even the shortest carotenoids, ($N = 18$, $N^4 \approx 7 \times 10^{10}$), is too large to solve exactly in reasonable time scales. Approximations are required, and one of the most useful for strongly correlated 1D systems is the density matrix renormalisation group (DMRG) method.[86,87] This method is used throughout this thesis, and this chapter expands on the key theory behind the density matrix renormalisation group,[87] and, in addition, the time-dependent variant[88,89] is introduced, which will be used in Chapters 5 and 6 for the calculation of dynamics. The results presented in Chapters 4-6 were produced by DMRG codes written or modified during my doctoral studies.

3.1 Density matrix renormalisation group

The density matrix renormalisation group method was first proposed by White.[90] This work was motivated by a desire to find a method that could tackle problems where the numerical renormalisation group (NRG) method failed.[91] Since its introduction, DMRG has flourished as a separate field of study, with the development

of dynamical DMRG[92] and time-dependent DMRG.[88,89] The use of DMRG in the chemistry community was pioneered by a number of groups[93–96] with more recent developments being lead by Legeza and co-workers.[97,98] After its initial development as a renormalisation technique, DMRG was connected to the Matrix Product States (MPS) theory.[99,100] Seminal reviews of DMRG have been written by Schollwöck, one covering DMRG from a traditional/renormalisation perspective[101] and another from an MPS perspective.[102] This chapter provides details of the key aspects of the density matrix renormalisation for the simulation of π-conjugated systems, taking a traditional perspective.

Basic theory

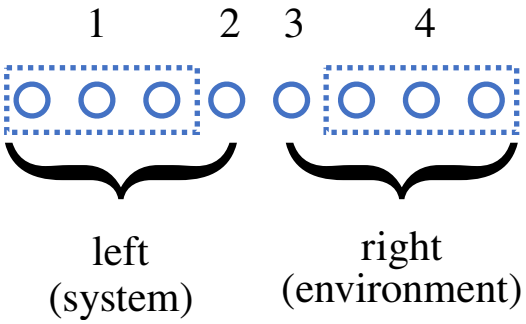


Figure 3.1: Schematic of blocks used in the density matrix renormalisation group. Blocks 1 and 2 form the left (system) augmented block, while blocks 3 and 4 form the right (environment) augmented block.

The density matrix renormalisation group was introduced to calculate an accurate but truncated ground state for problems with large Hilbert spaces. First, we begin by considering a system, made up of sites, that can be partitioned into two continuous blocks. The sites on the left part of the chain will form the left block, l, and the sites of the right part of the chain will form the right block. Note in many discussions of DMRG the blocks are called the system and environment blocks. The left and right blocks combine to form a superblock. For such a system

the untruncated ground state, will be written as,

$$|\Psi\rangle = \sum_{i,j} \Psi_{ij} |i\rangle |j\rangle , \tag{3.1}$$

where i runs over all the states of the left block and j runs over all the states of the right block, the coefficients of the state are Ψ_{ij}. In anticipation of later results, we introduce the reduced density matrix for the left block as,

$$\hat{\rho}_l = \mathrm{tr}_r |\Psi\rangle \langle\Psi| , \tag{3.2}$$

whose elements are given as,

$$\rho_{l_{ii'}} = \langle i | \hat{\rho}_l | i' \rangle = \sum_j \langle ij | \Psi \rangle \langle \Psi | i'j \rangle = \sum_j \Psi_{ij} \Psi^*_{i'j}. \tag{3.3}$$

The reduced density matrix is hermitian, so its eigenvalues are real. Its eigenvalues are also non-negative and the trace of the reduced density matrix equals unity.[103] This matrix can be rotated into its eigenbasis, where the orthonormal eigenvectors are labelled $|\alpha\rangle$ and eigenvalues labelled ω_α:

$$\hat{\rho}_l = \sum_\alpha \omega_\alpha |\alpha\rangle \langle\alpha| . \tag{3.4}$$

Having introduced the reduced density matrix, we now wish to truncate the representation of the state (Eq. (3.1)) so that the left block is now represented by a new basis, $\{\alpha'\}$ where $D_{\alpha'} < D_i$ (D is the dimension of a given basis). We aim to pick m states $|\alpha'\rangle$ such that the distance between the true ground state, $|\Psi\rangle$ and the truncated state, $\left|\tilde{\Psi}\right\rangle$ is minimised,[104]

$$S = \left| |\Psi\rangle - \left|\tilde{\Psi}\right\rangle \right|^2 , \tag{3.5}$$

where,

$$\left|\tilde{\Psi}\right\rangle = \sum_{\alpha'=1}^{m} \sum_{j} \Psi_{\alpha' j} \left|\alpha'\right\rangle \left|j\right\rangle . \tag{3.6}$$

We first consider the singular value decomposition of the ground state coefficients[104,105] such that,

$$\mathbf{\Psi} = \mathbf{U}\mathbf{D}\mathbf{V}^{\dagger}, \tag{3.7}$$

where $\mathbf{U}$ is a $(D_l \times D_r)$ unitary matrix, $\mathbf{V}$ is a $(D_r \times D_r)$ unitary matrix, and $\mathbf{D}$ is a $(D_r \times D_r)$ diagonal matrix, $D_{l/r}$ refers to the dimensionality of the left/right block. The diagonal elements of $\mathbf{D}$ are labelled as $\lambda_{\alpha'}$ and are real and non-negative; these are known as the singular values of $\mathbf{\Psi}$.

Assuming that $D_r \leq D_l$, the coefficients can be written as

$$\Psi_{ij} = \sum_{\alpha'=1}^{D_r} U_{i\alpha'} \lambda_{\alpha'} (V^{\dagger})_{\alpha' j} = \sum_{\alpha'=1}^{D_r} U_{i\alpha'} \lambda_{\alpha'} V^{*}_{\alpha' j}. \tag{3.8}$$

Taking this into account, the wavefunction can be written as

$$\begin{aligned} \left|\Psi\right\rangle &= \sum_{i}^{D_l} \sum_{j}^{D_r} \sum_{\alpha'}^{D_r} U_{i\alpha'} \lambda_{\alpha'} V^{*}_{\alpha' j} \left|i\right\rangle \left|j\right\rangle \\ &= \sum_{\alpha'}^{D_r} \left(\sum_{i}^{D_l} U_{i\alpha'} \left|i\right\rangle \right) \lambda_{\alpha'} \left(\sum_{j}^{D_r} V^{*}_{\alpha' j} \left|j\right\rangle \right), \\ &= \sum_{\alpha'}^{D_r} \lambda_{\alpha'} \left|\alpha'\right\rangle_l \left|\alpha'\right\rangle_r \end{aligned} \tag{3.9}$$

where the states $\left|\alpha'\right\rangle_l = \sum_i U_{i\alpha'} \left|i\right\rangle$ and $\left|\alpha'\right\rangle_r = \sum_j V^{*}_{\alpha' j} \left|j\right\rangle$ define new orthogonal bases, due to the properties of the SVD. The final line of Eq. (3.9) is known as the Schmidt decomposition of state Ψ and the $\left|\alpha'\right\rangle$ states are referred to as the Schmidt basis.[105]

In the Schmidt bases, the reduced density matrices for the left and right blocks

are,

$$\hat{\rho}_l = \mathrm{tr}\,|\Psi\rangle\langle\Psi| = \sum_{\alpha'} \lambda^2_{\alpha'}\,|\alpha'\rangle_l\,\langle\alpha'|_l\,, \tag{3.10}$$

and

$$\hat{\rho}_r = \sum_{\alpha'} \lambda^2_{\alpha'}\,|\alpha'\rangle_r\,\langle\alpha'|_r\,. \tag{3.11}$$

Comparing Eqs. (3.10) and (3.4) we see that the eigenvalues of the reduced density matrices and the square of the singular values are equal, $\omega_\alpha = \lambda^2_{\alpha'}$. Additionally, the Schmidt bases are the eigenvectors of the reduced density matrices, $|\alpha'\rangle \equiv |\alpha\rangle$.

Equipped with this information we return to the original question, which m basis states to use for the state $\left|\tilde{\Psi}\right\rangle$ to best approximate the state $|\Psi\rangle$. Using Eq. (3.5) and the definition of the Schmidt decomposition,

$$S = \left||\Psi\rangle - \left|\tilde{\Psi}\right\rangle\right|^2 = \sum_{ij}\left(\Psi_{ij} - \sum_{\alpha'=1}^{m} U_{i\alpha'}\lambda_{\alpha'}V^*_{\alpha' j}\right)^2. \tag{3.12}$$

From this result,[86] we see that the eigenvectors of the reduced density matrices with the m largest eigenvalues are the optimal bases to represent $|\Psi\rangle$. This is the fundamental result of the density matrix renormalisation group and is key to the infinite and finite algorithm implementations discussed later. The sum of the discarded eigenvalues is referred to as the truncation error.

Blocks, basis sets and Hamiltonian decomposition

In DMRG language, a chain is split into four primitive blocks, as depicted in Fig. 3.1. Blocks 1 and 2 are augmented to form what is sometimes called the system block, here we refer it to as the left block, while block 3 and 4 are augmented to form the environment block, referred to as the right block. Blocks 1 and 4 can represent a number of sites, while blocks 2 and 3 only ever contain a single site. Finally, the full system is described by the augmentation of the left and right blocks into the

superblock.

k	State	Q	$\hat{S}_z$
1	$\|0\rangle$	-1	0
2	$\|\downarrow\rangle$	0	-1
3	$\|\uparrow\rangle$	0	1
4	$\|\uparrow\downarrow\rangle$	1	0

Table 3.1: Mapping of k value to quantum numbers Q and $\hat{S}_z$ for a single site.

In π-conjugated models, each of the states in a block (primitive or augmented) can be described by two quantum numbers, k and n. The quantum number k refers to the charge/spin symmetry sector of the state. k for the states of a single site are given in Tab. 3.1, while n, is an index of states in symmetry sector k. A basis state can therefore be written as $|k_p, n_p\rangle^{(i)}$ where (i) is the label of the block the state belongs to, and p is the label of the edge site of the block. It is worth noting that (i) can be numerical, or be either (l) or (r) indicating the left or right block. If we consider a chain of length $2L+2$ for which the block 1 and 4 are equal in size; the left block is the direct product of the blocks 1 and 2 and given by,

$$|k_{L+1}, n_{L+1}\rangle^{(l)} = |k_L, n_L\rangle^{(1)} \otimes |k_{L+1}, n_{L+1}\rangle^{(2)}\,, \tag{3.13}$$

while the right block is the direct product of blocks 3 and block 4,

$$|k_{L+2}, n_{L+2}\rangle^{(r)} = |k_{L+2}, n_{L+2}\rangle^{(3)} \otimes |k_{L+3}, n_{L+3}\rangle^{(4)}\,. \tag{3.14}$$

By keeping track of $k^{(l)}$ and $k^{(r)}$, a superblock and Hamiltonian can be constructed with certain overall charge (Q) or spin (S^z) eigenvalues. This thesis is primarily concerned with charge-neutral $(Q=0)$, spin-zero $(S^z=0)$ systems and as such when constructing the superblock, we drop the k label, since only certain combinations of

$k^{(1)}, k^{(2)}, k^{(3)}, k^{(4)}$ are allowed. A state represented in the superblock basis is given as (we drop the k notation for compactness),

$$\begin{aligned}
|\Psi\rangle &= \sum_{n_L^{(1)}, n_{L+1}^{(2)}, n_{L+2}^{(3)}, n_{L+3}^{(4)}} \Psi_{n_L^{(1)}, n_{L+1}^{(2)}, n_{L+2}^{(3)}, n_{L+3}^{(4)}} |n_L\rangle^{(1)} \otimes |n_{L+1}\rangle^{(2)} \otimes |n_{L+2}\rangle^{(3)} \otimes |n_{L+2}\rangle^{(4)} \\
&= \sum_{n_{L+1}^{(l)} n_{L+2}^{(r)}} \Psi_{n_{L+1}^{(l)} n_{L+2}^{(r)}} |n_{L+1}\rangle^{(l)} \otimes |n_{L+2}\rangle^{(r)} \\
&= \sum_{ns} \Psi_{n_s} |n_s\rangle ,
\end{aligned} \tag{3.15}$$

where n_s is the index of the superblock states.

Since the basis of the system has been partitioned, we can also partition the Hamiltonian into terms which act only on sites within a block (intra-block Hamiltonian) and terms which act between blocks (inter-block Hamiltonian),

$$\hat{H} = \underbrace{\hat{H}_l + \hat{H}_r}_{\text{intra-block}} + \underbrace{\hat{H}_{lr}}_{\text{inter-block}} . \tag{3.16}$$

Decomposing the Hamiltonian in this manner speeds up its application to states.

3.1.1 Infinite and finite algorithms

To use the DMRG method on a large chain, the system must first be built up site by site. This is achieved through the infinite algorithm, which is depicted in Fig. 3.2. The procedure for calculating the ground state of a system using the infinite algorithm is laid out below:

1. The left block, l representing a small lattice of size L is formed as well as the left block Hamiltonian $\hat{H}_l$ and operators $\hat{A}_l$. Similarly a right block, r is formed. In the initial step, the basis of the left and right blocks will be exact.

2. A new left block, l' is formed, the old left block, l becomes block 1, and it is augmented with the single site block 2. H_{L+1} is not explicitly calculated at this point. A new right block is also formed.

3. The superblock is constructed from the augmented blocks, l' and r'. The superblock is of length $2L + 2$. In general, the explicit construction of the superblock Hamiltonian is avoided.

4. The superblock Hamiltonian $\hat{H}^{super}_{2L+2}$ is diagonalised numerically using a sparse matrix routine. In this work, a conjugate gradient algorithm was used. This gives the ground state energy and the ground state eigenvector $|\Psi\rangle$.

5. From $|\Psi\rangle$, the reduced density matrix is formed. This matrix is diagonalised, using a dense matrix routine. The eigenbasis is found and ordered according to the magnitude of the eigenvalues. A new basis is formed by taking the m states with the largest eigenvalues. Note that in the first few iterations of the algorithm the untruncated eigenbasis may be smaller than m, in this case, all basis states are retained, and the calculation will be exact.

6. The operators are transformed onto the reduced bases set for both the left and right. Restart the algorithm from step (2) until the desired length/desired number of sites is reached.

The procedure is not limited to ground state calculations; any state which can be accessed by sparse matrix diagonalisation can be targeted. The calculation of excited states is discussed later.

The infinite algorithm can, in theory, be used to target a chain of any size. However, the truncated basis states produced by the infinite algorithm suffer from a systematic error. If we are targeting a chain of length $2L + 2$, in the final step the left block with have length $L + 1$. The left block will have been formed from a block

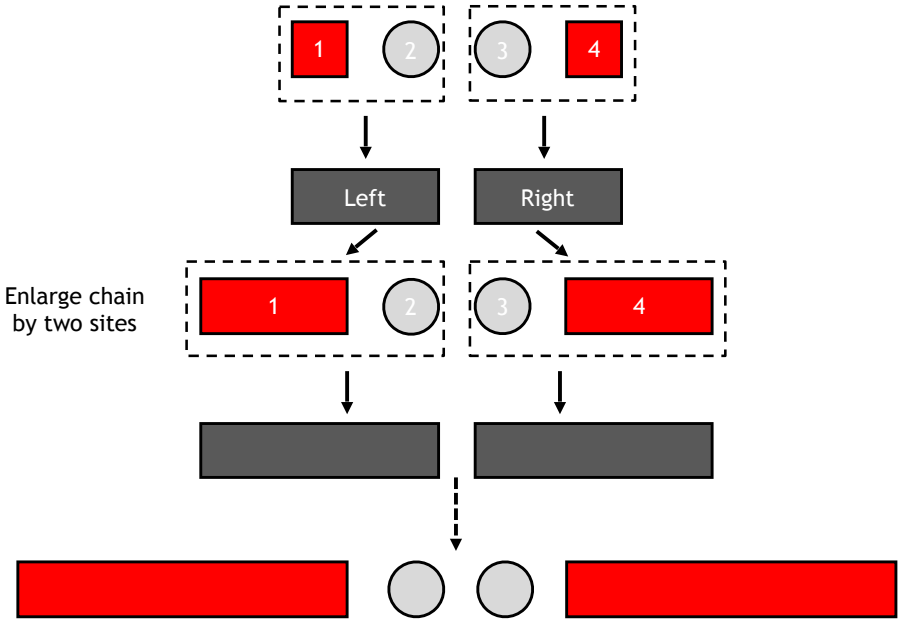


Figure 3.2: A schematic representing the super block construction at each stage in the DMRG infinite algorithm

of length L, found in the previous step, and a single site. Issues arise as the L block already represents a truncated basis found in the previous DMRG step, when the chain was length $2L$. Thus, during the infinite algorithm, the intermediate truncated bases are found embedded in chains that do not represent the targeted chain length and this can cause errors. Additionally, if there is disorder in our system, the potential energy surface may contain local minima. The states that describe the global minima of our $2L + 2$ length chain may already have been discarded; the infinite method is known to get trapped at local minima.[101]

The finite-system DMRG algorithm was introduced to reduce these problems.[90,101] For the finite-system DMRG algorithm, the infinite algorithm is carried out first until the desired length of chain is formed. The superblock will have a fixed length $2L + 2$ throughout the procedure. In contrast with the infinite algorithm, rather than both augmented blocks growing at each step, one block grows as the size of the other is reduced due to the finite routine. The right block is grown first with the left block shrinking, and until the left block can be represented exactly. The left block

is then grown, and the right block is shrunk. The point where both blocks are equal again in size is known as a sweep. Several sweeps may be carried out to improve the accuracy of calculations. The left and right blocks are calculated in a chain of our targeted length and are more accurate than those found during the infinite routine.

Each sweep is typically computationally more expensive than the proceeding infinite calculation though some computational techniques can reduce the cost, such as wavefunction prediction discussed later. Sparse matrix structures, not explicitly storing the Hamiltonian and the parallelisation of some routines were also used in this work to reduce computational expense of both the infinite and finite routines. Fig. 3.3 shows the block structure throughout the sweeping process.

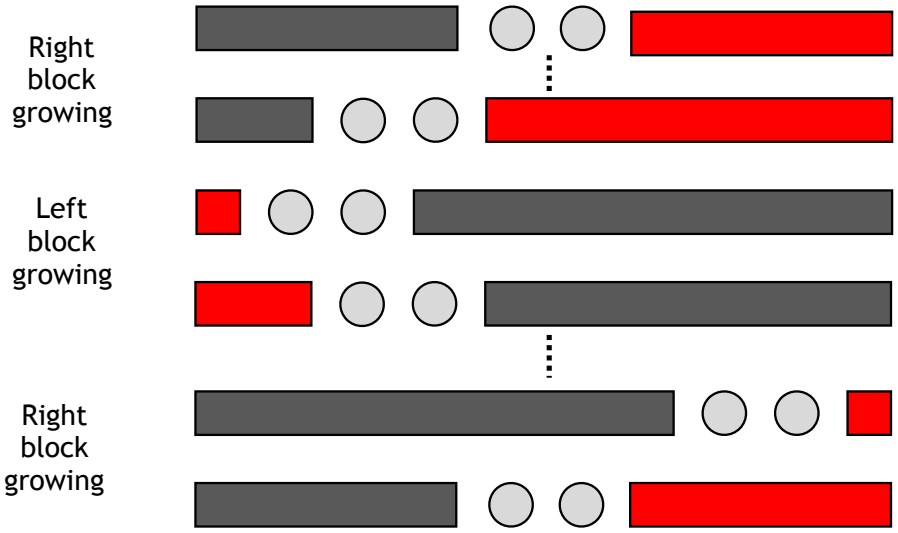


Figure 3.3: A schematic showing the growth and shrinking of the left and right blocks during one finite algorithm sweep.

3.2 Density matrix truncation and the rotation to the new basis

At each step of the DMRG algorithms, the basis set of the growing and shrinking blocks must be truncated and rotated. If we consider the left block to be growing and the right block to be shrinking, they are related to the basis states of blocks in

the previous step by the following relationships:[87,101]

$$\left|n_{L+1}^{(1)}\right\rangle = \sum_{n_L^{(1)},n_{L+1}^{(2)}} \left\langle n_L^{(1)} n_{L+1}^{(2)} \,\middle|\, n_{L+1}^{(1)} \right\rangle \left| n_L^{(1)} n_{L+1}^{(2)} \right\rangle = \sum_{n_L^{(1)},n_{L+1}^{(2)}} (\hat{W}_l)_{n_L^{(1)},n_{L+1}^{(2)},n_{L+1}^{(1)}} \left| n_L^{(1)} n_{L+1}^{(2)} \right\rangle, \tag{3.17}$$

and

$$\left|n_{L+4}^{(4)}\right\rangle = \sum_{n_{L+3}^{(4)},n_{L+3}^{(3)}} \left\langle n_{L+3}^{(4)} \,\middle|\, n_{L+3}^{(3)} n_{L+4}^{(4)} \right\rangle \left| n_{L+3}^{(4)} \right\rangle = \sum_{n_{L+3}^{(4)},n_{L+3}^{(3)}} (\hat{W}_r^\dagger)_{n_{L+3}^{(4)} n_{L+3}^{(3)},n_{L+4}^{(4)}} \left| n_{L+3}^{(4)} \right\rangle, \tag{3.18}$$

where,

$$\left(\hat{W}_l\right)_{n_L^{(1)},n_{L+1}^{(2)},n_{L+1}^{(1)}} = \left\langle n_L^{(1)} n_{L+1}^{(2)} \,\middle|\, n_{L+1}^{(1)} \right\rangle, \tag{3.19}$$

and

$$\left(\hat{W}_r^\dagger\right)_{n_{L+3}^{(4)},n_{L+3}^{(3)},n_{L+4}^{(4)}} = \left\langle n_{L+3}^{(4)} \,\middle|\, n_{L+3}^{(3)} n_{L+4}^{(4)} \right\rangle. \tag{3.20}$$

If only m states are retained, the matrices $\hat{W}_{l/r}$ will have dimensions $D^{(1)/(4)}d \times m$, where d is the dimension of a single site. Additionally, if the basis has already been truncated then $\hat{W}_{l/r} = m$.

Using the above transformation, operators are rotated into the new truncated basis at each step. This can be carried out for the left block as,

$$\begin{aligned}
&\left\langle n_{L+1}^{(1)} \,\middle|\, \hat{O} \,\middle|\, n_{L+1}^{\prime(1)} \right\rangle \\
&= \sum_{n_L^{(1)} n_{L+1}^{(2)}} \sum_{n_L^{\prime(1)} n_{L+1}^{\prime(2)}} \left\langle n_{L+1}^{(1)} \,\middle|\, n_L^{(1)} n_{L+1}^{(2)} \right\rangle \left\langle n_L^{(1)} n_{L+1}^{(2)} \,\middle|\, \hat{O} \,\middle|\, n_L^{\prime(1)} n_{L+1}^{\prime(2)} \right\rangle \left\langle n_L^{\prime(1)} n_{L+1}^{\prime(2)} \,\middle|\, n_{L+1}^{\prime(1)} \right\rangle \\
&= \sum_{n_L^{(1)} n_{L+1}^{(2)}} \sum_{n_L^{\prime(1)} n_{L+1}^{\prime(2)}} \left(\hat{W}_l^\dagger\right)_{n_{L+1}^{(1)},n_L^{(1)},n_{L+1}^{(2)}} \left\langle n_L^{(1)} n_{L+1}^{(2)} \,\middle|\, \hat{O} \,\middle|\, n_L^{\prime(1)} n_{L+1}^{\prime(2)} \right\rangle \left(\hat{W}_l\right)_{n_L^{\prime(1)},n_{L+1}^{\prime(2)},n_{L+1}^{\prime(1)}}.
\end{aligned} \tag{3.21}$$

A similar expression can be defined for operators in the right block.

3.2.1 Wave function prediction

At each step of the chain building and sweeping, a sparse matrix diagonalisation routine is used to find eigenstates. These routines iteratively improve a trial state until convergence is achieved. During the infinite routine, the initial trial state is produced from a random seed. However, during the finite routine, one can use the wavefunction calculated in the previous step. The method of rotating the previous wavefunction into a trial state of the current step was developed by White.[106] By using the White wave function prediction method, the number of diagonalisation iterations can be reduced by a factor of 10. Additionally, the prediction method is key to the adaptive time-dependent DMRG, as discussed later.

Before the change of basis, the targeted eigenstate is written as,

$$|\Psi_L\rangle = \sum_{n_L^{(1)} n_{L+1}^{(2)} n_{L+2}^{(3)} n_{L+3}^{(4)}} \left\langle n_L^{(1)} n_{L+1}^{(2)} n_{L+2}^{(3)} n_{L+3}^{(4)} \middle| \Psi \right\rangle \left| n_L^{(1)} n_{L+1}^{(2)} n_{L+2}^{(3)} n_{L+3}^{(4)} \right\rangle, \tag{3.22}$$

while after the change of basis, the state is given by,

$$|\Psi_{L+1}\rangle = \sum_{n_{L+1}^{(1)} n_{L+2}^{(2)} n_{L+3}^{(3)} n_{L+4}^{(4)}} \left\langle n_{L+1}^{(1)} n_{L+2}^{(2)} n_{L+3}^{(3)} n_{L+4}^{(4)} \middle| \Psi \right\rangle \left| n_{L+1}^{(1)} n_{L+2}^{(2)} n_{L+3}^{(3)} n_{L+4}^{(4)} \right\rangle. \tag{3.23}$$

We make two incomplete basis transformations one for the growing block and one for the shrinking block, such that we approximate $\left\langle n_{L+1}^{(1)} n_{L+2}^{(2)} n_{L+3}^{(3)} n_{L+4}^{(4)} \middle| \Psi_{L+1} \right\rangle \approx$

$\left\langle n^{(1)}_{L+1} n^{(2)}_{L+2} n^{(3)}_{L+3} n^{(4)}_{L+4} \,\middle|\, \Psi_L \right\rangle$, this leads to the rotated coefficients being given by,

$$
\begin{aligned}
&\left\langle n^{(1)}_{L+1} n^{(2)}_{L+2} n^{(3)}_{L+3} n^{(4)}_{L+4} \,\middle|\, \Psi_{L+1} \right\rangle \\
&= \left\langle n^{(1)}_{L+1} n^{(2)}_{L+2} n^{(3)}_{L+3} n^{(4)}_{L+4} \,\middle|\, \Psi_L \right\rangle \\
&= \sum_{n^{(1)}_L n^{(2)}_{L+1} n^{(3)}_{L+2} n^{(4)}_{L+3}} \left\langle n^{(1)}_L n^{(2)}_{L+1} n^{(3)}_{L+2} n^{(4)}_{L+3} \,\middle|\, \Psi_L \right\rangle \left\langle n^{(1)}_{L+1} n^{(2)}_{L+2} n^{(3)}_{L+3} n^{(4)}_{L+4} \,\middle|\, n^{(1)}_L n^{(2)}_{L+1} n^{(3)}_{L+2} n^{(4)}_{L+3} \right\rangle \\
&= \sum_{n^{(1)}_L n^{(2)}_{L+1} n^{(3)}_{L+2} n^{(4)}_{L+3}} \left\langle n^{(1)}_L n^{(2)}_{L+1} n^{(3)}_{L+2} n^{(4)}_{L+3} \,\middle|\, \Psi_L \right\rangle \left\langle n^{(1)}_{L+1} \,\middle|\, n^{(1)}_L n^{(2)}_{L+1} \right\rangle \\
&\underbrace{\left\langle n^{(2)}_{L+2} \,\middle|\, n^{(3)}_{L+2} \right\rangle}_{\delta_{n^{(2)}_{L+2} n^{(3)}_{L+2}}} \left\langle n^{(3)}_{L+2} n^{(4)}_{L+3} \,\middle|\, n^{(4)}_{L+4} \right\rangle \\
&= \sum_{n^{(1)}_L n^{(2)}_{L+1} n^{(2)}_{L+2} n^{(4)}_{L+3}} \left\langle n^{(1)}_L n^{(2)}_{L+1} n^{(2)}_{L+2} n^{(4)}_{L+3} \,\middle|\, \Psi_L \right\rangle \left(\hat{W}^{\dagger}_l\right)_{n^{(1)}_{L+1} n^{(1)}_L n^{(2)}_{L+1},} \left(\hat{W}_r\right)_{n^{(3)}_{L+3}, n^{(4)}_{L+4}, n^{(4)}_{L+3}} .
\end{aligned}
\tag{3.24}
$$

The rotation of the wave function to the new basis has limited computational cost compared to the gain achieved by the reduction in diagonalisation iterations.

3.2.2 Excitations

In the proceeding section, the infinite algorithm was discussed for calculating ground state energies. However, typically excited states are also of scientific interest, as is the case in this thesis. DMRG allows us to target excited states in addition to the ground state. Excited states can be calculated from the superblock Hamiltonian at each step using the sparse matrix diagonalisation routine. To ensure that the excited states, as well as the ground state, are optimally represented by the truncated basis, the excited states are included in the calculation of the reduced density matrix as follows:

$$\hat{\rho} = \mathrm{tr}_l \sum_i \kappa_i \left|\psi_i\right\rangle \left\langle\psi_i\right| , \tag{3.25}$$

where the sum over i contains all the targeted states. $\sum_i \kappa_i$ should equal 1, and it is common to weight all the states the same.

For instance, to calculate the excitation energy of the $2^1A_g^-$ state, during the diagonalisation of the Hamiltonian we would find both the ground state, $\left|1^1A_g^-\right\rangle$ and, via the Gram–Schmidt process, the excited state $\left|2^1A_g^-\right\rangle$. When calculating the reduced density matrix we would include an equal contribution form $\left|1^1A_g^-\right\rangle$ and $\left|2^1A_g^-\right\rangle$ states, such that,

$$\hat{\rho} = \frac{1}{2}\,\mathrm{tr}_l \left|1^1A_g^-\right\rangle \left\langle 1^1A_g^-\right| + \frac{1}{2}\,\mathrm{tr}_l \left|2^1A_g^-\right\rangle \left\langle 2^1A_g^-\right|. \tag{3.26}$$

The truncated basis will be optimised to describe both the $1^1A_g^-$ and $2^1A_g^-$ states.

3.2.3 Symmetries

Symmetries may be used to specifically target ground and excited states. In the case of the π-conjugated models, there are three symmetries in particular which can be used to describe states. These are:

1. **Particle-hole symmetry** - (J_i: $\hat{c}_{i\sigma}^\dagger \mapsto (-1)^i \hat{c}_{i\sigma}$): If a system possesses particle-hole symmetry then $[\hat{H}, \hat{J}] = 0$, where $\hat{J} = \prod_i \hat{J}_i$, and the single site operation is given by $\hat{J}_i \left|0\right\rangle = \left|\uparrow\downarrow\right\rangle, \hat{J}_i \left|\uparrow\right\rangle = (-1)^i \left|\downarrow\right\rangle, \hat{J}_i \left|\downarrow\right\rangle = (-1)^i \left|\uparrow\right\rangle, \hat{J}_{i+1} \left|\uparrow\downarrow\right\rangle = \left|0\right\rangle$. Eigenstates can take eigenvalues ± 1 and are labelled either $+$ or $-$.

2. **Spin flip symmetry** - (P_i: $\hat{c}_{i\sigma}^\dagger \mapsto \hat{c}_{i\bar{\sigma}}^\dagger$): If a system possesses spin-flip symmetry then $[\hat{H}, \hat{P}] = 0$, where $\hat{P} = \prod_i \hat{P}_i$, and the single site operation is given by $\hat{P}_i \left|0\right\rangle = \left|0\right\rangle, \hat{P}_i \left|\uparrow\right\rangle = \left|\downarrow\right\rangle, \hat{P}_i \left|\downarrow\right\rangle = -\left|\uparrow\right\rangle, \hat{P}_i \left|\uparrow\downarrow\right\rangle = \left|\uparrow\downarrow\right\rangle$. Eigenstates can take eigenvalues ± 1. Spin-flip symmetry can be used to differentiate singlet and quintet states from triplet states.

3. C_2 **symmetry**: π-conjugated molecules often posses a two-fold symmetry

rotation axis at the centre of the molecule. The spatial reflection or parity operator, C_2 acts globally. It acts on a superblock state as follows

$$\hat{C}_2 \left| n_1, n_2, n_3, n_4 \right\rangle = (-1)^{\xi} \left| n_4, n_3, n_2, n_1 \right\rangle$$

where the phase is determined by the occupancy of each of the blocks, N_j is the number of electrons in block j and $\xi = (N_1 + N_2)(N_3 + N_4)$. A state may have eigenvalues of ± 1, with respect to this rotation and will be given the symmetry label A_g or B_u. Parity is only a good quantum number during the infinite routine and when the left and right block are equal in size during the finite DMRG.

By using the following equation,

$$\left| \Psi_{\pm} \right\rangle = \frac{1}{2} \left(\left| \Psi \right\rangle \pm \hat{O} \left| \Psi \right\rangle \right), \tag{3.27}$$

trial states with the desired symmetries are produced for the sparse matrix diagonalisation, where $\hat{O} = \hat{P}, \hat{J}, \hat{C}_2$. Each of the targeted symmetries commute for 1D dimensional chains.

With the use of symmetries and targeting of excited states, eigenstates which are involved in singlet fission were studied as discussed in Chapters 4-6.

3.2.4 Why DMRG works: Entanglement, entropy and area law

DMRG can provide remarkable accuracy for 1D dimensional systems even when only a few states are retained; this is in contrast to 2D systems. To understand why DMRG works so well, we first must introduce entanglement.

Entanglement is a property of a state that is composed of two or more quantum objects such as spins. Often quantum systems can be described by linear superposition of basis states. As before, if we consider partitioning our system into two sectors (left, l, which the index i runs over and right, r, which the index j runs over) we found that the wave function can be written as,

$$|\Psi\rangle = \sum_{ij} \Psi_{ij} |i\rangle |j\rangle . \tag{3.28}$$

We can imagine the case where this state is a product state and as such the spins in sector l can be described independently of the spins in sector r;

$$|\Psi\rangle = \left(\sum_{i} \Psi_i |i\rangle \right) \otimes \left(\sum_{j} \Psi_j |j\rangle \right) . \tag{3.29}$$

In this case, sectors l and r are not entangled. However, states which can not be decomposed into products and instead can only be written as linear sums of bases spanning both l and r are entangled. An example for a two spin system is $|\Psi\rangle = \frac{1}{\sqrt{2}}(|\uparrow\rangle_l |\downarrow\rangle_r + |\downarrow\rangle_l |\uparrow\rangle_r)$. We also previously found that states of the form Eq. (3.28), through the use of SVD decomposition can be rewritten as,

$$|\Psi\rangle = \sum_{\alpha=1}^{M} \lambda_\alpha |\alpha\rangle_l |\alpha\rangle_r . \tag{3.30}$$

Here we can see that if $M = 1$, we will have an unentangled state as in Eq. (3.29). The accuracy of truncating the state in Eq. (3.30) entirely depends on the spectrum of the Schmidt coefficients, λ_α. Remembering that λ_α^2 are equal to the eigenvalues of the reduced density matrix, we find that:[105]

- If the eigenvalues of the reduced density matrix decay very fast, little error is introduced by discarding the small weights.

- The number of non-zero eigenvalues corresponds to the amount of entanglement: fewer eigenvalues means less entanglement. A single eigenvalue results in a product state that can be described as disentangled.

- DMRG minimises the loss of information. The Schmidt decomposition concentrates the descriptions of the entanglement into as few as states as possible; thus information loss is minimised when discarding. The closer the target state is to a product state, the greater success DMRG will have.

To quantify the amount of entanglement we have in a system, the von Neumann entanglement entropy is used:[101]

$$S = -\sum_{\alpha} \omega_\alpha \log \omega_\alpha = -\operatorname{Tr}(\hat{\rho}_A \log \hat{\rho}_A). \tag{3.31}$$

The growth of entanglement with systems size is related to the area law which describes why DMRG works so well for 1D systems but is much less efficient for higher dimensions.[107] The area law states that the entanglement entropy of the ground state of a gapped, partitioned system is proportional to the size of the partition between the systems. For 1D systems, the surface between two systems is a point, and this does not change with system size, therefore the entropy, S, is proportional to a constant.[108] While for a 2D system, the area between partitions is a line which will grow with system size, and the entropy, S, is proportional to the 'length', L of the system.[107] Generally the number of states which is needed to accurately represent a state is related to the entanglement entropy, given by:[109]

$$m \approx \exp(S) \tag{3.32}$$

Therefore for 1D systems, the growth in the number of states is small while for 2D

systems increase in system size lead to an exponential increase in required states.

3.2.5 DMRG and MPS

MPS: Matrix product states

In this section, we will connect the states produced by the DMRG algorithm with the theory of matrix product states. Again we start by considering a 1D system of L sites. Each site has a Hilbert of size d. In such a system, a general state is given as a sum of product states, such,

$$\begin{aligned} |\psi\rangle &= |\sigma_1\rangle \otimes |\sigma_2\rangle \otimes \cdots \otimes |\sigma_{L-1}\rangle \otimes |\sigma_L\rangle \\ &= \sum_{\sigma} \Psi_\sigma |\sigma\rangle . \end{aligned} \tag{3.33}$$

Now let us consider a block of this system which represents $l-1$ sites. To represent this state exactly would require d^{l-1} states. We can represent this block by a smaller number of states $m < d^{l-1}$ given by $\{|\beta\rangle_{l-1}\}$. If we were to add a new site to the right of this block to create a block of l sites and $m \times d$ states in its basis. The basis states are generated by products $\{|\beta\rangle_{l-1} \otimes |s_l\rangle\}$. We also introduced a projection operator A_l to generate a new truncated basis. This is written as

$$|\alpha\rangle_l = \sum_{\beta_{l-1}, s_l} A_l^{\alpha_l, (\beta_{l-1}, s_l)} |\beta_{l-1}\rangle \otimes |s_l\rangle , \tag{3.34}$$

where A is indexed by the chain length l and its matrix indices α and (β_{l-1}, s_l) (Note (β_{l-1}, s_l) is a single index). We make a change of notation $A_l^{\alpha_l, \beta_{l-1}}[s_l] \equiv A_l^{\alpha_l, (\beta, s_l)}$ by writing the $m \times (d * m)$ as a set of d $m \times m$ matrices, and we also recursively apply the projection such that Eq. (3.34) is rewritten as,

$$|\alpha\rangle_l = \sum_{s_1 \cdots s_l} (A_1[s_1]A_2[s_2]\ldots A_l[s_{l-1}])^{\alpha,s_1} |s_1 s_2 \cdots s_l\rangle \tag{3.35}$$

We can now consider the DMRG routine, which produces $m \times m$ product states for $|\Psi\rangle$. For instance consider the transformation that produced the left block that terminates on bond l from products of the block terminating at bond $l-1$ and a single sites l, allowing

$$\left\langle \alpha^{(S)}_{n_{l-1}} s_l \right| \left. \alpha^{(S)}_{n_l} \right\rangle \equiv A_l^{n_{l-1}n_l}[s_l], \tag{3.36}$$

such that,

$$\left|\alpha^{(S)}_{n_l}\right\rangle = \sum_{n_{l-1}s_n} A_l^{n_{l-1}n_l}[s_l] \left|\alpha^{(S)}_{n_{l-1}}\right\rangle \otimes |s_l\rangle \,. \tag{3.37}$$

By using backwards recursion and expressing $\left|\alpha^{(S)}_{n_{l-1}}\right\rangle$ in terms of $\left|\alpha^{(S)}_{n_{l-2}}\right\rangle$ etc. we will end up an expression equivalent to Eq. (3.35). A similar expression can be found for the environment block. From these results, we see that the DMRG routine works to generate optimal matrix product states. The DMRG method can be formulated by considering the MPS as the starting point and is reviewed in the following reference [102].

3.3 Time-dependent density matrix renormalisation group

This section will discuss the adaptive time-dependent density matrix renormalisation group method (t-DMRG). This method was developed independently by White and co-workers and Daley and co-workers[88,89] and remains the most widely used time dependent DMRG technique.

To introduce t-DMRG, we first consider the time-dependent Schrödinger equation ($\hbar = 1$),

$$i\frac{\partial}{\partial t}\left|\Psi(t)\right\rangle = \hat{H}\left|\Psi(t)\right\rangle, \tag{3.38}$$

which has the formal solution (in the Schrödinger picture) of,

$$\left|\Psi(t)\right\rangle = e^{-i\hat{H}t}\left|\Psi(t=0)\right\rangle. \tag{3.39}$$

In a DMRG framework, the Hamiltonian, $\hat{H}$ and starting wavefunctions $|\Psi(t=0)\rangle$ are represented in a truncated Hilbert space. Initial attempts to develop time-dependent DMRG methods involved evolving the dynamics in a truncated Hilbert space defined by the starting state $|\Psi(t=0)\rangle$. This method was introduced by Cazalilla and Marston[110] and works well in situations where the evolving state remains similar to the starting state. Improvements can be made to the Cazalilla and Marston method by including additional states in the reduced density matrix which may be more similar to the destination state.[89] However, when the time-evolving state explores an unknown region of the Hilbert space that is not well described by the truncated Hilbert space, this method fails. To address this failure, in the adaptive t-DMRG method, the truncated Hilbert space and the evolving state are both updated at each time step. To allow this, it is convenient for the Hamiltonian used for dynamics to be of a certain form.

3.3.1 Suzuki-Trotter decomposition

One of the fundamental assumptions of the adaptive t-DMRG approach is that the evolving state can be calculated by the successive application of the evolution operator,

$$\left|\Psi(t)\right\rangle = (e^{-i\hat{H}\delta t}\cdots e^{-i\hat{H}\delta t})\left|\Psi(0)\right\rangle. \tag{3.40}$$

Furthermore, when the Hamiltonian consists of only on-site and nearest-neighbour

terms, such as,

$$\hat{H} = \hat{H}_{1,2} + \hat{H}_{2,3} + \hat{H}_{3,4} \cdots \hat{H}_{L-1,L}, \tag{3.41}$$

using the Baker-Campbell-Hausdorff theorem,[111] we can approximate the application of the evolution operator by the following decomposition,

$$e^{-i\hat{H}\delta t} \approx e^{-i\hat{H}_{1,2}\delta t/2} e^{-i\hat{H}_{2,3}\delta t/2} \cdots e^{-i\hat{H}_{L-1,L}\delta t/2} e^{-i\hat{H}_{L-1,L}\delta t/2} \cdots e^{-i\hat{H}_{2,3}\delta t/2} e^{-i\hat{H}_{1,2}\delta t/2}. \tag{3.42}$$

This is known as a Suzuki-Trotter (Trotter) decomposition.[111,112] The order of error for this decomposition is δt^3, and when it applied $N = T/\delta t$ times, the overall error is $\approx \delta t^2$, this is known as the Trotter error and is one of the main errors which affects t-DMRG.[88,113] The local evolution operators, $e^{-i\hat{H}_{i,j}\delta t/2}$ are also known as bond evolution operators.

A bond evolution operator has a dimension of $d \times d$, where d is the local single-site dimension, and its application can be very efficient. Its matrix elements can be expressed as (dropping the k notation for compactness):

$$U^{n_2',n_3'}_{n_2,n_3} = \left\langle n_2', n_3' \right| e^{-i\hat{H}_{i,i+1}\delta t/2} \left| n_2 n_3 \right\rangle. \tag{3.43}$$

To apply the bond evolution operator in a DMRG context, we consider the case when the nearest neighbour interaction takes place between single sites in different DMRG blocks each with a single site, i.e. blocks 2 and 3. Applying the operator to the wavefunction can then be written as,

$$e^{-i\hat{H}_{i,i+1}\delta t/2} \left|\Psi\right\rangle = \sum_{n_1,n_4} \sum_{n_2,n_3} \sum_{n_2',n_3'} \left\langle n_1, n_2, n_3, n_4 \right| \left.\Psi\right\rangle U^{n_2',n_3'}_{n_2,n_3} \left| n_1, n_2', n_3', n_4 \right\rangle. \tag{3.44}$$

3.3.2 t-DMRG algorithm

To use Eq. (3.44), we first prepare an initial state using the finite DMRG algorithm. The state can be an eigenstate of the static Hamiltonian, and dynamics can be induced by changing Hamiltonian parameters or including additional terms. Alternatively, the starting wavefunction can be perturbed with the application of an operator at $t = 0$.

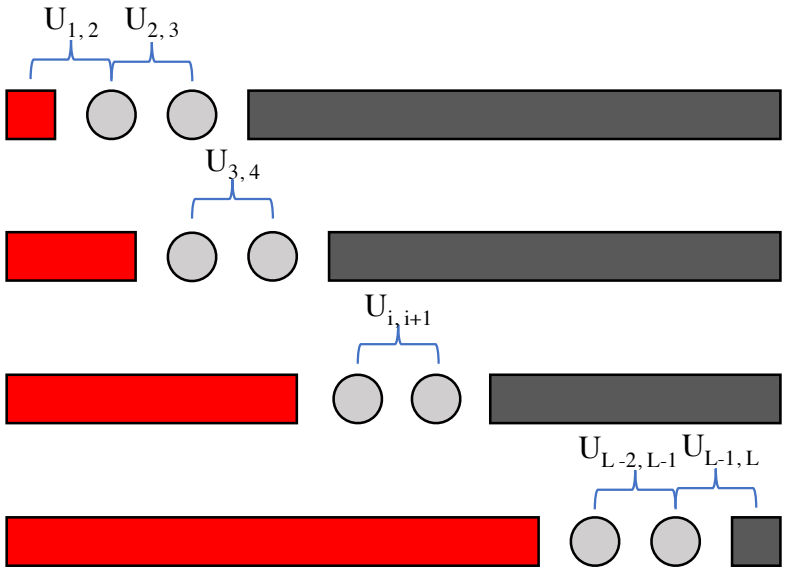


Figure 3.4: A schematic showing the growth and shrinking of the left (system) and right (environment) blocks during one finite algorithm sweep.

The prepared state can then be evolved in time by application of the bond operators. The sweeping routine used during finite DMRG can be used to move sites from block to block and ensure the bond operator is always applied to blocks that contain only single sites. Overall the application of adaptive time-dependent DMRG is described as follows:

1. Generate initial state - The initial state can either be the eigenstate for a Hamiltonian different to the Hamiltonian used for dynamics or an operator can be applied to an eigenstate. This will be generated using the finite DMRG algorithm.

2. Beginning at one end of the chain, an evolution link operator is applied.

3. The reduced density matrix of the growing left or right block is calculated, and the basis is truncated.

4. The operators are rotated into the new basis set.

5. The wavefunction is rotated into the new basis set using the wavefunction prediction method developed by White (Sec. 3.2.1).[106]

6. The above steps are repeated until the end of the chain is reached. Then the previously shrinking block becomes the growing block, and we sweep in the opposite direction, applying the link evolution operators where necessary.

During the infinite and finite algorithm, the Hilbert space is truncated in such a way to best represent the desired eigenstate. During time evolution, this state changes and may no longer be well represented by the basis. The time-dependent density matrix renormalisation algorithm allows both the state and basis set to evolve, with the basis at time t' best representing the state at that time.

Chapter 4

Polyene triplet pair states and their role in singlet fission

4.1 Introduction

The first step of singlet fission in π-conjugated linear polyenes is the internal conversion from the photoexcited $1^1B_u^+$ state to a triplet-pair state, i.e. $^1(TT)$. In polyenes, many low energy excited states have multiple triplet excitation character,[74] and these states are generally dark. As such, the destination triplet-pair state of singlet fission state interconversion is unknown.[27] In this chapter, the candidate states for the singlet fission $^m(TT)$ state are investigated and characterised.

One of the candidate states is the $2^1A_g^-$ state, whose triplet-pair character has been well established in the literature[58,73–75,83,114–116] and this state is often considered as a bound pair of triplet excitations. Other potential states include the $3^1A_g^-$ and $1^1B_u^-$ singlet states and $1^5A_g^-$quintet state.

In extended polyene systems such as polydiacetylene and poly(thienylenevinylene), it has been observed that singlet fission occurs after photoexcitation only when molecules are excited with energy in excess of the band edge, with isolated triplet signatures appearing in transient absorption spectroscopy measurements[30,117]

When an excitation occurs *at* the band edge, the system relaxes non-radiatively via the $2^1A_g^-$ state. The S_2 to S_1 transition occurs via internal conversion between the two potential energy surfaces,[118] taking place on a time-scale of 100s fs.[19,30,117] This suggests that this mid-band excited singlet fission does not proceed via the $2^1A_g^-$ state.

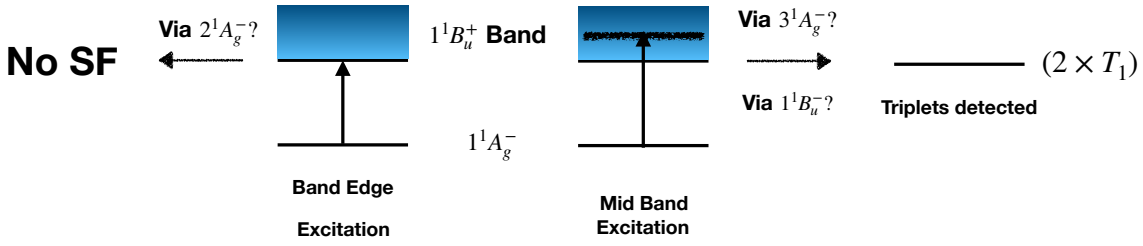


Figure 4.1: Schematic of potential relaxation pathways from the bright state in polyenes

Therefore, in the extended polyene systems there are two relaxation pathways: one to the ground state (which proceeds via the $2^1A_g^-$ state) and a different singlet fission pathway with no $2^1A_g^-$ involvement,[30,117] as illustrated in Fig. 4.1.

If singlet fission in polyenes does not involve the $2^1A_g^-$ state but does require excess energy to overcome a barrier, it can be asked do any higher energy states contribute? Upon vertical excitation it has been found that the $1^1B_u^-$ and $3^1A_g^-$ states exist above the $1^1B_u^+$ state, although as the chain length increases the $1B_u^-$ energy falls below the $1^1B_u^+$.[74,119] It is also thought that the $1^1B_u^-$ and $3^1A_g^-$ states have triplet-triplet character.[74]

In addition to the singlet triplet-pair state, a quintet triplet-pair fission intermediate, $^5(T_1T_1)$ has been observed in acene materials.[22,43,120] Spin mixing, via inter-triplet dipole interactions, is possible between the $^1(T_1T_1)$ and $^5(T_1T_1)$ states,[44] meaning the quintet could be involved in the singlet fission process or offer an alternative relaxation pathway for the excited molecule.

In this chapter calculations of the properties of the key excited states of polyenes, i.e., the $2^1A_g^-$, $1^1B_u^+$, $1^1B_u^-$ and $3^1A_g^-$ singlet states, the $1^5A_g^-$ quintet state and the

$1^3B_u^-$ triplet state are presented.

The Parsier-Parr-Pople-Peierls model was used to describe interacting π-electrons coupled to the nuclei and is solved using the density matrix renormalisation group (DMRG) method. The relaxed geometries of these states are investigated within a soliton framework.

Excitations in polyene systems contain spin-density wave, bond-order excitations and charge density waves. The interplay between these contributions leads to a myriad of phenomena.[58] To gain insight into the nature of the higher energy excited states, the states were characterised using the spin-spin correlation function and triplet-pair and electron-hole projections. In addition, the optical transitions from these key states were investigated.

4.2 Methods

4.2.1 Pariser-Parr-Pople-Peierls model

The Pariser-Parr-Pople-Peierls (PPPP) model was used to treat the π-electrons of the conjugated system. This model includes both long-range electronic interactions and electron-nuclear coupling. It is defined as[58]

$$\hat{H}_{PPPP} = \hat{H}_{PPP} + \hat{H}_{el-ph} + \hat{H}_{elastic}, \tag{4.1}$$

where $\hat{H}_{PPP}$ is the Pariser-Parr-Pople Hamiltonian, defined by

$$\hat{H}_{PPP} = -2t_0 \sum_n \hat{T}_n + U \sum_n \Big(\hat{N}_{n\uparrow} - \frac{1}{2}\Big)\Big(\hat{N}_{n\downarrow} - \frac{1}{2}\Big) + \frac{1}{2} \sum_{n \neq m} V_{n,m} \Big(\hat{N}_n - 1\Big)\Big(\hat{N}_m - 1\Big). \tag{4.2}$$

Here, $\hat{T}_n = \frac{1}{2} \sum_\sigma \left(c^\dagger_{n,\sigma} c_{n+1,\sigma} + c^\dagger_{n+1,\sigma} c_{n,\sigma}\right)$ is the bond order operator, t_0 is the hopping integral for a uniform, undistorted chain, U is the Coulombic interaction of two

electrons in the same orbital and V_{nm} is the long range Coulombic repulsion. The Ohno potential,[121] given by $V_{nm} = U/\sqrt{1 + (U\epsilon_r r_{nm}/14.397)^2}$ is used, with bond lengths r_{nm} in Å. Successful parametrizations of the Ohno potential for conjugated polymers have been found by Mazumdar and Chandross[122] and more recently, by Gebhard and co-workers.[123,124]

H_{el-ph} is the electron-phonon coupling, given by

$$H_{el-ph} = 2\alpha \sum_n (u_{n+1} - u_n)\, \hat{T}_n - 2\alpha W \sum_n (u_{n+1} - u_n) \left(\hat{N}_{n+1} - 1\right) \left(\hat{N}_n - 1\right), \quad (4.3)$$

where α is the electron-nuclear coupling parameter and u_n is the displacement of nucleus n from its undistorted position. Through this term, changes in bond length cause changes in the hopping integrals and the Coulomb interactions. Due to the rapid decay of the density-density correlator, $(N_n - 1)(N_m - 1)$, with distance, only changes in the Coulomb potential to first order are considered.[73,82] Therefore, W is determined by

$$W = \frac{U\gamma r_0}{2\alpha \left(1 + \gamma r_0^2\right)^{3/2}}, \quad (4.4)$$

where $\gamma = (U\epsilon_r/14.397)^2$ and r_0 is the undistorted average bond length in Å.

The elastic energy of the nuclei contributes through H_{ph}, defined as

$$H_{ph} = \frac{\alpha^2}{\pi t_0 \lambda} \sum_n (u_{n+1} - u_n)^2 + \Gamma \sum_n (u_{n+1} - u_n), \quad (4.5)$$

where λ, the dimensionless electron-nuclear coupling parameter, is $\frac{2\alpha^2}{\pi K t}$ and K is the nuclear spring constant. Γ is a Lagrange multiplier which ensures a constant chain length.

The requirement that the force per bond vanishes at equilibrium gives a self-

consistent equation for the bond distortion, namely

$$(u_{n+1} - u_n) = \frac{\pi t \lambda}{\alpha} \left(\Gamma - \left\langle \hat{T}_n \right\rangle + W \left\langle \hat{D}_n \right\rangle \right), \tag{4.6}$$

where $\hat{D}_n = (N_n - 1)(N_{n+1} - 1)$ is the nearest neighbour density-density correlator.

We can calculate relaxed energies of eigenstate using this equation, and the following routine:

1. The eigenstate is calculated using an initial choice of $\{u_n\}$ by building up the target chain length using the DMRG method.

2. At the target chain length, the conditions of force per bond equalling 0 and Eq. (4.6) are applied to find new the $\{u_n\}$.

3. Using the new values $\{u_n\}$, steps (1) and (2) are repeated. The procedure is successfully terminated when the energy of the eigenstate have converged to some tolerance.

DMRG is a highly accurate and robust computational method for gapped, one-dimensional quantum lattice models. Being variational, its accuracy is systematically improvable by increasing the Hilbert space size. Extensive convergence tests on the application of the DMRG method to the excited states of the PPPP model have previously been published.[73,125,126] For the current calculations we typically retained over 400 states per block. In addition, when investigating possible energy crossovers between pairs of excited states, we compute these states using the same reduced density matrix (i.e., in the same truncated Hilbert space).

This work followed a parameterisation of the PPP Hamiltonian by Mazumdar and Chandross for *screened* polyacetylene,[122] namely $U = 8$ eV, $\epsilon_r = 2$ and $t_0 = 2.4$ eV. Furthermore, the electron-nuclear coupling constants of Barford and co-workers,[73] namely, $\lambda = 0.115$ and $\alpha = 4.593$ eVÅ^{-1} were used.

4.3 Results

4.3.1 Vertical and relaxed energies

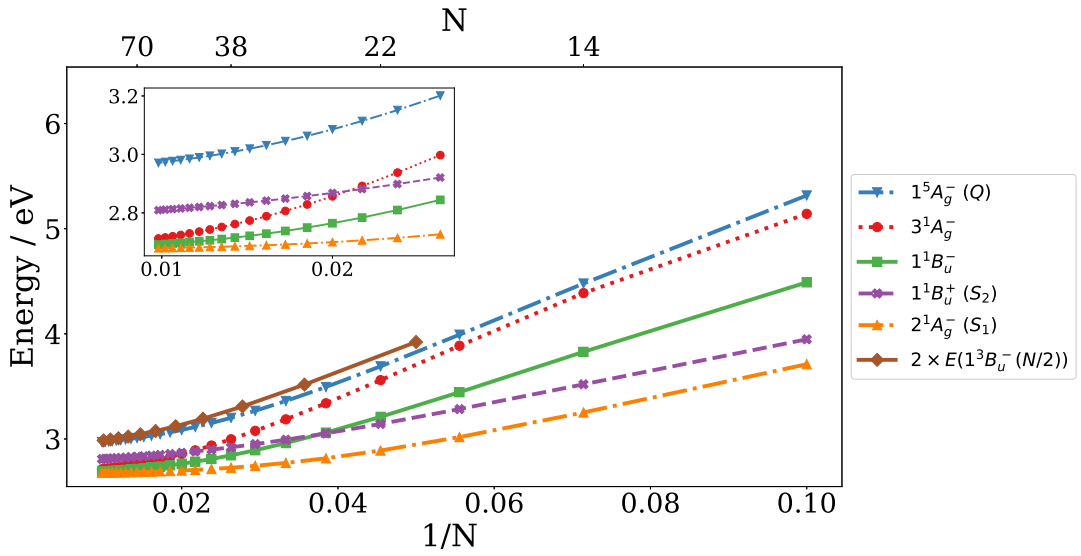


Figure 4.2: Vertical excitation energy of low-lying singlet and quintet states. Also shown is twice the vertical excitation energy of the triplet for chain lengths $N/2$. N is the number of C-atoms. The insert shows the energies in the asymptotic limit.

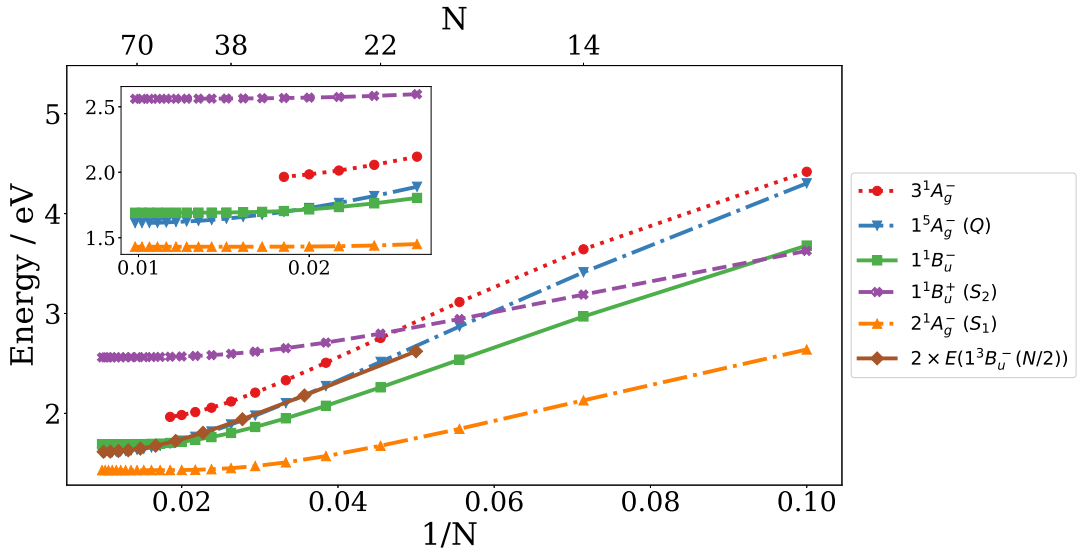


Figure 4.3: Relaxed excitation energy of low-lying singlet and quintet states. Also shown is twice the relaxed excitation energy of the triplet for chain lengths $N/2$. N is the number of C-atoms. The insert shows the energies in the asymptotic limit.

Using the Hellmann-Feynman iterative procedure, the relaxed geometries of the ground state, $1^1A_g^-$, for a range of chain lengths up to 102 carbon atoms (or sites)

were calculated using the DMRG method.[73,86,101]

The vertical excitation energies for the lowest energy singlets are shown in Fig. 4.2. For short chains, the usual energetic ordering of $2^1A_g^- < 1^1B_u^+ < 1^1B_u^- < 3^1A_g^-$ is observed.[74,127] For chain lengths greater than 26 sites, the vertical $1^1B_u^-$ energy becomes lower than the $1^1B_u^+$ energy, while at chain lengths greater than 46 sites the $3^1A_g^-$ vertical energy falls below the $1^1B_u^+$ energy.

The $1^5A_g^-$ quintet state, however, remains above the bright state at all chain lengths. Its energy converges to twice the triplet energy evaluated at half the chain length, implying that it corresponds to an unbound triplet-pair. This assumption will be confirmed by an analysis of the bond-dimerisation and spin-spin correlation in the following sections. (This observation of the triplet-pair character of the quintet state is often invoked for simpler models, but remains valid with interacting electrons and electron-nuclear coupling.[19])

The inset of Fig. 4.2 shows that the vertical energies of the $2^1A_g^-$, $1^1B_u^-$ and $3^1A_g^-$ states converge to the same value in the asymptotic limit, being ~ 0.3 eV lower than the vertical quintet state. This result indicates that these vertical singlet states are different pseudo-momentum members of the same family of excitations, as described in more detail in Section 4.3.4. They have different energies because of their different center-of-mass kinetic energies, which vanishes in the long-chain limit.

Turning now to the relaxed energies, as shown in Fig. 4.3 the relaxed $2^1A_g^-$ state is always lower in energy than the relaxed $1^1B_u^+$ state. For chain lengths greater than 10 and 20 sites, the $1^1B_u^-$ and $3^1A_g^-$ states, respectively, also fall below the $1^1B_u^+$ state. The quintet state undergoes a considerable geometry relaxation compared to the $1^1B_u^+$ state and its energy falls below the bright state for $N > 16$.

Comparing the vertical and relaxed energies, between 10 and 26 sites the vertical

$1^1B_u^-$ state lies above the vertical $1^1B_u^+$ state, but the relaxed $1^1B_u^-$ state is below the relaxed $1^1B_u^+$ state; and similarly for the $3^1A_g^-$ state between 20 and 46 site chains. Thus, the calculations suggest that there might exist internal conversion pathways to these states from the optically excited $1^1B_u^+$ state. In addition, if spin mixing is allowed, relaxation pathways could also involve the $1^5A_g^-$ quintet state. Based on the experimental observations that certain relaxation pathways become available only for mid-band or higher excitation,[19,117] these pathways are likely to have a barrier.

The $2A_g^-$ state is found to be a bound state compared to two free (relaxed) triplets. Whilst endothermic singlet fission is possible,[25,128] this state is unlikely to be involved in singlet fission and instead offers an alternative relaxation pathway, as has been observed experimentally.[30,117] Similarly, for realistic chain lengths the relaxed $1^1B_u^-$ energy lies below the relaxed energy of two free triplets, while the relaxed $3^1A_g^-$ energy lies above them for all chain lengths. Furthermore, the relaxed quintet state was found to be approximately twice the energy of a relaxed triplet for a chain of $N/2$, $E(1^5A_g^-) \approx 2 \times E(1^3B_u^-[N/2])$, similar to the vertical case.

It is worth noting that the relaxation energies increase as $3^1A_g^- < 1^1B_u^- < 2^1A_g^-$. Consequently, unlike the vertical energies, the relaxed energies of the $2^1A_g^-$, $1^1B_u^-$ and $3^1A_g^-$ states do not converge to the same value in the asymptotic limit, and indeed they saturate for $N \gtrsim 50$. This energy saturation occurs because of self-localisation of the solitons, which is a consequence of the classical treatment of the nuclear degrees of freedom and can be corrected by using a model of fully quantised phonons[58,125] (see Chapter 6). In practice, however, in realistic systems disorder will also act to localise excited states.[129]

4.3.2 Soliton structures

In the even N polyene ground state, nuclei are dimerised along the chain, with a repeated short-long-short bond arrangement. Electronically excited states lower their total energy by distorting from the ground state geometry. In some cases, the ground state bond alternation is reduced or reversed over sections of the chain. The change of dimerisation is characterised by domain walls called solitons.[58,73,77,130–132]

In neutral chains with an even number of sites, each soliton (S) is associated with an antisoliton ($\bar{S}$). Solitons in linear conjugated systems are of two types: radical or ionic. For a radical soliton associated with covalent states the nuclei distortion is centred around a radical unpaired spin (or a spinon); the soliton has a net spin but is neutral. For an ionic soliton, however, the distortion is associated with an unoccupied or doubly occupied site, so has $S^z = 0$ but is charged.[58,77]

To investigate the solitonic structure of the excited singlet and quintet states, the staggered, normalised bond dimerisation, δ_n, of their relaxed geometries was calculated, defined as

$$\delta_n = (-1)^n \frac{(t_n - \bar{t})}{\bar{t}}, \tag{4.7}$$

with $t_n = t_0 + \alpha(u_{n+1} - u_n)$ and $\bar{t}$ being the average of t_n.

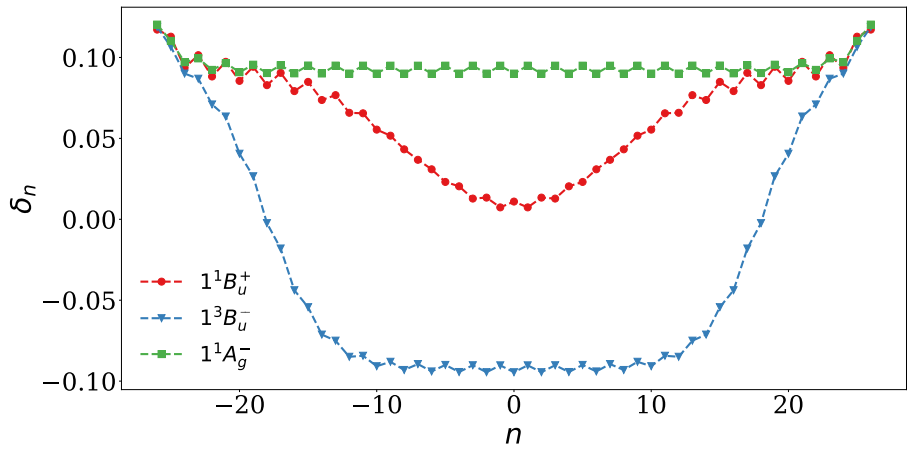


Figure 4.4: Staggered bond dimerisation, δ_n, for the ground state, $1^1A_g^-$, and the two-soliton states, $1^1B_u^+$and $1^3B_u^-$

Fig. 4.4 shows the staggered bond dimerisation for the ground state, $1^1A_g^-$, the first optically singlet excited state, $1^1B_u^+$, and the lowest energy triplet state, $1^3B_u^-$. The $1^1A_g^-$ bond dimerisation is used as a reference, which remains close to $\delta = 0.085$ across the chain, though being slightly larger at the ends of the chain.

As the value of δ_n tends to zero the lattice becomes undimerised, while a negative value indicates dimerisation opposite to the ground state, i.e., short-long-short rather than long-short-long.

An excitation to the $1^1B_u^+$ state creates an electron-hole pair; this state therefore consists of an ionic soliton-antisoliton pair.[133] Due to the Coulomb interaction, this electron hole pair is bound, and the separation of the electron and hole is limited. This means the distortion of the lattice is limited.

The bond dimerisation of the $1^3B_u^-$ state shows a much larger distortion, with a reversal of the ground state dimerisation in the middle of the chain. The $1^3B_u^-$ state consist of two neutral, spin-$\frac{1}{2}$ solitons, owing to the state's covalent character. A schematic of how the ionic and radical solitions that make up the the $1^1B_u^+$ and $1^3B_u^-$ states, respectively, influence the staggered bond dimerisation is provided in Fig. 4.5. Unlike the $1^1B_u^+$ state there is no ionic attraction between the solitons, indeed, the solitons are weakly repelling.

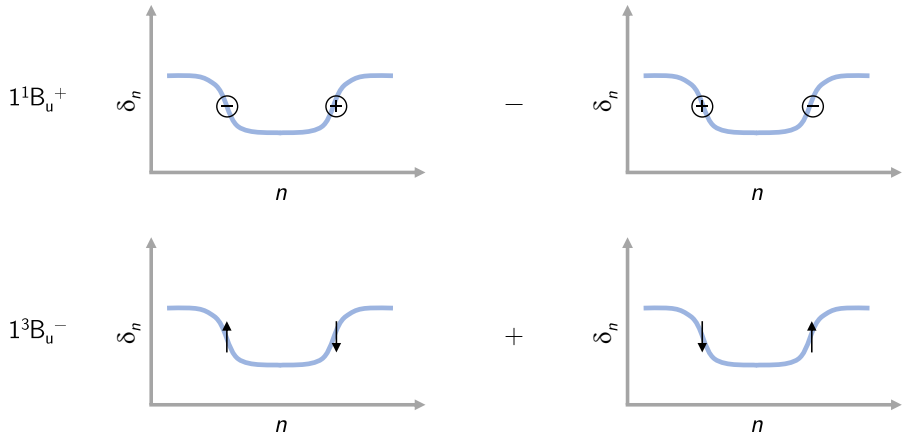


Figure 4.5: A schematic representation of the solitonic structure of the (a) $1^1B_u^+$ state and (b) the $1^3B_u^-$ state.

The bond dimerisation of these two-soliton states can be fitted to the following function

$$\delta_i = \delta_0\Big[1 + \tanh\left(\frac{2n_0 a}{\xi}\right)\Big\{\tanh\left(\frac{2(n-n_0)a}{\xi}\right) - \tanh\left(\frac{2(n+n_0)a}{\xi}\right)\Big\}\Big] \quad (4.8)$$

This equation can be derived from Peierls model,[58,134] but holds with the inclusion of long-range interactions. A soliton is located at $n = n_0$, which changes the phase of dimerisation, and there is an antisoliton located at $n = -n_0$, which reverses the phase again. ξ is the coherence length or domain wall width. The fitted values for the $1^1B_u^+$ and $1^3B_u^-$ are shown in Fig. 4.6.

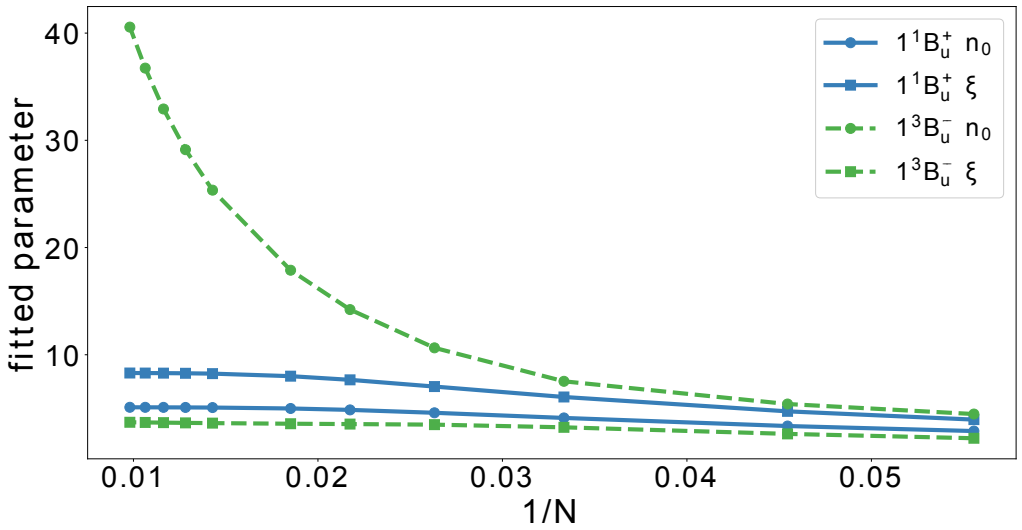


Figure 4.6: Fitted bond dimerisation parameters

For the $1^1B_u^+$ state, the soliton-antisoliton separation, $2n_0$, initially increases, but at longer chain lengths it converges to a value of ≈ 6. This suggest that the soliton-antisoliton form a bound pair.

However for the $1^3B_u^-$ state $2n_0$, is larger and also increases more rapidly. The separation does not converge with chain length, suggesting the $1^3B_u^-$ soliton pair

are weakly repelling. For both states the coherence length, ξ convergences, with the soliton width of the $1^3B_u^-$ being larger than the $1^1B_u^+$ state.

While, the lowest lying triplet state, $1^3B_u^-$, is a two-soliton state (i.e., $S\bar{S}$) with each soliton being associated with a radical spin, residing towards the ends of the chain, the $2^1A_g^-$, $1^1B_u^-$ and $1^5A_g^-$ states are four-soliton states.

Fig. 4.8(a) presents the staggered bond dimerisation for the $2^1A_g^-$ and $1^5A_g^-$ states, implying that the soliton arrangement is $S\bar{S}S\bar{S}$. The $1^5A_g^-$ bond dimerisation strongly resembles that of two triplets residing on either half of the chain, suggesting that the $1^5A_g^-$ state consists of two spatially separated triplets. The edge soliton and antisoliton ($n \approx \mp 18$ to $n \approx \mp 8$), reside much closer to the center of the chain, than for the $1^5A_g^-$ state. The solitons in the center of the chain overlap and as such the chain becomes undimerised, $\delta_n \approx 0$. The bond dimerisation of the $2^1A_g^-$ state is well-known[73,74,130–132,135] the solitons are more bound, indicating that the $2^1A_g^-$ state is a bound triplet-pair. These observations are quantified by fitting the bond dimerisation of the $2^1A_g^-$ and $1^5A_g^-$ states to[132]

$$\delta_n = \delta_0\Bigg[1 + \tanh\left(\frac{2n_0a}{\xi}\right)\Bigg\{\tanh\left(\frac{2(n-n_d-n_0)a}{\xi}\right) - \tanh\left(\frac{2(n-n_d+n_0)a}{\xi}\right) + \tanh\left(\frac{2(n+n_d-n_0)a}{\xi}\right) - \tanh\left(\frac{2(n+n_d+n_0)a}{\xi}\right)\Bigg\}\Bigg], \tag{4.9}$$

where ξ is the domain wall width, $2n_0$ is the separation of the soliton and antisoliton within a $S\bar{S}$ pair on either side of the chain, while $2n_d$ is the separation of the pairs.

The bond dimerisation of the $1^1B_u^-$ state, shown in Fig. 4.8(b), can be explained by the soliton arrangement of $SS\bar{S}\bar{S}$. Its bond dimerisation fits the equation

$$\delta_n = \delta_0\Big[1 + \frac{1}{2}\tanh\left(\frac{2n_0 a}{\xi}\right)\Big\{\tanh\left(\frac{2(n-n_d-n_0)a}{\xi}\right) + \tanh\left(\frac{2(n-n_d+n_0)a}{\xi}\right) - \tanh\left(\frac{2(n+n_d-n_0)a}{\xi}\right) - \tanh\left(\frac{2(n+n_d+n_0)a}{\xi}\right)\Big\}\Big], \tag{4.10}$$

where $2n_0$ is the separation of the soliton and soliton within a SS pair (and likewise of the antisoliton and antisoliton within a $\bar{S}\bar{S}$ pair), while $2n_d$ is the separation of these pairs. The solitonic arrangement, and the definition of n_0 and n_d are illustrated in Fig. 4.7.

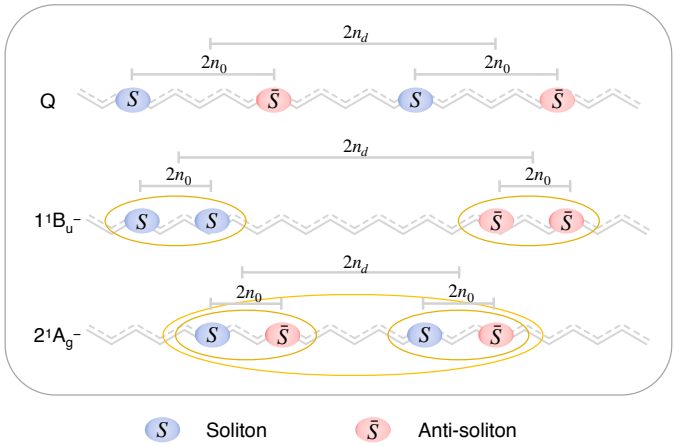


Figure 4.7: The solitonic arrangement of the $1^5A_g^-$ (Q), $1^1B_u^-$, and $2^1A_g^-$ states, and also illustrating the definition of n_0 and n_d. The orange ovals indicate binding between the solitons.

We are unable to fit the $3^1A_g^-$ state bond dimerisation to either Eqs. (4.9) or (4.10). As shown later, there are many different triplet-pair contributions to the $3^1A_g^-$ state causing a complicated bond dimerisation.

The fitted parameters, n_0, n_d and ξ, for the three four-soliton states are plotted in Fig. 4.9 against inverse chain length. In Fig. 4.9(a) the coherence length, ξ, converges with chain length for all states.

The rapid convergence of n_0 with chain length for the $2^1A_g^-$ state, shown in Fig. 4.9(b), implies that the solitons within a $S\bar{S}$ pair are more strongly bound compared

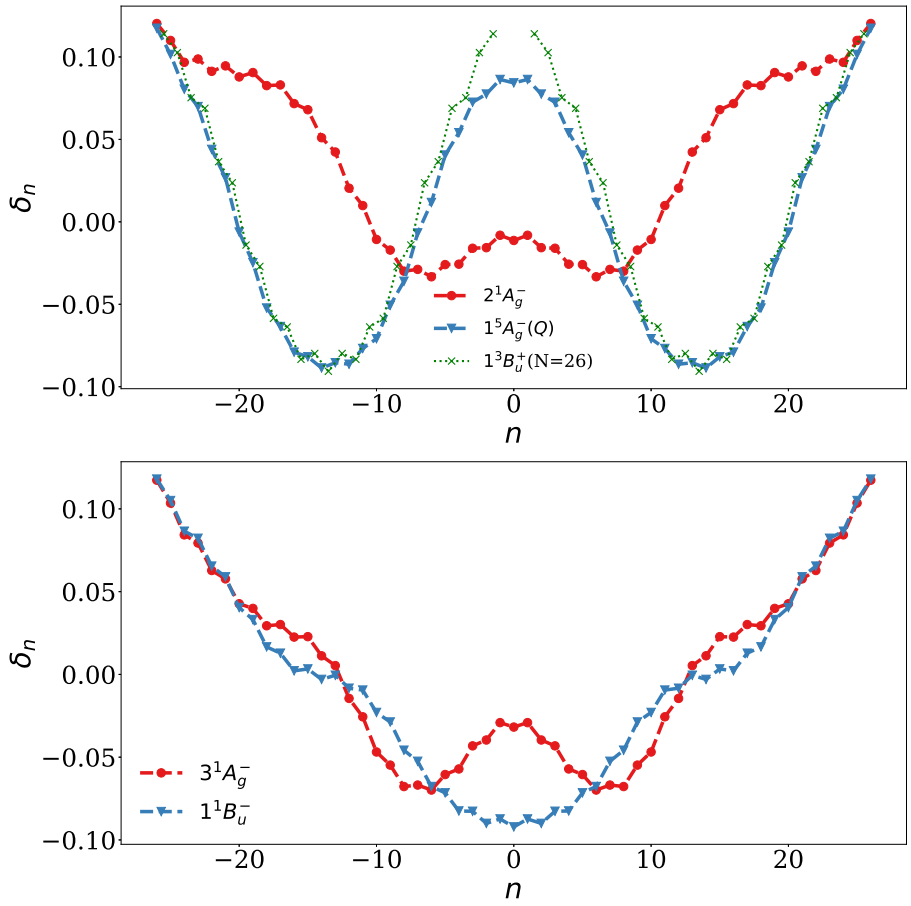


Figure 4.8: The staggered bond dimerisation, δ_n for a chain of 54 sites, of the (a) the $2^1A_g^-$, $1^5A_g^-$ and $1^3B_u^-$ (for $N = 26$) states and (b) the $1^1B_u^-$ and $3^1A_g^-$states.

to other states. For the $1^5A_g^-$ state, the change in n_0 with chain length, N, resembles that of the $1^3B_u^-$ state for a chain of half-length, $N/2$, indicating that the $1^5A_g^-$ state has significant $T_1 - T_1$ character with two triplet-like excitations occupying either side of the chain. n_0 converges as a function of N for the $1^1B_u^-$ state, implying that the solitons (antisolitons) within a SS ($\bar{S}\bar{S}$) pair are bound.

The distances between soliton pairs, n_d, are shown in Fig. 4.9(c). Again, for the $2^1A_g^-$ state there is rapid convergence in the separation of these pairs. In contrast, both the $1^5A_g^-$ and $1^1B_u^-$ states do not show convergence, with the pair separation increasing as the chain length increases. The $S\bar{S}$ pair distance for the $1^5A_g^-$ state follows $n_d \approx N/4$, again indicating that the pairs are unbound.

We also observe that for chains of more than ≈ 50 carbon atoms, n_d increases more quickly for the $1^1B_u^-$ state than for the $1^5A_g^-$state. As shown in the inset of Fig.

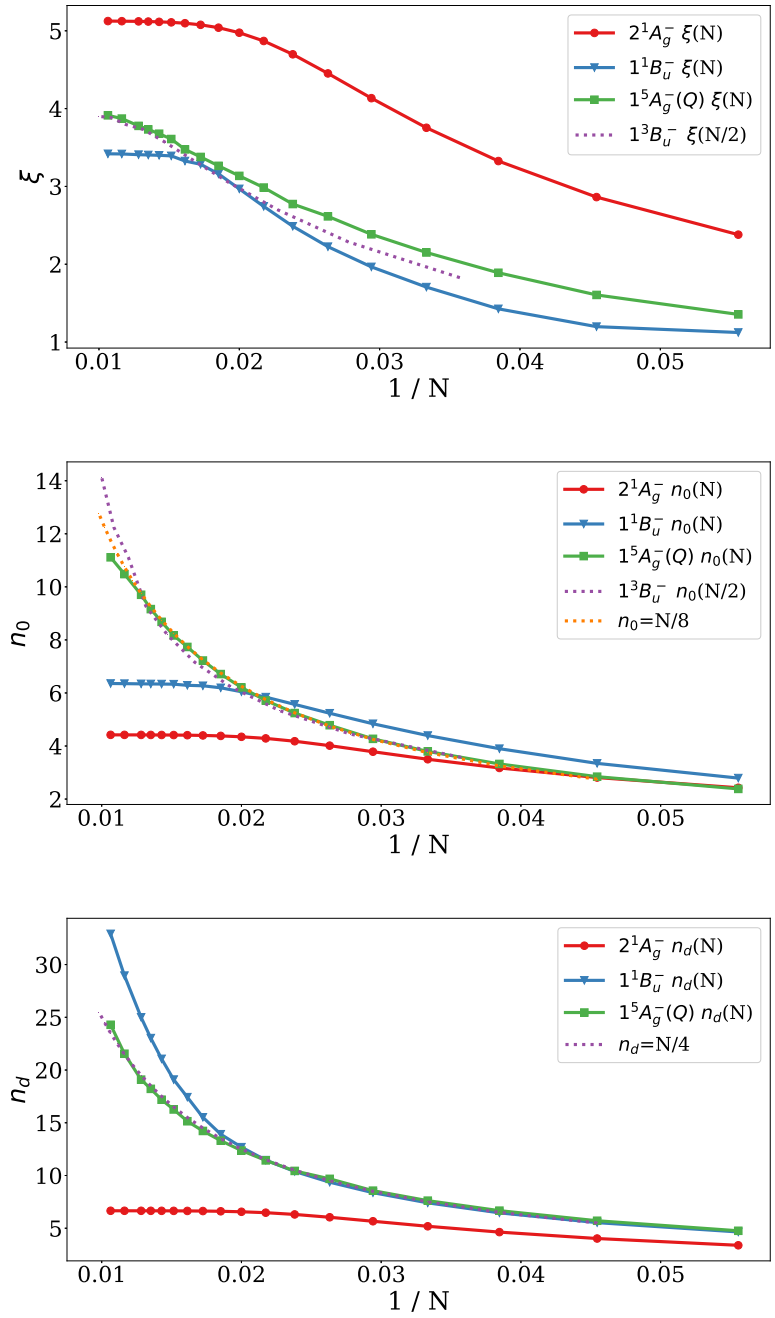


Figure 4.9: The fitted parameters, (a) ξ_i, (b) n_0, and (c) n_d plotted against inverse chain length for the four-soliton states $2^1A_g^-$, $1^5A_g^-$ and $1^1B_u^-$. For comparison, in (a) the $1^3B_u^-$ n_0 for length $N/2$, in (b) the $1^3B_u^-$ ξ for length $N/2$ is plotted and in (c) the curve $n_d = N/4$ is plotted.

4.3, this deviation coincides with the relaxed energy of the $1^1B_u^-$ state being higher than the $1^5A_g^-$ state for $N \geq 50$, implying that at large chain lengths the triplets in the relaxed $1^1B_u^-$ state are unbound with respect to pairs of relaxed triplets. The solitons (or spinons) in the $1^1B_u^-$ state are not *free* however, as n_d converges with

chain length. (We note that the triplets in the relaxed $1^1B_u^-$ state are unbound with respect to pairs of relaxed triplets for all chain lengths because, as we saw in the previous section the electron-lattice relaxation energy decreases with increasing kinetic energy, causing a crossover of the $3^1A_g^-$ and $1^5A_g^-$ energies).

4.3.3 Spin-spin correlation

In addition to the bond dimerisation, further insight into the radical (spinon) character of the triplet-pair states is obtained via the spin-spin correlation function, defined as

$$S_{nm} = \langle S_n^z S_m^z \rangle \,. \tag{4.11}$$

A positive/negative spin-spin correlation value indicates a ferromagnetic/antiferromagnetic alignment between a pair of spins.

The spin-spin correlations for the relaxed $1^3B_u^-$ state are shown in Fig. 4.10a. The radical soliton/antisoliton of the triplet state localise towards the end of the chain and there is a long range spin-spin correlation between them. The solitons are delocalised over a small region well described by the coherence length, ξ.

Fig. 4.10e shows the spin-spin correlation for the relaxed $1^5A_g^-$ state; there are three correlations between neighbouring solitons and antisolitons, and three further long range correlations. This correlation pattern is consistent with two unbound triplets, i.e., four solitons positioned along the chain as predicted from Eq. (4.9) and presented in Fig. 4.8a. A schematic of the soliton interactions that lead to these six correlations is shown in Fig. 4.10f.

Fig. 4.10b shows S_{nm} for the $2^1A_g^-$ state. It is difficult to discern correlations between individual solitons, because the correlations overlap each other. However, along the anti-diagonal, $m = (N - n)$, long range correlations between sites ≈ 10 and ≈ 40 can be seen. Overall, the spin-spin correlations of the $2^1A_g^-$ state further

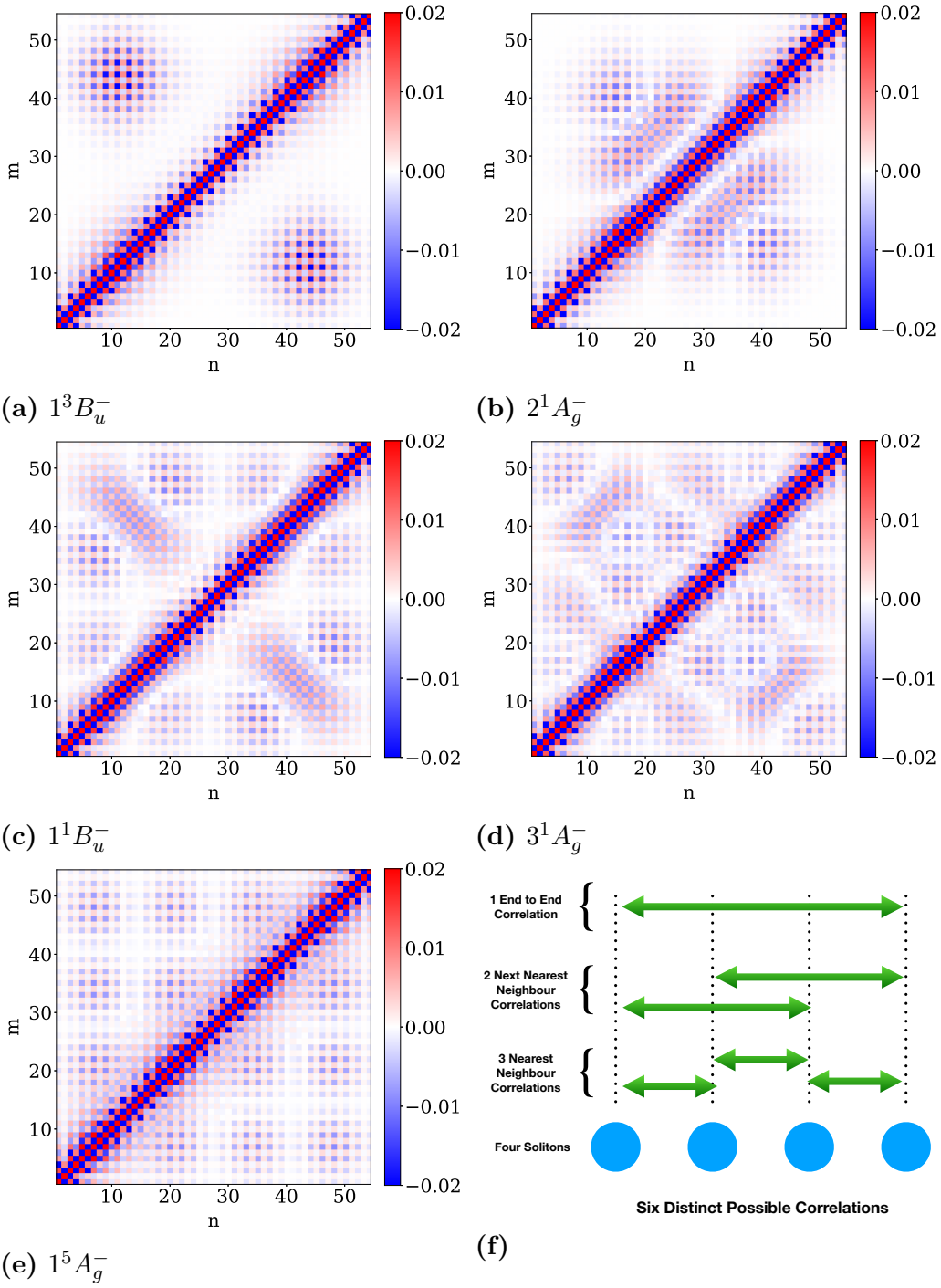


Figure 4.10: The spin-spin correlations for the relaxed (a) $1^3B_u^-$, (b) $2^1A_g^-$, (c) $1^1B_u^-$, (d) $3^1A_g^-$, and (e) $1^5A_g^-$ states. (f) shows a schematic of the correlations from the four spin-radicals (solitons) of the $1^5A_g^-$ state. (Note that the values of S_{nm} for $n = m$ to $n = m \pm 4$ are larger than scale provided. The scale presented is used to emphasise the long range correlations.)

confirm its bound triplet-pair character. The triplets are bound in the middle of the chain, and individual solitons contributing to the triplets cannot be identified.

S_{nm} for the relaxed $1^1B_u^-$ state shows correlations similar to $3^1A_g^-$ state, but

with much more delocalised correlations along the antidiagonal.

4.3.4 Excited state wavefunctions

The low-lying singlet dark states, i.e., $2^1A_g^-$, $1^1B_u^-$ and $3^1A_g^-$, have negative particle-hole symmetry and are sometimes characterised as being covalent or of predominately spin-density-wave (SDW) character. In contrast, the optically allowed $1^1B_u^+$ state has positive particle-hole symmetry and is characterised as being 'ionic' or of electron-hole character.

In practice, however, the multiexcitonic $2^1A_g^-$, $1^1B_u^-$ and $3^1A_g^-$ states have both covalent and ionic character. In addition, as found in Section 4.3.1, the vertical energies of these states converge to the same value as $N \to \infty$ suggesting that they are related. In this section we describe the multiexcitonic character of these states and explain how they are members of the same family of excitations. We first discuss the triplet-pair components of these states before describing their excitonic wave functions.

Triplet-triplet overlap

By comparing the excitation energy of the low-energy singlets of polyenes with the excitation energy of the individual triplets, it has been suggested that the triplet-triplet combinations that contribute to each state are:[74,118]

$$\begin{aligned} 2^1A_g^- &\equiv T_1 \otimes T_1 \\ 1^1B_u^- &\equiv T_1 \otimes T_2 \\ 3^1A_g^- &\equiv T_2 \otimes T_2 \end{aligned} \tag{4.12}$$

where $T_1 \equiv 1^3B_u^-$ and $T_2 \equiv 1^3A_g^-$.

To quantify the triplet-triplet character of the $2^1A_g^-$, $3^1A_g^-$ and $1^1B_u^-$ singlet

states their overlap with triplet-pair direct product wavefunctions was computed. Firstly the vertical excited state wavefunctions for a chain of 12 sites were calculated and then, by calculating the triplet states for a chain of 6 sites and taking the direct product of different pairs of triplets, states that have triplets on either half of the chain are generated. The square overlap of the triplet-triplet wavefunctions with the $2^1A_g^-$, $3^1A_g^-$ and $1^1B_u^-$ states are presented in Tab. 4.1.

The $2^1A_g^-$ state, whilst primarily consisting of $T_1 \otimes T_1$ components, also contains some $T_1 \otimes T_2$ character. The $1^1B_u^-$ state consists exclusively of $T_1 \otimes T_2$, as only these combinations are symmetry allowed. The $3^1A_g^-$ state, rather than primarily having $T_2 \otimes T_2$ character, has both $T_1 \otimes T_1$ and symmetry allowed combinations of T_1 and T_2 components in its wavefunction. Indeed, the sum of the $T_1 \otimes T_1$ and $T_1 \otimes T_2$ components has larger amplitude than the $T_2 \otimes T_2$ character. Since the $3^1A_g^-$ state has character from each of the triplet-triplet combinations, the sum of these contributions lead to the complicated staggered bond dimerisation and spin-spin correlation, discussed in Sections 4.3.2 and 4.3.3.

Triplet-pair wavefunctions

In the previous section it was found that higher-energy covalent states are composed of linear combinations of higher-energy triplet states. This section investigates how to construct bound triplet-pair states from free triplet-pair states. To do this it is convenient to assume translationally invariant systems. In addition a dimerised antiferromagnetic groundstate is also assumed, from which bound triplet-pair excitations are predicted.[136,137]

Suppose that $a_{k_1}^\dagger$ and $a_{k_2}^\dagger$ create triplet excitations (or more precisely, bound spinon-antispinon pairs[137]) with wavevectors k_1 and k_2. Then a free triplet-pair

		$\lvert \langle T_l \otimes T_r \rvert \Psi \rangle \rvert_v^2$		
T_l	T_r	$2^1A_g^-$	$3^1A_g^-$	$1^1B_u^-$
T_1^0	T_1^0	0.134	0.020	-
T_1^{+1}	T_1^{-1}	0.134	0.020	-
T_1^{-1}	T_1^{+1}	0.134	0.020	-
T_1^0	T_2^0	0.010	0.012	0.022
T_2^0	T_1^0	0.010	0.012	0.022
T_1^{+1}	T_2^{-1}	0.010	0.012	0.022
T_2^{-1}	T_1^{+1}	0.010	0.012	0.022
T_2^{+1}	T_1^{-1}	0.010	0.012	0.022
T_1^{-1}	T_2^{+1}	0.010	0.012	0.022
T_2^0	T_2^0	-	0.015	-
T_2^{+1}	T_2^{-1}	-	0.015	-
T_2^{-1}	T_2^{+1}	-	0.015	-
Total		0.462	0.177	0.132

Table 4.1: Table of the square of overlaps, $\lvert \langle T_l \otimes T_r \rvert \Psi \rangle \rvert^2$ for the vertical $2^1A_g^-$, $1^1B_u^-$ and $3^1A_g^-$ states. T_r and T_l are calculated for a 6 site chain (the super script indicates the S_z eigenvalue of the state, T_1 and T_2 corresponds to the $1^3B_u^-$ and $1^3A_g^-$ triplets, respectively), while the state Ψ is calculated for an 12 site chain.

excitation is

$$|k_1, k_2\rangle = |K - k'/2, K + k'/2\rangle = a^\dagger_{k_1} a^\dagger_{k_2} |\mathrm{GS}\rangle \,, \tag{4.13}$$

where $2K = (k_1 + k_2)$ is a the center-of-mass wavevector, $k' = (k_1 - k_2)$ is the relative wavevector, and $|\mathrm{GS}\rangle$ represents the dimerised antiferromagnetic groundstate.

A bound triplet-pair excitation is a linear combination of the kets $\{|k_1, k_2\rangle\}$, namely

$$|\Phi_n(K)\rangle = \sum_{k',K'} \Phi_n(k', K') \, |K - k'/2, K + k'/2\rangle \,, \tag{4.14}$$

where $\Phi_n(k', K')$ is the triplet-pair wavefunction in k-space and n is the principal quantum number. K is a good quantum number for the bound state (although k' is not), hence

$$\Phi_n(k', K') = \psi_n(k')\delta(K' - K) \tag{4.15}$$

and thus

$$|\Phi_n(K)\rangle = \sum_{k'} \psi_n(k') \, |K - k'/2, K + k'/2\rangle \,. \tag{4.16}$$

Fourier transforming $\Phi_n(k', K')$ gives the real-space triplet-pair wavefunction:

$$\tilde{\Phi}_{n,K}(r, R) = \tilde{\psi}_n(r)\tilde{\Psi}_K(R) \tag{4.17}$$

where the center-of-mass wavefunction is the Bloch state

$$\tilde{\Psi}_K(R) = \frac{1}{\sqrt{N}} \exp(iKR). \tag{4.18}$$

R is the center-of-mass coordinate, and $\tilde{\psi}_n(r)$ is the relative wavefunction with r being the $T - T$ separation.

Equation (4.16) indicates that the bound triplet-pair state is constructed from a linear combination of free triplet-pair states with different k_1 and k_2, subject to

a definite center-of-mass wavevector (and momentum). These states form a band, whose band width is determined by their center-of-mass kinetic energy. A bound triplet-pair is unstable to dissociation (or fission) if its kinetic energy is greater than the triplet-pair binding energy.

4.3.5 Exciton wavefunctions

We now describe the exciton wave functions of the low- energy states of linear polyenes, using a real-space representation. The excitation of an electron from the valence-band to the conduction-band in semiconductors creates a positively charged hole in the valence-band. In conjugated polymers, the electrostatic interaction between the two create a bound electron-hole pair, termed an exciton. Assuming the 'weak-coupling' limit, excitons in conjugated polymers are described by an effective H-atom model[58,126,138] or by a mapping from a single-CI calculation.[139] An excitation from the valence-band to the conduction-band can thus be characterised by an effective particle model.[58] In the real-space picture, an exciton is described by the center-of-mass coordinate of the exciton, R and the relative coordinate, r.[58] r is a measure of the size of the exciton. The electron-hole coordinate, r, is associated with the principal quantum number, n[58,126,138] , while the center-of-mass coordinate is associated with the center-of-mass quantum number, j.

We denote an exciton basis state by $|R + r/2, R - r/2\rangle$. The exciton creation operator $S^{\dagger}_{rR}$ creates a hole in the valence-band orbitals at $(R - r/2)$ and an electron in the conduction-band orbitals at $(R + r/2)$, i.e.,

$$|R + r/2, R - r/2\rangle = S^{\dagger}_{rR}\,|\mathrm{GS}\rangle\,, \tag{4.19}$$

where $|\mathrm{GS}\rangle$ is the ground state in this basis.

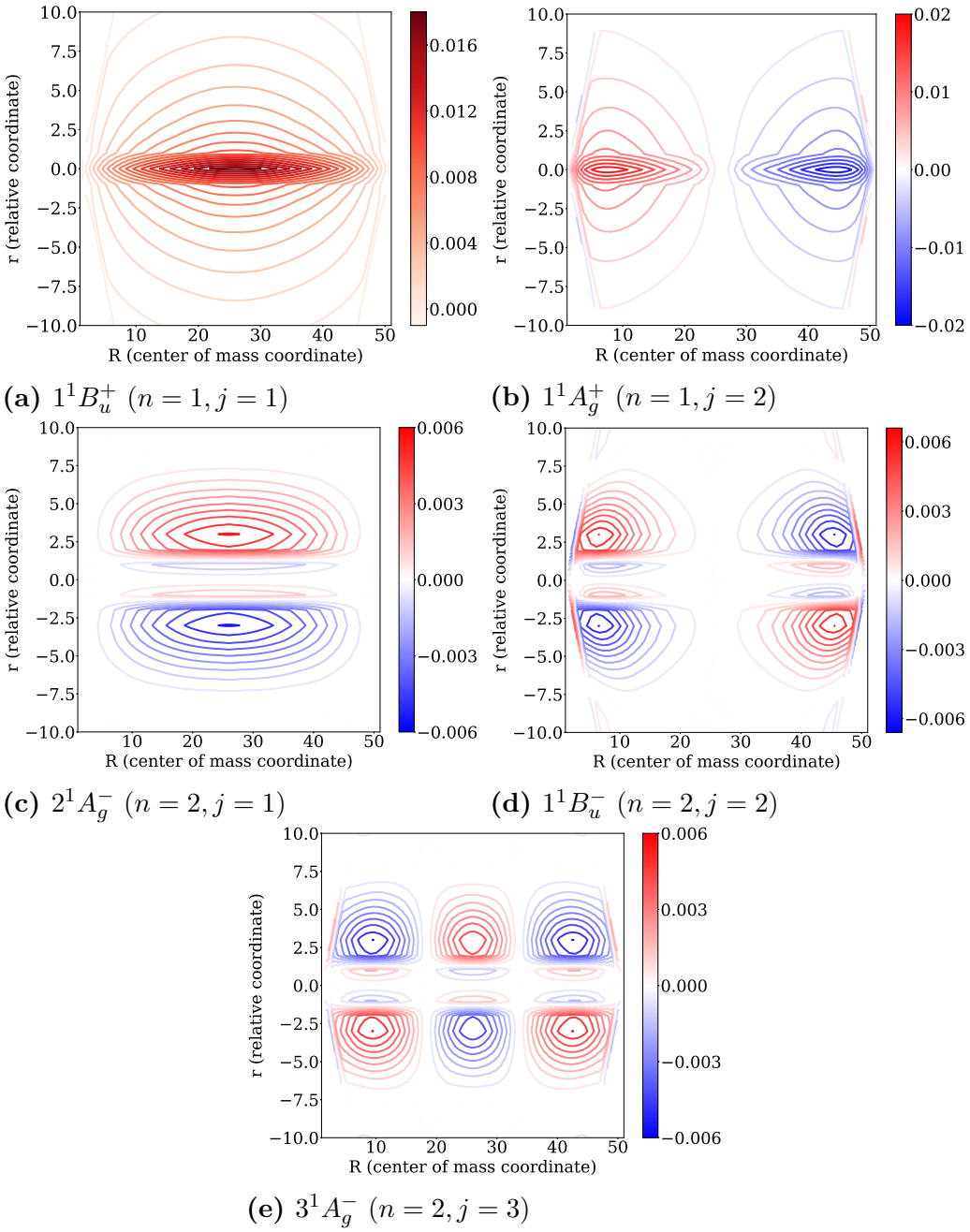
To investigate the electron-hole nature of the excited states, we express an excited state $|\Phi\rangle$ as a linear combination of the real-space exciton basis $\{|R + r/2, R - r/2\}\rangle$:

$$|\Phi\rangle = \sum_{r,R} \Phi(r, R) \, |R + r/2, R - r/2\rangle \, . \tag{4.20}$$

$\Phi(r, R)$ is the exciton wavefunction and is given by the projection of the excited states on to the ground state:

$$\Phi(r, R) = \langle \mathrm{GS}|S_{rR}|\Phi\rangle \, . \tag{4.21}$$

The calculated vertical exciton wavefunctions for the $1^1B_u^+$, $1^1A_g^+$, $2^1A_g^-$, $1^1B_u^-$ and $3^1A_g^-$ states of chain of $L = 102$ are illustrated in Fig. 4.11. A similar method has been employed by Rissler and co-workers[140] for visualising exciton wavefunctions of Peierls–Mott insulators.



(a) $1^1B_u^+$ $(n = 1, j = 1)$

(b) $1^1A_g^+$ $(n = 1, j = 2)$

(c) $2^1A_g^-$ $(n = 2, j = 1)$

(d) $1^1B_u^-$ $(n = 2, j = 2)$

(e) $3^1A_g^-$ $(n = 2, j = 3)$

Figure 4.11: Exciton components obtained from Eq. (4.21). n and j are the exciton principal and center-of-mass quantum numbers, respectively. Reproduced from D. J. Valentine, D. Manawadu, and W. Barford; Higher-energy triplet-pair states in polyenes and their role in intramolecular singlet fission, *Phys. Rev. B*, **102(12)**, 125107 (2020)

The nodal patterns of $\Phi(r, R)$ indicate that the $1^1B_u^+$ and $1^1A_g^+$ states have components belonging to the $n = 1$ family of (even-parity) excitons with center-of-mass quantum numbers, $j = 1$ and 2, respectively. Similarly, the $2^1A_g^-$, $1^1B_u^-$ and $3^1A_g^-$ states have components belonging to the $n = 2$ family of (odd-parity) excitons with center-of-mass quantum numbers, $j = 1$, 2 and 3, respectively. Thus, the single

electron-hole components of the $2^1A_g^-$, $3^1A_g^-$ and $1^1B_u^-$ states belong to the same fundamental excitation. We note, however, that the electron-hole weights for these states are five times smaller than for the $1^1B_u^+$ and $1^1A_g^+$ states.

(The calculation of the exciton components of the triplet-pair state was carried out by Barford group member Dilhan Manawadu. The above analysis was a joint collaboration.)

4.3.6 The '$2A_g$ family'

As we have shown, the $2^1A_g^-$, $1^1B_u^-$ and $3^1A_g^-$ states have both triplet-pair and electron-hole components. For a translationally invariant system their vertical excitations can be expressed as

$$|\Phi(K)\rangle = a^{\mathrm{TT}}(K)\left|\Phi_m^{\mathrm{TT}}(K)\right\rangle + a^{\text{e-h}}(K)\left|\Phi_n^{\text{e-h}}(K)\right\rangle, \tag{4.22}$$

where $\left|\Phi_m^{\mathrm{TT}}(K)\right\rangle$ is given by Eq. (4.16) and $\left|\Phi_m^{\text{e-h}}(K)\right\rangle$ is given by Eq. (4.20).[58] Both components are labelled by the same center-of-mass quantum number, K, but the principal quantum numbers for the triplet-pair (m) and electron-hole (n) components are different, being 1 and 2, respectively.

Equation (4.22) conveys the concept that the $2^1A_g^-$, $1^1B_u^-$ and $3^1A_g^-$ states are the three lowest-energy members of the same set of fundamental excitations which are distinguishable only by their center-of-mass momentum.

4.3.7 Spectra

As the low-energy states have triplet-triplet components, it might be expected that their spectra resemble that of the $1^3B_u^-$ and $1^3A_g^-$ triplet states. The approximate spectra of the $2^1A_g^-$, $3^1A_g^-$, $1^1B_u^-$, $1^5A_g^-$, $1^3B_u^-(T_1)$ and $1^3A_g^-(T_2)$ states for a $N = 26$

were calculated using the expression,

$$I(E) = \sum_i |\langle i \,|\, \hat{\mu} \,|\, \Psi \rangle|^2 \delta(E_i - E_\Psi - E), \tag{4.23}$$

where the sum is over states with opposite particle-hole and C_2 symmetry to the state $|\Psi\rangle$. $(E_i - E_\Psi)$ is the energy difference between state i and state Ψ, $\hat{\mu}$ is the transition dipole operator and $|\langle i \,|\, \hat{\mu} \,|\, \Psi \rangle|^2$ is square of the transition dipole moment between states i and Ψ.

As shown in Figs. 4.12-4.13, for all of the triplet-pair states, the maximum absorption occurs within ~ 0.5 eV of the $1^3B_u^-$ maximum absorption. Given that the $2^1A_g^-$ state is considered to be a bound triplet-pair, it might be expected that the maximum absorption energy is higher than the triplet state, as a photoexcitation would need to overcome the binding energy of the triplet, in addition to having enough energy to excite a triplet state. However, the maximum absorption of the $2^1A_g^-$ state is found to be lower than the $1^3B_u^-$ state, in agreement with experimental observations in carotenoids.[141] The $2^1A_g^-$ state also has an absorption in the near infra-red part of the spectrum, which can be attributed to the $2^1A_g^- \rightarrow 1^1B_u^+$ transition. The near infra-red absorption of a bound triplet-pair has also been predicted in acene materials.[56]

The $1^5A_g^-$ quintet state exhibits a single absorption with energy closest to the triplet maximum absorption over all chain lengths and whose intensity most closely matches the $1^3B_u^-$ absorption. Comparing the $1^1B_u^-$ to the triplets, for each triplet absorption there is a corresponding red-shifted absorption in the $1^1B_u^-$ spectra, also indicating that despite being a bound state, absorption are lower in energy compared to individual triplets.

Due to the mixed triplet-pair character of the $3^1A_g^-$ state there are many different absorptions. As for the $2^1A_g^-$state, the $3^1A_g^-$ state has a lower energy absorption in

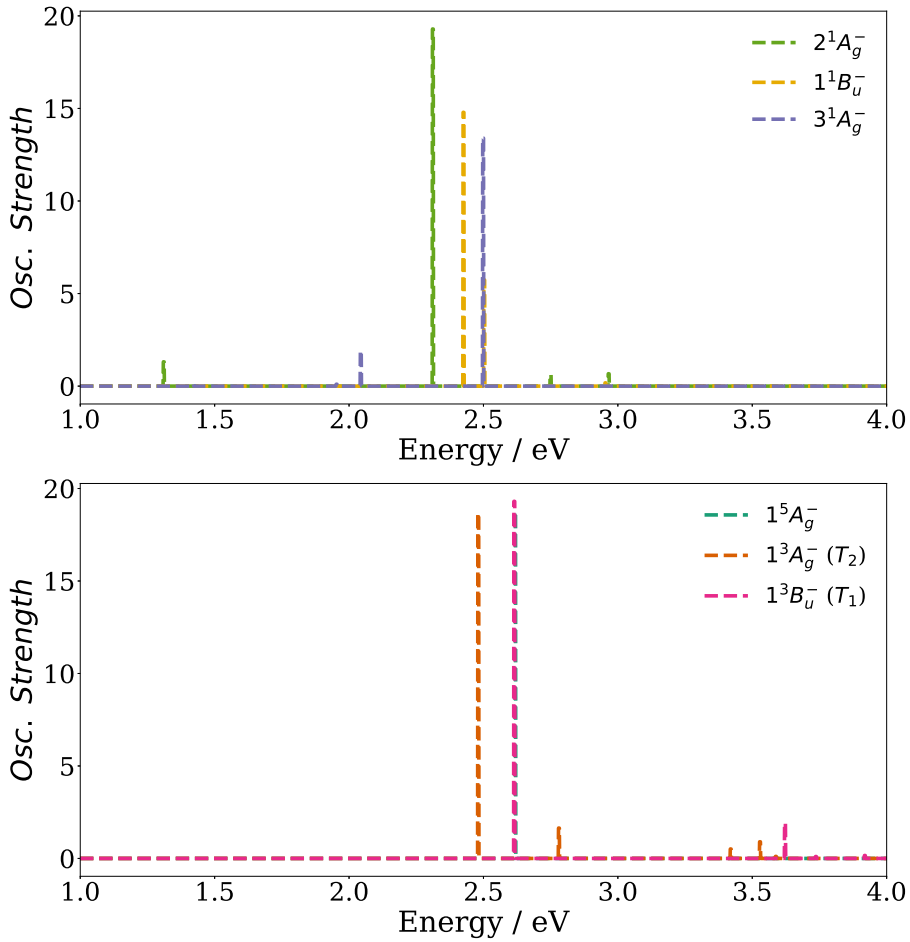


Figure 4.12: Stick spectra calculated using Eq. (4.23) of the (a) $2^1A_g^-$, $3^1A_g^-$and $1^1B_u^-$ states and (b) $1^5A_g^-$, $1^3B_u^-(T_1)$ and $1^3A_g^-$ (T_2) for 26 site chain

the infra-red to yellow portion of the spectrum.

It is worth noting that although our calculated transition energy from the $1^5A_g^-$ state coincides with our calculated $T-T^*$ transition energy (i.e., ca. 2.56 eV for the 26-site chain) this energy is over 1 eV higher than the observed $T-T^*$ transition energy for singlet fission in conjugated polyenes.[19,30] This discrepancy is in large part due to the failure of the Mazumdar and Chandross parameterisation of the PPP model to correctly estimate the solvation energy of weakly bound excitons and charges.[122] The T^* state is expected to be the $n=2$ (charge-transfer) triplet exciton, whose solvation energy is over an eV larger than predicted by the parametrised PPP model.[142]

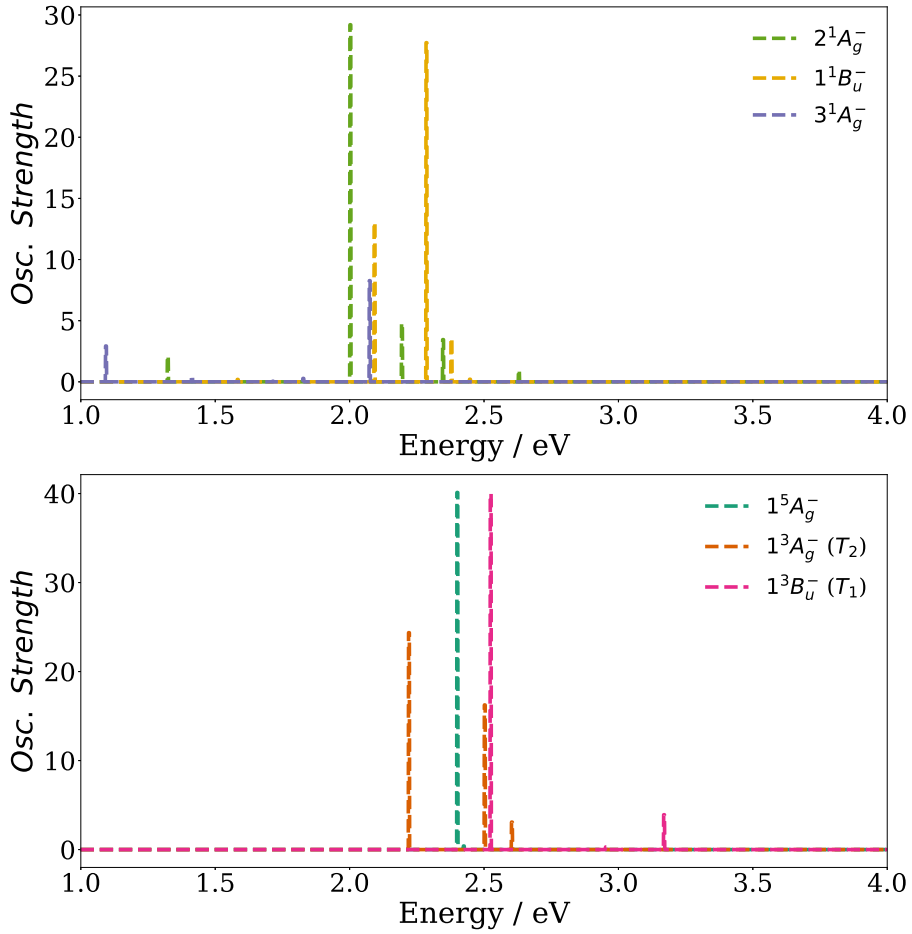


Figure 4.13: Stick spectra calculated using Eq. (4.23) of the (a) $2^1A_g^-$, $3^1A_g^-$and $1^1B_u^-$ states and (b) $1^5A_g^-$, $1^3B_u^-(T_1)$ and $1^3A_g^-$ (T_2) for 54 site chain

4.4 Discussion and conclusions

By calculating the relaxed energies of the singlet states of conjugated polyenes, the $1^1B_u^-$ and $3^1A_g^-$ states were found to lie below the bright $1^1B_u^+$ state at experimentally relevant chain lengths. This implies that these states could be involved in relaxation pathways, particularly if systems are excited with energy higher than the band edge. In addition, the energy of the relaxed $1^5A_g^-$ state on a chain of N C-atoms is twice the energy of the relaxed triplet state on a chain of $N/2$ C-atoms, so if spin mixing where allowed this state could represent an intermediate unbound triplet-pair state for the singlet fission process.

An analysis of the bond dimerisation of the relaxed excitations indicates that the $2^1A_g^-$ is a four-soliton state, as previously ascertained.[131] The $1^5A_g^-$ and $1^1B_u^-$ states are also found to be four-soliton states. Both of these states seem to consist of repelling soliton pairs, with the bond dimerisation of the $1^5A_g^-$ resembling two $1^3B_u^-$ triplets occupying either side of the chain. The $3^1A_g^-$ state bond dimerisation is more complicated due to the mixed triplet-pair combinations that contribute to this state.

The spin-spin correlation function offers another way to visualise the soliton structure. This again indicates that the $2^1A_g^-$ state is a bound triplet-pair. $3^1A_g^-$, $1^5A_g^-$ and $1^1B_u^-$ states show long-range spin correlations, which correspond to the staggered bond dimerisation.

The calculated spectra indicate that the $1^5A_g^-$ state most closely resembles the triplet absorption, although the $1^1B_u^-$ and $3^1A_g^-$ states also absorb at a similar energy. Recent pump-push-probe experiments by Pandya et al. excited the $2^1A_g^-$ state after being generated from the relaxation of the initially photoexcited state.[143] As the $2^1A_g^-$ state has $^1(T_1T_1)$ character, the excited push state is expected to be of

$^1(T_1T^*)$ character. Relaxation from the $^1(T_1T^*)$ state was found to involve a state with spatially separated, but correlated triplet; this spatially separated state could be either the $1^1B_u^-$ or $3^1A_g^-$ state.[143]

The triplet-triplet nature of the $2^1A_g^-$, $3^1A_g^-$ and $1^1B_u^-$ states was further probed by calculating the overlap of these states with half-chain triplet combinations. The $T_1 \otimes T_1$ nature of the $2^1A_g^-$ and $T_1 \otimes T_2$ nature of the $1^1B_u^-$ state was confirmed. The $3^1A_g^-$ state has a mixture of $T_1 \otimes T_1$, and symmetry allowed $T_1 \otimes T_2$ and $T_2 \otimes T_2$ contributions.

One of the aims of this work has been to identify a singlet state in polyenes that is intermediate between the initially photoexcited singlet state, S_2, and the final non-geminate pair of triplet states. Such a state should satisfy the following conditions:

1. It should have significant triplet-triplet character.

2. Its vertical energy should lie above the vertical energy of S_2, but its relaxed energy should lie below the relaxed energy of S_2. Such conditions imply the possibility of an efficient interconversion from S_2 via a conical intersection.

3. Its relaxed energy should lie slightly higher than twice the relaxed energy of the triplet state, so that fission is fast and exothermic.

For our choice of model parameters it was found that: the $2^1A_g^-$ state only satisfies condition (1.); the $1^1B_u^-$ state satisfies condition (1.), condition (2.) for $10 < N < 26$, but not condition (3.); the $3^1A_g^-$ state satisfies condition (1.), conditions (2.) for $20 < N < 46$, and condition (3.). Thus, the $3^1A_g^-$ state would appear to be a candidate intermediate state for longer polyenes, but such a state does not exist for shorter carotenoids.

However, caution should be exercised when making predictions about the pre-

cise intermediate state, as owing to using semi-empirical parameters our calculated excitation energies are only expected to be accurate to within a few tenths of an eV. Our key conclusion, therefore, is that there is a family of singlet excitations (the '$2^1A_g^-$ family'), composed of both triplet-pair and electron-hole character, which are fundamentally the same excitation (i.e., have the same principal quantum numbers), but have different center-of-mass energies. The lowest energy member of this family, the $2^1A_g^-$ state, cannot undergo singlet fission. But higher energy members, owing to their increased kinetic energy and reduced electron-lattice relaxation, can undergo singlet fission for certain chain lengths.

Chapter 5

State interconversion: Ehrenfest dynamics

5.1 Introduction

Having discussed the low energy states involved in intramolecular singlet fission in extended polyene systems such as polydiacetylene, attention is now turned to the shorter polyene systems of carotenoids. These molecules are ubiquitous in photosynthetic systems and also undergo singlet fission.

In this chapter, the first step of singlet fission in carotenoid-like systems, state interconversion, is studied. First, a brief historical review of the understanding of SF in carotenoids in presented. Then the methods to probe the state interconversion are introduced. Finally, the results are presented, revealing which states are involved in SF in the first few femtoseconds after photoexcitation.

5.1.1 Singlet fission in carotenoids

Early work on singlet fission in shorter polyene systems was primarily concerned with carotenoids found in bacterial light-harvesting complexes.[15,67] In these complexes, carotenoids act as ancillary light harvesters, absorbing light and funnelling it to photosynthetic centres via excitation energy transfer. They also photoprotect bacteriochlorophylls by quenching chlorophyll triplet excitations.[144] Therefore, in

bacteria, there are two routes to carotenoid triplet formation: triplet sensitisation from the quenching of chlorophyll excitations and singlet fission. SF was first suggested as a mechanism for higher triplet yields in photosynthetic bacteria in the 1980s.[15,67] Later the singlet fission mechanism was found to be an ultrafast process being detected on sub-ps timescales.[145]

In light-harvesting complexes from different bacteria, carotenoids exhibit different geometries.[65] Papagiannakis and co-workers used resonance Raman measurements to show that when carotenoids occupy a twisted geometry, triplet yields are higher. It is thought that the twisted geometry aids the decoherence of the triplets in a triplet pair state formed via singlet fission. This work suggested that singlet fission in carotenoid is intramolecular.[65,145] For intramolecular singlet fission, a single polyene chain must contain two excitations. In contrast with the longer conjugated polymer systems considered in the previous chapter, the two excitations in a carotenoid chain overlap, as the spatial extent of the excitations is greater than the chain length.

The notion of intramolecular singlet fission in carotenoids has been controversial, as SF is an ultrafast process, and it can be challenging to interpret experimental signals.[27,59,68,146] Moreover, intramolecular singlet fission in carotenoids has been questioned by electron paramagnetic resonance studies of carotenoids in the bacterial complexes.[64,66] Klenina and co-workers suggested that singlet fission takes place between two neighbouring carotenoids and could be mediated by nearby bacteriochlorophyll. Studies on carotenoids in solution also could not detect intramolecular singlet fission.[59] At low concentrations, when only an intramolecular mechanism would be possible, no triplets were identified. At higher concentrations, carotenoids aggregates form and intermolecular singlet fission is readily observed.[59,63]

Yu et al. devised a strategy to investigate the triplet formation solely from

the singlet fission channel in bacteriochlorophylls, using triplet excitation profiles.[13] In their work, they investigated how conjugation length can affect singlet fission by studying carotenoids in different bacterial photosynthetic centres. They concluded that carotenoid singlet fission in bacteriochlorophylls is intramolecular and that twisted geometry facilitates singlet fission. Furthermore, they also found that longer conjugation length increases SF triplet yields. They suggest that longer chains aid the localisation of triplets on either end of the chains. Yu and co-workers showed that the EPR results found by the Klenina group are also consistent with an intramolecular scheme.[13,64,66]

To investigate the role twisted geometry can play in intramolecular singlet fission, our colleagues (Clark group, Sheffield) have studied orange carotenoid protein (OCP). OCP binds a single keto-carotenoid, and when exposed to blue-green light, the protein transitions from an orange form (OCPo) to a red form (OCPr).[147,148] As OCP binds to only a single carotenoid, it is ideal for probing intramolecular singlet fission.

Each of these forms can be stabilised to allow spectroscopy experiments to be conducted. Resonance Raman spectra of the two forms indicate a change in carotenoid geometry also takes places when transitioning from OCPr to OCPo. In the OCPo form, a signal attributed to C-H wagging is detected, indicating a twisted geometry for the carotenoid. This signal is absent in the OCPr conformation. Preliminary results by the Clark group have failed to detect singlet fission in either the OCPr or OCPo, suggesting that a twisted geometry is not sufficient for intramolecular singlet fission. The differing electronic environment of OCP, compared to bacteriochlorophylls, may explain the lack of triplet formation in OCP.

To summarise, research into carotenoids in light-harvesting complexes proposes that singlet fission in these species is intramolecular and singlet fission quantum

yields are increased by the carotenoid adopting a twisted geometry. However, studies on OCP have shown that a twisted geometry is not sufficient for intramolecular singlet fission. Therefore, the electronic environment of the light-harvesting complexes could play a significant role in singlet fission, in addition to the geometry adopted along the chain.

As previously discussed, the singlet fission phenomena can be broken down into three processes, depicted below. Changes in geometry and electronic environment could affect each of these processes.

$$S_{OE} \overset{1}{\rightleftharpoons} {}^1(TT) \overset{2}{\rightleftharpoons} {}^1(T\cdots T) \overset{3}{\rightarrow} T+T$$

1 : state interconversion

2 : loss of electronic interaction

3 : spin decoherence

This chapter explores the state interconversion process which is presumed to be intramolecular. In addition, to the observation of intramolecular singlet fission in carotenoids,[13] studies on diphenyl-dicyano-oligoenes (DPDC) revealed an initial intramolecular triplet-pair state singlet forming from the bright state, which then under went intermolecular singlet fission.[62] This process was described as *intra- to intermolcular* singlet fission. The DPDCs used had a conjugation length shorter than natural carotenoids and therefore unlikely to be able to undergo *true* intramolecular singlet fission.

When carotenoids are embedded in photosynthetic centres and OCP, they are surrounded by hydrophobic amino-acid groups, these groups contain phenyl- and other groups that could affect the electron screening experienced by the carotenoid.[149] The Coloumbic parameter U is varied to replicate this change in screening by the

environment. In addition, as found in the previous chapter, changes in conjugation length change the energy ordering of the states. Energy ordering is also affected by changes in U, with the $E^{0-0}(1^1B_u^+) - E^{0-0}(2^1A_g^-)$ gap increasing with conjugation length but also with increase in U.

Using the UV-model and Ehrenfest dynamics, introduced in section 5.2, the initial femtoseconds after photoexcitation are probed for an 18 site chain. To allow conversion from the initial state, a symmetry-breaking term is introduced to the Hamiltonian. By varying the Coulombic parameter, the effect of electronic environment on low energy states and state interconversion is investigated. In addition, the relaxation of the low energy states on their surfaces is investigated in section 5.3.1. By identifying relaxed geometries in this manner, bond dimerisation results from the previous chapter can be corroborated. Furthermore, by investigating dynamics with no interconversion/no symmetry breaking, signatures of each of the low lying states are found, allowing their involvement in state interconversion to be identified. Finally, the focus will turn to the state interconversion of the photoexcited state.

5.2 Methods

5.2.1 UV-Peierls model and Ehrenfest dynamics

The evolution of the photoexcited state is carried out using the time-dependent density matrix renormalisation group method. As described in Section 3.3, this method is most convenient to use when Hamiltonians include only nearest neighbour interactions. This work therefore, uses the UV-Peierls Hamiltonian defined as

$$\hat{H}_{UVP} = \hat{H}_{UV} + \hat{H}_{e-p} + \hat{H}_{ph} \tag{5.1}$$

where $\hat{H}_{UV}$ is the electronic UV or extended Hubbard Hamiltonian

$$\begin{aligned}\hat{H}_{UV} =& \sum_i \epsilon_i \hat{N}_i - \sum_{i,\sigma} t_i \left(\hat{c}^\dagger_{i+1\sigma}\hat{c}_{i\sigma} + \hat{c}^\dagger_{i\sigma}\hat{c}_{i+1\sigma}\right) \\ &+ U\sum_i \left(\hat{N}_{i\uparrow} - \frac{1}{2}\right)\left(\hat{N}_{i\downarrow} - \frac{1}{2}\right) + V\sum_i \left(\hat{N}_{i\uparrow} - 1\right)\left(\hat{N}_{i+1\downarrow} - 1\right)\end{aligned} \tag{5.2}$$

which includes only on-site and nearest neighbour Coulombic interactions. When applying this model to π-conjugated systems, the physically relevant parameter regime is $U > V > 0$. To reduce the parameter space of the model, only a fixed ratio of $U/V = 4$ is considered. For $U > 0$, with this ratio, the ground state has spin-density wave character.[150]

$\hat{H}_{ph}$ describes nuclear contributions and is given by

$$\hat{H}_{ph} = \sum_n \left(\frac{p_n^2}{2m} + \frac{K}{2}(u_{n+1} - u_n)^2\right) \tag{5.3}$$

The coupling between the electrons and the lattice is given by

$$\hat{H}_{e-ph} = \alpha \sum_n (u_{n+1} - u_n)\hat{T}_{n,n+1} \tag{5.4}$$

where $\hat{T}_{n,n+1} = \sum_\sigma \hat{c}^\dagger_{n\sigma}\hat{c}_{n+1\sigma} + \hat{c}^\dagger_{n+1\sigma}\hat{c}_{n\sigma}$. In this work, like in the previous chapter, the electron-nuclear coupling constant of Barford and co-workers,[73] $\alpha = 4.593$ eV Å^{-1} was used which corresponds to a dimensionless coupling constant of $\lambda = 0.115$. In Eqs. (5.3) and (5.4), the nuclei are treated classically, allowing the Ehrenfest approximation to be used (discussed later). The electrons, however, are treated quantum mechanically and their dynamics are determined by the time-dependent Schrödinger equation (TDSE), given by,

$$i\hbar\frac{\partial}{\partial t}\left|\Psi(t)\right\rangle = \hat{H}_{UVP}\left|\Psi(t)\right\rangle \tag{5.5}$$

The evolution of the TDSE is achieved using t-DMRG. Simultaneously, the classical motion of the nuclei are determined by the associated Newton's equation of motion,

$$\begin{aligned} M_\alpha \mathbf{u}_\alpha &= \mathbf{F}_\alpha(\mathbf{u}_\alpha) \\ &= \nabla_\alpha \left\langle \Psi \middle| \hat{H}_{UVP} \middle| \Psi \right\rangle \end{aligned} \tag{5.6}$$

Here, two separate approximations are made. The first assumption is that the electrons influence the nuclei through a classical field that is the average of all the electrons; this is a mean-field approximation. The second assumption is that the nuclei obey Newtonian mechanics. Despite the mean-field nature of the Ehrenfest dynamics, transitions between different electronic states are possible in this formalism, and it is, therefore, a non-adiabatic method.[151] However, a consequence of the mean-field approximation is that Ehrenfest dynamics do not properly describe dynamics that involve a conical intersection.[152,153] Furthermore, they fail to properly describe exciton decoherence.[152,154–156] These discrepancies will be addressed in Chapter 6. However, Ehrenfest dynamics remains a simple and effective method which can give qualitative insight into non-adiabatic dynamics.

Under the UV-Peierls Hamiltonian the force on each atom, f_l, is

$$f_l = -\frac{\delta \left\langle \Psi \middle| \hat{H} \middle| \Psi \right\rangle}{\delta u_l} = -\left\langle \frac{\delta H}{\delta u_l} \right\rangle = -\left\langle \frac{\delta H_{e-p}}{\delta u_l} \right\rangle - \left\langle \frac{\delta H_{ph}}{\delta u_l} \right\rangle \tag{5.7}$$

This leads to

$$f_l = -K\left(2u_l - (u_{l+1} + u_{l-1})\right) + \alpha\left(\left\langle \hat{T}_{l-1,l} \right\rangle - \left\langle \hat{T}_{l,l+1} \right\rangle\right) \tag{5.8}$$

The classical treatment of the nuclear degrees of freedom mean that nuclear motion obey the following equations:

$$\frac{dv_l}{dt} = f_l(t) \tag{5.9}$$

and

$$\frac{du_l}{dt} = \frac{p_l(t)}{m}, \tag{5.10}$$

where v_l and p_l are the velocity and momentum respectively of nucleus l.

To encourage the relaxation of the nuclei, a phenomenological damping term is introduced, which acts as friction for the nuclei. Including this term, the time derivative of the momentum becomes:

$$\frac{dp_l}{dt} = -K\left(2u_l - (u_{l+1} + u_{l-1})\right) + \alpha\left(\left\langle \hat{T}_{l-1,l} \right\rangle - \left\langle \hat{T}_{l,l+1} \right\rangle\right) - \gamma p_l \tag{5.11}$$

The damped velocity Verlet scheme (derivation in appendix 5.A) is used for updating the positions and momenta of the nuclei:

$$u_l(t + \Delta t) = u_l(t) + \frac{p_l \Delta t}{M} + \frac{1}{2M}\left[f_l(t) - \gamma p_l(t)\right]\Delta t^2 \tag{5.12}$$

$$p_l(t + \Delta t) = \frac{1}{1 + \Delta t\gamma/2}\left[p_l(1 - \Delta t\gamma/2) + \frac{\Delta t}{2}(f_l(t) + f_l(t + \Delta t))\right] \tag{5.13}$$

The UVP Hamiltonian depends parametrically on the location of the nuclei $\mathbf{u} = (u_1, u_2, ...u_N)$. As the timescales of electronic and nuclear motion differ by an order of magnitude, we can evolve the electrons for a number of t-DMRG time steps before updating the nuclear positions. To calculate dynamics the following protocol is used:

1. Evolve the system for n time steps under the Trotter decomposition corresponding to $\mathbf{u}$ via the t-DMRG method (section 3.3.2).

2. After the nth time step calculate the bond order $\langle T \rangle$ across the chain and use it to calculate the force, f_l.

3. Using the new force, update the positions of the nuclei, $\mathbf{u}'$, as per the velocity Verlet scheme, given in Eqs. (5.12) and (5.13).

4. Calculate a new Trotter decomposition $\hat{H}(\mathbf{u}')$ with the new nuclear positions. Let $\mathbf{u}' = \mathbf{u}$ and calculate the new $\{t_n\}$

$$t'_n = t^0_n - \alpha\left(u_{n+1} - u_n\right) \tag{5.14}$$

5. Repeat from step 1, until the desired time has been simulated.

In this work, to keep the Verlet error smaller than the t-DMRG error, the nuclear positions are updated every three t-DMRG time steps.

5.2.2 Symmetry breaking

The UVP Hamiltonian, with uniform or dimerised parameters, possesses both C_2 and particle-hole symmetries and as such dynamics evolving under this Hamiltonian will maintain these symmetries. These symmetries will prevent the $1^1B_u^+$ optical state from either undergoing singlet fission or relaxing to the $1^1A_g^-$ ground state via the $2^1A_g^-$ state. To allow dynamics and mixing between all singlet states in this work, particle-hole and C_2 symmetry is broken with the following term:

$$H_{SB} = +\epsilon\hat{N}_1 - \epsilon\hat{N}_N \tag{5.15}$$

This term changes the on-site energy at either end of the chain. The inclusion of this term is well-justified in studying singlet fission, as substituted push-pull or donor-acceptor polymers are known to undergo singlet fission.[157,158] In addition, carotenoids which undergo singlet fission will often have terminal ketone groups (heteroatoms) such as astaxanthin.[59] The presence of these heteroatoms break particle-

hole symmetry and affects the end-of-chain site energies. A positive site energy corresponds to a donor group and a negative site energy to an acceptor group. In this study, $|\epsilon|$ is limited to 1 eV, as this should break the symmetry without significantly changing the character of the states.[115]

5.3 Results

5.3.1 Potential energy surfaces

Starting from the groundstate dimerised geometry and calculating the damped Ehrenfest dynamics without symmetry breaking ($\gamma = \omega$ and $\epsilon = 0$ eV) for each state gives insight to their potential energy surfaces (PES). Assuming a state relaxes on its PES and there is no non-adiabatic coupling to other states, the relaxed geometry should be the same as found through the Hellmann-Feynman procedure (Chapter 4). Fig. 5.1 illustrates the evolution with damping of the total of energy of the low energy singlet and quintet states. For all U values, the $1^1B_u^-$, Q and $1^1B_u^+$ states relax on their surfaces without coupling to other states. The $2^1A_g^-$ and $3^1A_g^-$ states both couple to lower $^1A_g^-$ sector states; the $2^1A_g^-$ state couples more strongly to the $1^1A_g^-$ than the $3^1A_g^-$ couples to the lower states.

As this work is concerned with the dynamics of the photoexcited state, only states that lie below or near in energy to the $1^1B_u^+$ state are considered. The energy ordering of the states is given in Table 5.1.

As U increases, so does the energy of the $1^1B_u^+$ state relative to the other states. This is due to its predominantly electron-hole nature; double or zero occupation of sites is disfavoured by a larger U. In addition, the $1^1B_u^+$ has a smaller relaxation energy (the difference between the initial dimerised and relaxed energies) than the triplet pair states, as was found in Chap. 4.

When $U = 4$ eV, the vertical $2^1A_g^-$ energy is above the vertical $1^1B_u^+$ energy, upon

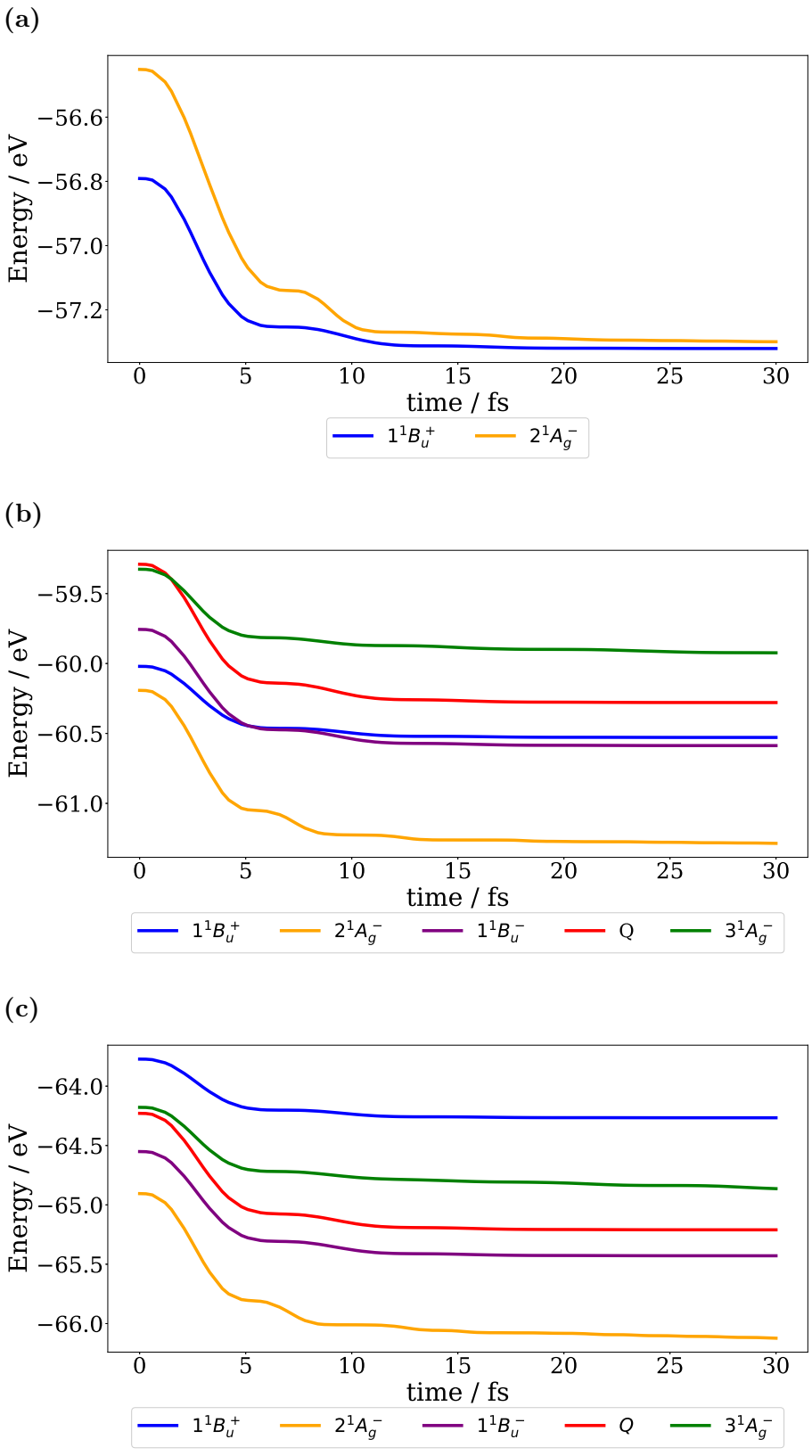


Figure 5.1: Total energy with $\gamma = \omega$ damping of low energy states for an 18 site chain (a) $U = 4$ eV, (b) $U = 6$ eV and (c) $U = 8$ eV.

U	4	6	8
Lowest energy state	$1^1B_u^+$	$2^1A_g^-$	$2^1A_g^-$
	$2^1A_g^-$	$1^1B_u^-$	$1^1B_u^-$
		$1^1B_u^+$	Q
		Q	$3^1A_g^-$
Highest energy state		$3^1A_g^-$	$1^1B_u^+$

Table 5.1: Energy ordering of relaxed low energy states for a 18 site chain for $U = 4, 6, 8$ eV.

relaxation the energy gap between the state decreases significantly. At $U = 6$ eV, the energy ordering is reversed, and the vertical $2^1A_g^-$ energy is below the vertical $1^1B_u^+$ energy. The gap between the $1^1B_u^+$ and $1^1B_u^-$ states is also decreased. At $U = 8$ eV, the $1^1B_u^+$ relaxed state lies higher in energy than the other singlet states as well as the quintet state. At this Coulombic interaction strength, the closest state is $3^1A_g^-$. Across all the U values, the energy ordering of $2^1A_g^- < 1^1B_u^- < 3^1A_g^-$, is observed at vertical and relaxed geometries, further confirming these states as belonging to the same family. The energy ordering of vertical and relaxed state for $U = 6$ eV most closely matches that of a $N = 18$ site chain with PPPP Hamiltonian from the previous chapter.

Fig. 5.2 shows the staggered bond dimerisation of the states after 30 fs of the damped dynamics. The Q and $1^1B_u^-$ display the same four soliton dimerisation patterns previously found with the Hellmann-Feynman routine. The $1^1B_u^+$ also resembles the Hellmann-Feynman bond dimerisation. As U decreases the relaxed $2^1A_g^-$ geometry becomes less dimerised, with $U = 4$ eV and the distinction between each of the four solitons becomes difficult.

The relaxed $3^1A_g^-$ state ($U = 6, 8$ eV) has the characteristic six soliton ($SS\bar{S}S\bar{S}\bar{S}$) dimerisation, again, however, the dimerisation diminishes with lower U.

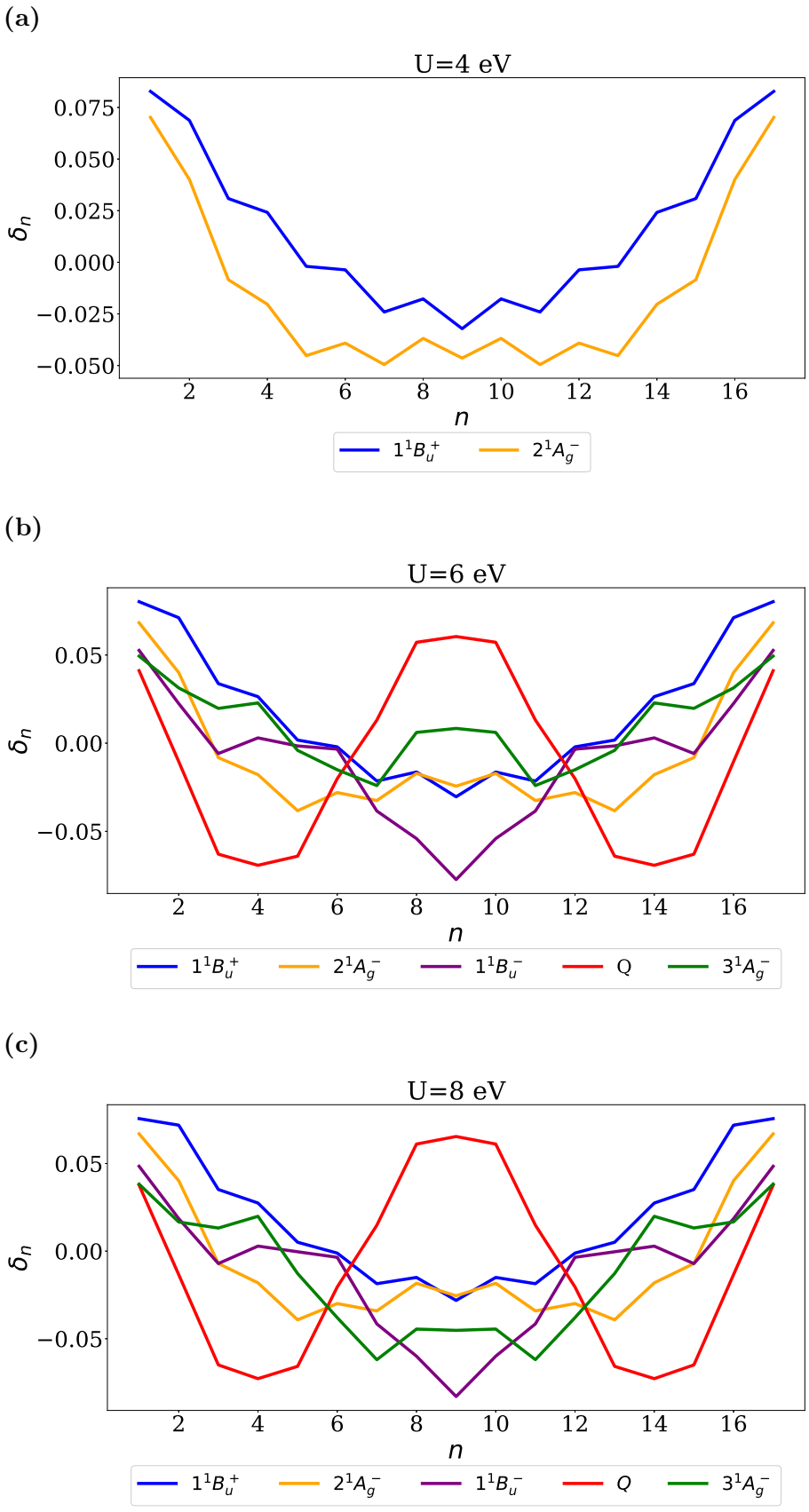


Figure 5.2: Staggered bond dimerisation after 30 fs of $\gamma = 1.0$ damped dynamics for the low energy singlet and quintet states for (a) $U = 4$ eV, (b) $U = 6$ eV and (c) $U = 8$ eV.

5.3.2 Identification of states

Having established the energy ordering of the states, it is necessary to ascertain observables that are distinct for each of the low energy states. These observables can then be used to keep track of the photoexcited states during state interconversion.

Ionicity

The total ionicity operator[159] is defined as

$$\sum_n (\hat{N}_n - 1)^2, \tag{5.16}$$

where $\hat{N}_n$ is the number operator for site n. The total ionicity operator is a measure of the amount of double-occupied and non-occupied sites a state has and therefore indicates the magnitude of ionic contributions.

The evolution of the ionicity for each of the low energy singlet states is shown in Fig. 5.3. The $1^1B_u^+$ state has the largest ionicity of these states, as expected, and unlike the other states, the ionicity of the $1^1B_u^+$ is highly consistent throughout. As U increases, the ionicity of all states decreases, with the decrease being less pronounced for the $1^1B_u^+$ state.

The $2^1A_g^-$ has the next largest ionicity, which fluctuates with time. These fluctuations, whose magnitude decreases with increasing U, can be partially explained by coupling to the ground state, which has a larger ionicity than the $2^1A_g^-$ state.[159] Additionally, the $3^1A_g^-$ state also shows some fluctuations when $U = 6$ eV, which again may be due to coupling. The quintet Q state has the lowest ionicity due to its decreased ionic character. Each of the states have both electron-hole and triplet pair components, and we witness Rabi oscillation between these components. As U gets larger the energy difference between the components increases and the oscillation

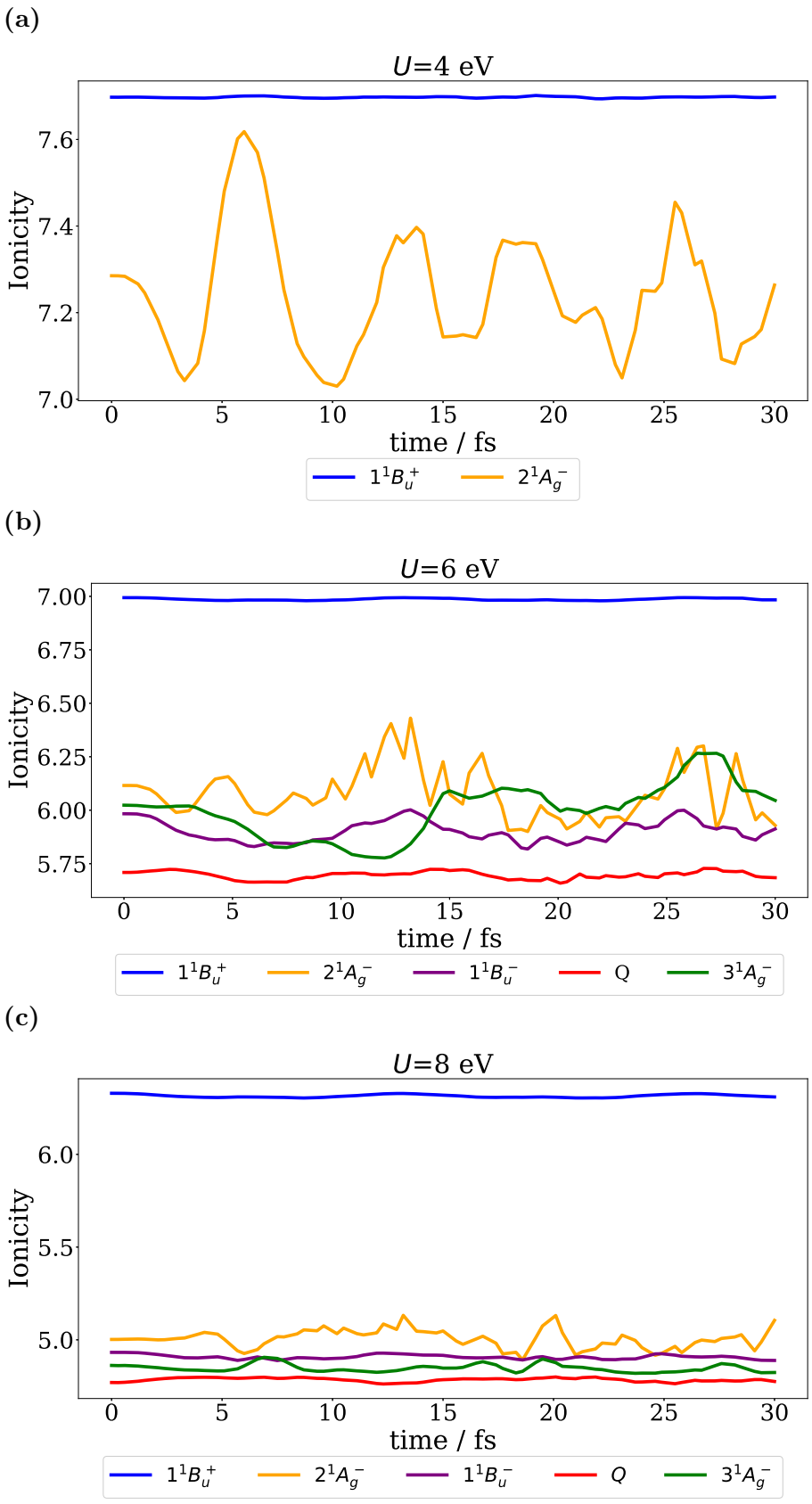


Figure 5.3: Total ionicity with critical damping of low energy state for an 18 site chain, (a) $U = 4$ eV, (b) $U = 6$ eV and (c) $U = 8$ eV.

decrease in amplitude and their period is also reduced.

Since the ionicity for the $1^1B_u^-$ state is distinct (larger in magnitude and does not fluctuate) any decrease in ionicity will indicate the state losing $1^1B_u^-$ character and gaining triplet-pair character.

Spin-spin correlations

The low energy states of polyenes have both ionic and spin-wave (covalent) character. As shown in the previous chapter, the spin-spin correlation can give insight into the spin-wave character of a state.

The evolution of the spin-spin correlations $\langle S_1 S_{18} \rangle$, $\langle S_4 S_{15} \rangle$ and $\langle S_1 S_4 \rangle$ for $U = 6$ eV is depicted in Fig. 5.4, while the correlations for $U = 8$ eV are found in Appendix 5.B. The correlations for all U values show the same general trends. The low energy triplet pair states exhibit long-range spin-spin correlations while for the $1^1B_u^+$ state, $\langle S_1 S_{18} \rangle$ and $\langle S_4 S_{15} \rangle$ are close to zero during the evolution, meaning a gain in magnitude of these correlations will indicate that the photoexcited state has gained triplet-pair character.

In addition, the spin-spin correlation can be used to differentiate between the triplet-pair states. Considering $\langle S_4 S_{15} \rangle$, the $1^1B_u^-$ state has a positive correlation, while the $3^1A_g^-$ state exhibits a negative correlation. For the $2^1A_g^-$ state, the correlation fluctuates, with mostly non-zero magnitude. The $\langle S_1 S_4 \rangle$ correlation is less negative for the $3^1A_g^-$ and $1^1B_u^-$ states compared to the $2^1A_g^-$ and $1^1B_u^+$ states, though the fluctuation in magnitude is significant for the $2^1A_g^-$ state. In polyenes after photoexcitation a system will either relax via the $2^1A_g^-$ state or undergo singlet fission via a different triplet-pair state. Using the $\langle S_1 S_4 \rangle$ and $\langle S_4 S_{15} \rangle$ correlations, the specific triplet-pair state the bright state converts to can be tracked.

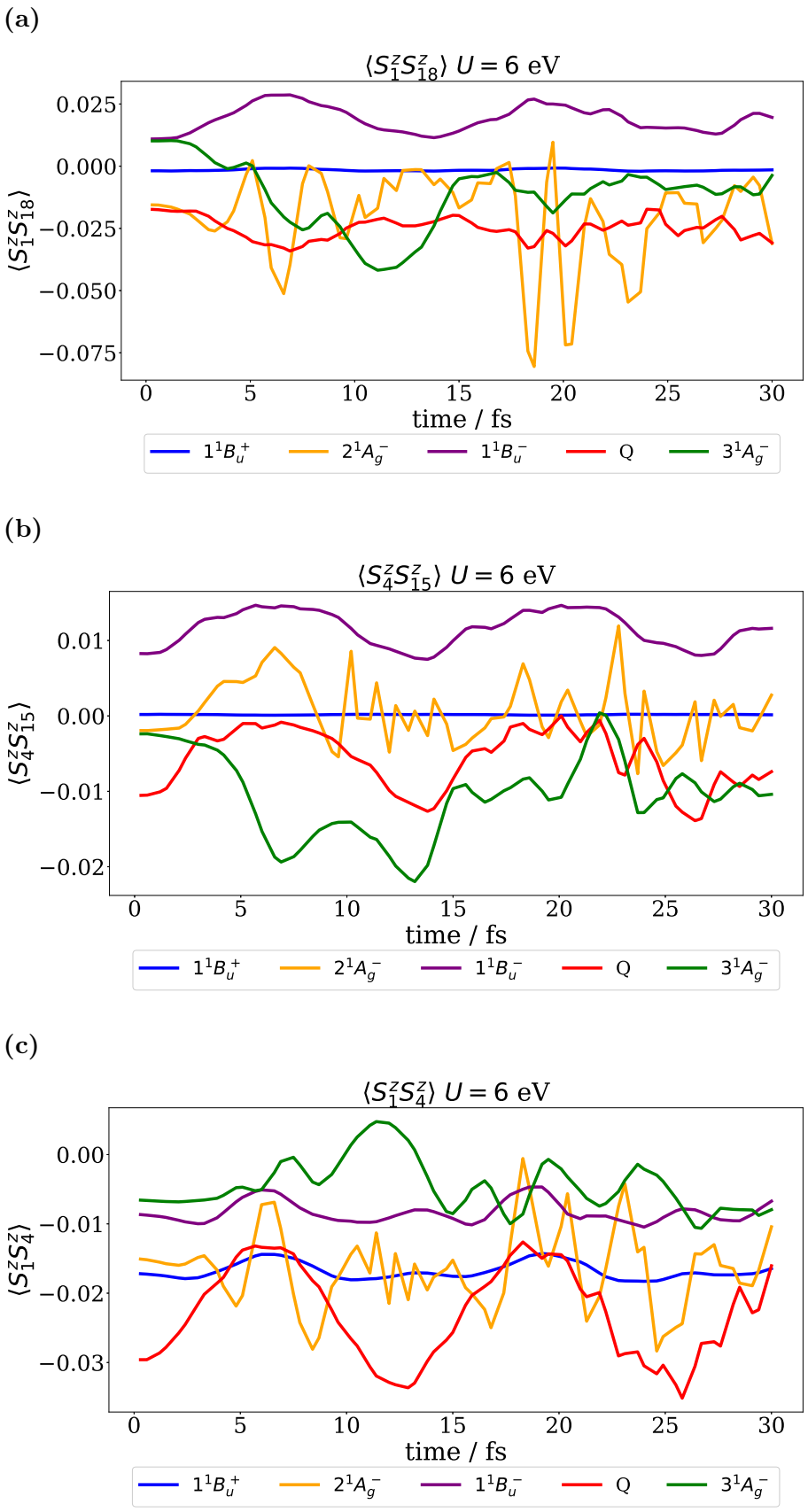


Figure 5.4: Evolution of $\langle S_1 S_{18} \rangle$, $\langle S_4 S_{15} \rangle$ and $\langle S_1 S_4 \rangle$ correlations for the low energy states with $U = 6$ eV with no symmetry breaking.

Bond Dimerisation

It has already been observed that the solitonic structure of each of the low energy states is distinct, and this leads to characteristic relaxed staggered bond dimerisation. In addition, the staggered bond dimerisation, when calculated for undamped dynamics, is unique for each of the states, and this is illustrated in Appendix 5.C. The bond dimerisation can therefore also provide insight into which state the photoexcited state is evolving.

5.3.3 Dynamics of the $1^1B_u^+$ state

The first step of singlet fission, state interconversion, was probed by calculating dynamics starting from the vertical $1^1B_u^+$ state. The $1^1B_u^+$ state is the lowest energy optical state and has the largest dipole moment from the ground state. Thus the vertical $1^1B_u^+$ state makes a good approximation to the photoexcited state.[158] The initial vertical state was always calculated without symmetry breaking, as the DMRG routine is most accurate when symmetries are applied. H_{SB} was only introduced for the time evolution of the state. In real systems, symmetry breaking terms will likely fluctuate during dynamical processes. As the aim of this work is to gain qualitative insight into the state interconversion, introducing the symmetry breaking only for the time-evolution with a small magnitude, e.g. 1 eV, is valid.

Ionicity

The evolution of the ionicity of the photoexcited state with a range of U values is presented in Fig. 5.5. When $\epsilon > 0$, the total ionicity decreases for all U values, implying that the states gain some non-$1^1B_u^+$ state character. The magnitude in the change of the ionicity increases with increasing U. For $U = 6$ and 8 eV, the lowering of the ionicity is most substantial when $\epsilon = 1.0$ eV. For $U = 4$ eV, the $2^1A_g^-$

and $1^1B_u^+$ relaxed energies were found to be very close in energy. As such when $\epsilon = 1.0$, after an initial rapid change, the ionicity oscillates and fluctuates back to the $1^1B_u^+$ magnitude. When U increases to 6 eV, the $\epsilon = 1.0$ eV ionicity also displays oscillations but there as an overall trend of lowering magnitude. Taking magnitude into account, the decrease in ionicity is most substantial for $U = 6$ eV, suggesting the gain in triplet-pair state character is largest.

Now considering the inclusion of damping, for $U = 6$ eV, rather than facilitating relaxation to other states, reduces the change in ionicity. This indicates that for this parameter regime, state interconversion may involve a high energy region of the $1^1B_u^+$ PES or conical intersection, and is in contrast to the $U = 8$ eV dynamics where damping is found to enhance the change in ionicity.

Overall, these results indicate that state interconversion takes places very rapidly and for all electronic environments (all Coulombic parameter values), during evolution, the initially photoexcited state gains the character of a triplet-pair state.

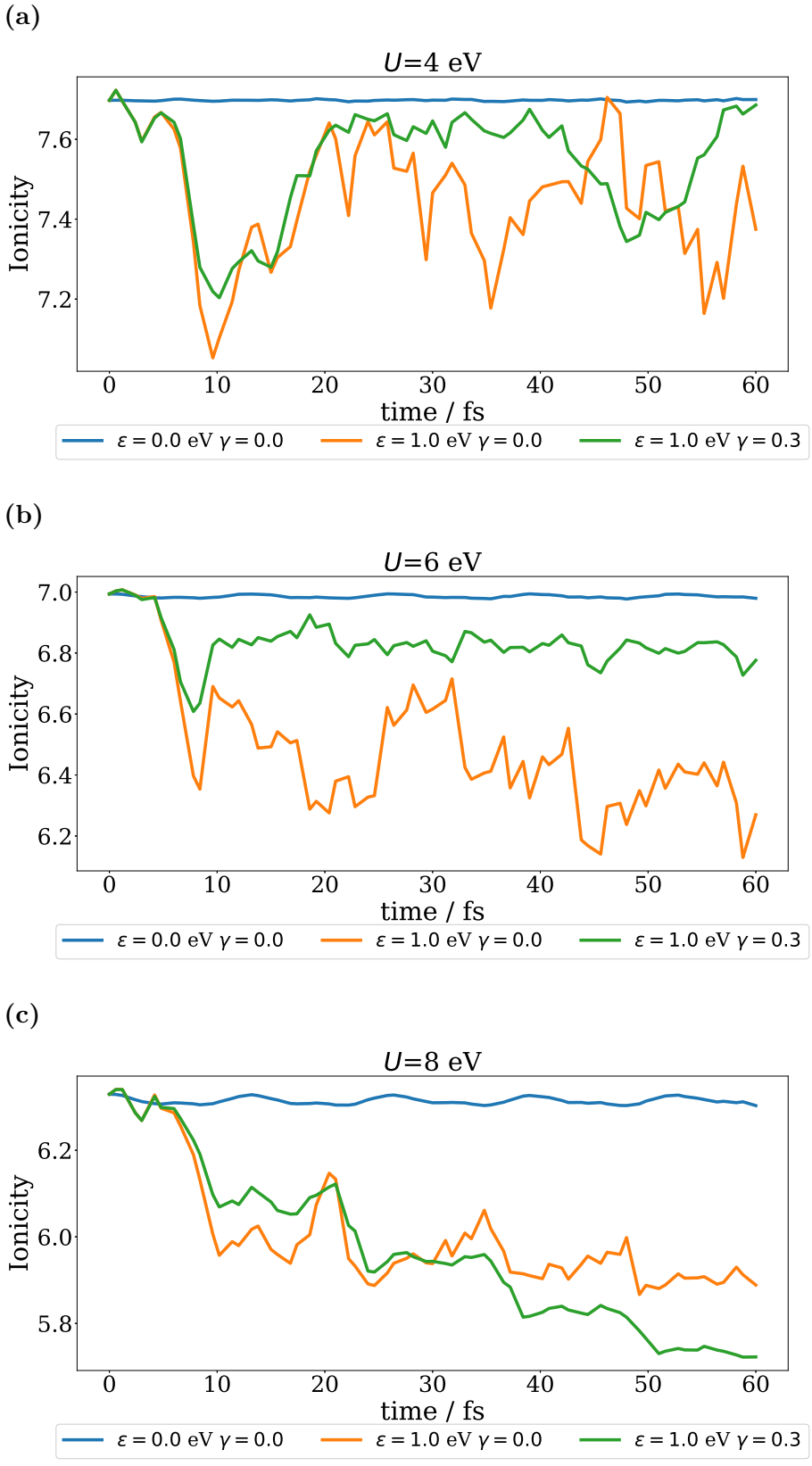


Figure 5.5: Evolution of the total ionicity of the photoexcited state for different ϵ and for U = (a) 4 eV, (b) 6 eV, and (c) 8 eV.

Spin-spin correlation

The presence of long-range spin-correlations indicates that a singlet state has some spin-wave density and triplet-pair character. The evolution of the spin-spin correlations $\langle S_1 S_{18} \rangle$, $\langle S_4 S_{15} \rangle$ and $\langle S_1 S_4 \rangle$ for different values of U are depicted in Figs. 5.6-5.8.

Turning first to the $U = 4$ eV results, there is a strong correlation between $\langle S_1 S_{18} \rangle$ and the ionicity (Fig. 5.5a), indicating that as the state loses electron-hole character (which contributes to ionicity) it gains spin-wave density character. The oscillation in magnitude suggests that interconversion is reversible with the evolving state moving between $1^1B_u^+$ and $2^1A_g^-$ character.

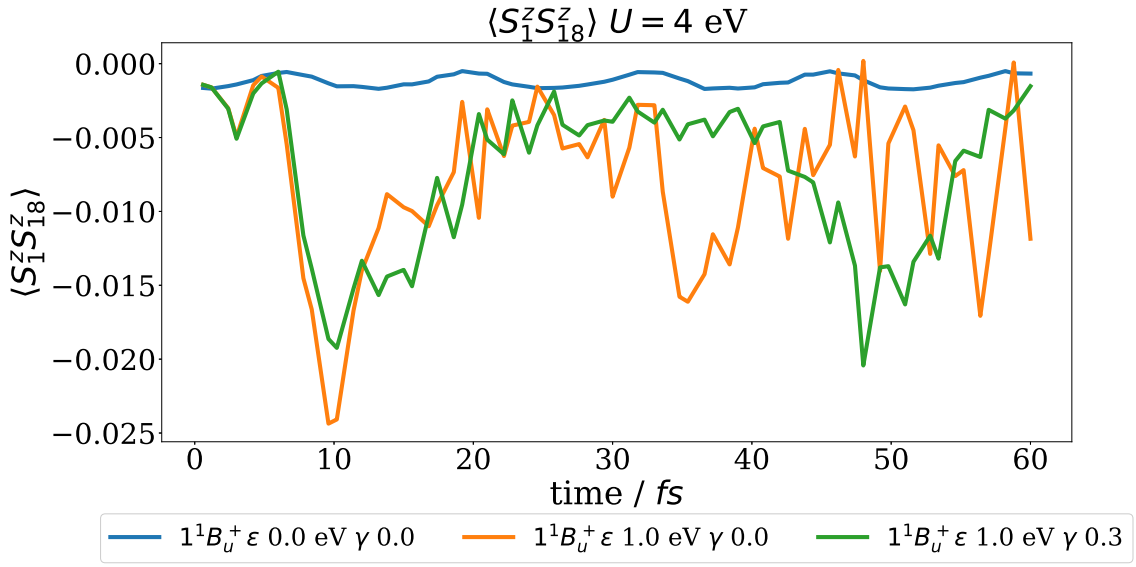


Figure 5.6: Dynamics of the spin correlations$\langle S_1 S_{18} \rangle$ for $U = 4$ eV.

For $U = 6$ eV, the spin-spin correlations again show rapid fluctuations. Despite this, the $\langle S_1 S_{18} \rangle$ correlation generally increases in magnitude with increased symmetry breaking. Based solely on relaxed energy gap considerations (Fig. 5.1b), state interconversion from the $1^1B_u^+$ state to the $3^1A_g^-$state is expected to be preferred over interconversion to the $2^1A_g^-$ state. The small energy gap between the states can lead to large non-adiabatic couplings, and even crossover via a conical inter-

section. The $\langle S_1 S_{18} \rangle$ correlation is found to be negative. Furthermore, the $\langle S_4 S_{15} \rangle$ correlation fluctuates at high frequency about zero, behaviour resembling that of the $2^1A_g^-$ state (Fig. 5.4b). Similarly, the $\langle S_1 S_4 \rangle$ correlation, on average, becomes less negative than the $1^1B_u^+$ correlation and fluctuates like the $2^1A_g^-$ state correlation.

As U is increased to 8 eV, the energy gap between the $1^1B_u^+$ and $2^1A_g^-$ state is increased (Fig. 5.1c), and the state nearest in energy to the bright state is the $3^1A_g^-$. Again, the symmetry breaking term induces a gain in magnitude of the end-to-end spin-spin correlation (Fig. 5.8). It is worth noting that when $\epsilon = 1.0$ eV, $\gamma = 0.3$, which led to the biggest change in ionicity, the $\langle S_1 S_{18} \rangle$ oscillates above and below the $1^1B_u^+$ value. This behaviour mirrors that of the $3^1A_g^-$ state (Fig. 5.4a). Also, in contrast to the dynamics when $U = 6$ eV, the $\langle S_4 S_{15} \rangle$ correlation becomes negative with increased symmetry breaking. This, again, is comparable to the $3^1A_g^-$ state (Fig. 5.4b). As before, the $\langle S_1 S_4 \rangle$ correlation, on average, becomes less negative like the $3^1A_g^-$ state.

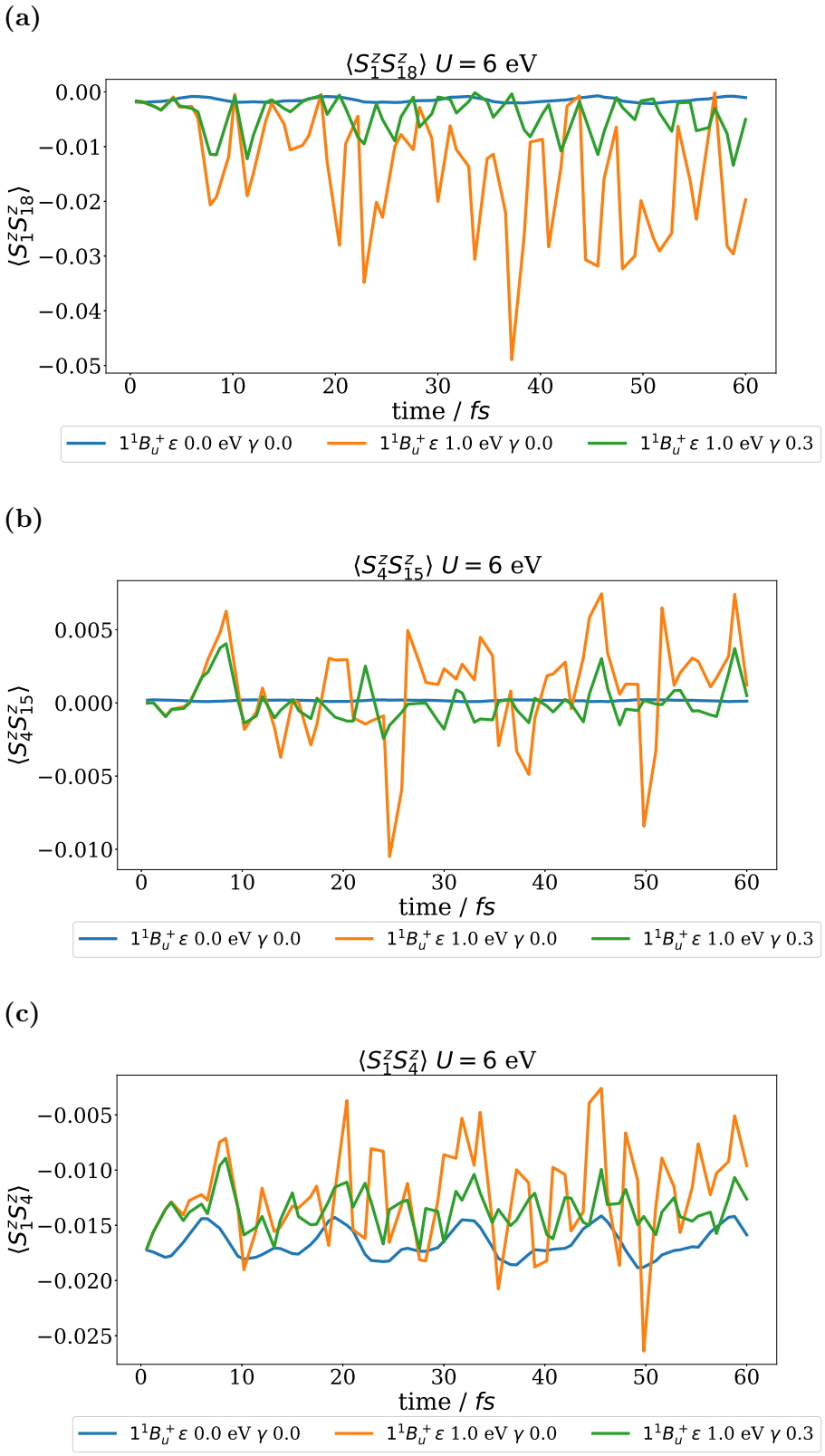


Figure 5.7: Dynamics of the spin correlations (a) $\langle S_1 S_{18} \rangle$, (b) $\langle S_4 S_{15} \rangle$ and (c) $\langle S_1 S_4 \rangle$ for $U = 6$ eV.

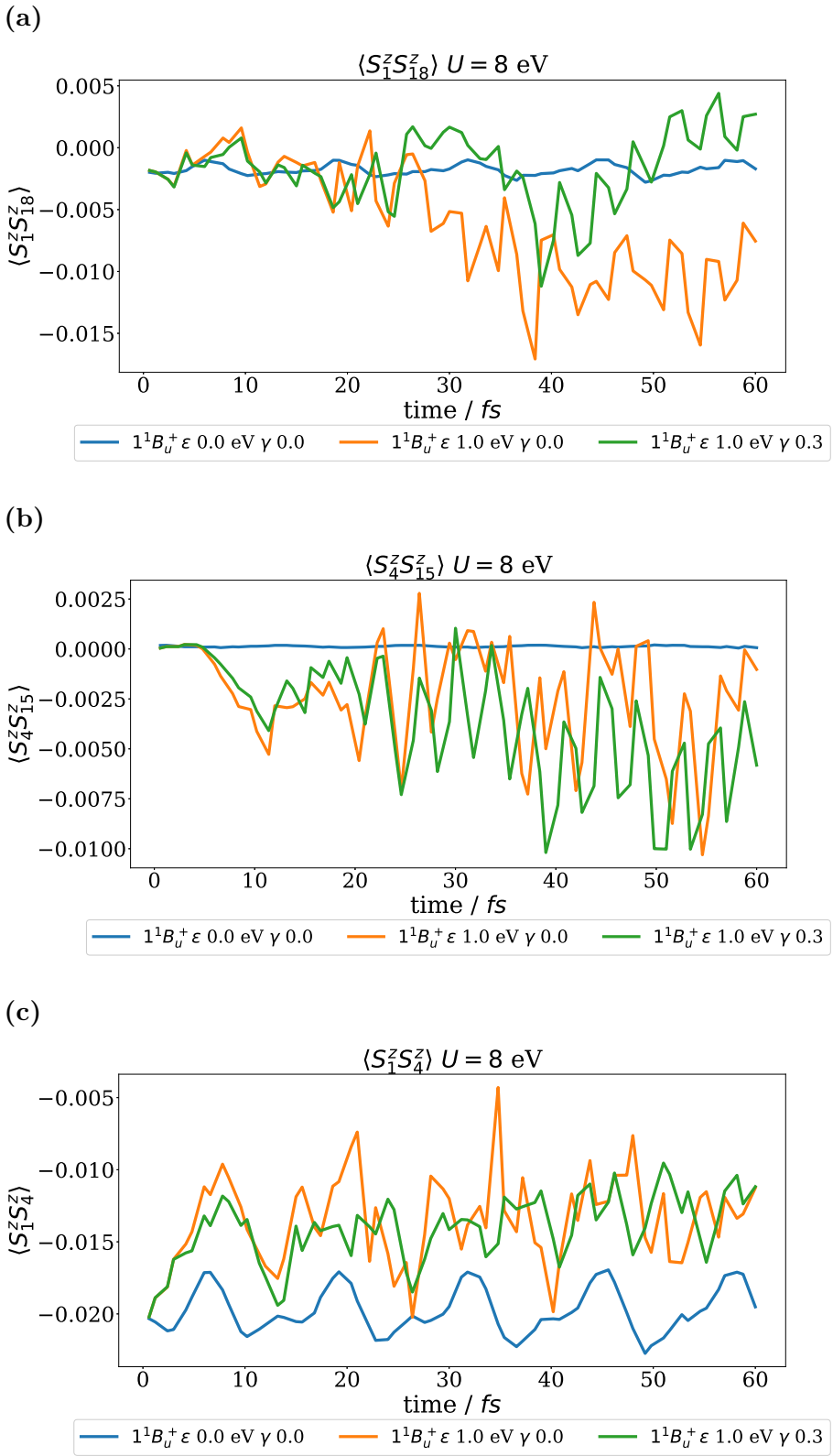


Figure 5.8: Dynamics of the spin correlations (a) $\langle S_1 S_{18} \rangle$, (b) $\langle S_4 S_{15} \rangle$ and (c) $\langle S_1 S_4 \rangle$ for $U = 8$ eV.

Bond dimerisation

The final observable that can give us an indication of which states are involved in interconversion is the staggered bond dimerisation, which we use to investigate $U = 6, 8$ eV.

The bond dimerisation oscillates between positive and negative values in the middle of the chain, for the $1^1B_u^+$ state with no symmetry breaking for all U values (Fig. 5.9). By varying U the evolution of the bond dimerisation changes as illustrated in Figs. 5.10-5.11.

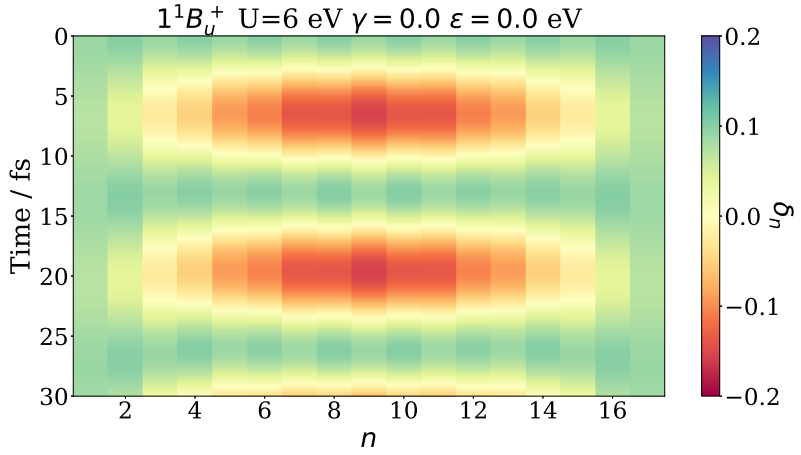


Figure 5.9: Evolution of the staggered bond dimerization of the $1^1B_u^+$ state with no symmetry breaking.

For the $U = 6$ eV case, with symmetry breaking $\epsilon = 1.0$ eV (Fig. 5.10a), oscillations in the staggered bond dimerisation along the chain are no longer in phase; there is a delay between the middle of the chain and the end sites. This resembles the $2^1A_g^-$ staggered bond dynamics, as illustrated in Fig. 5.10b. This agrees with the spin-spin correlation results where we saw a gain in $2^1A_g^-$ character.

In results not presented here, when the dynamics are damped there is only a slight distortion compared to the symmetric $1^1B_u^+$ dynamics, corroborating the ionicity results, that for $U = 6$ eV damping hinders state interconversion.

The evolution of the staggered bond dimerisation of the photoexcited state with

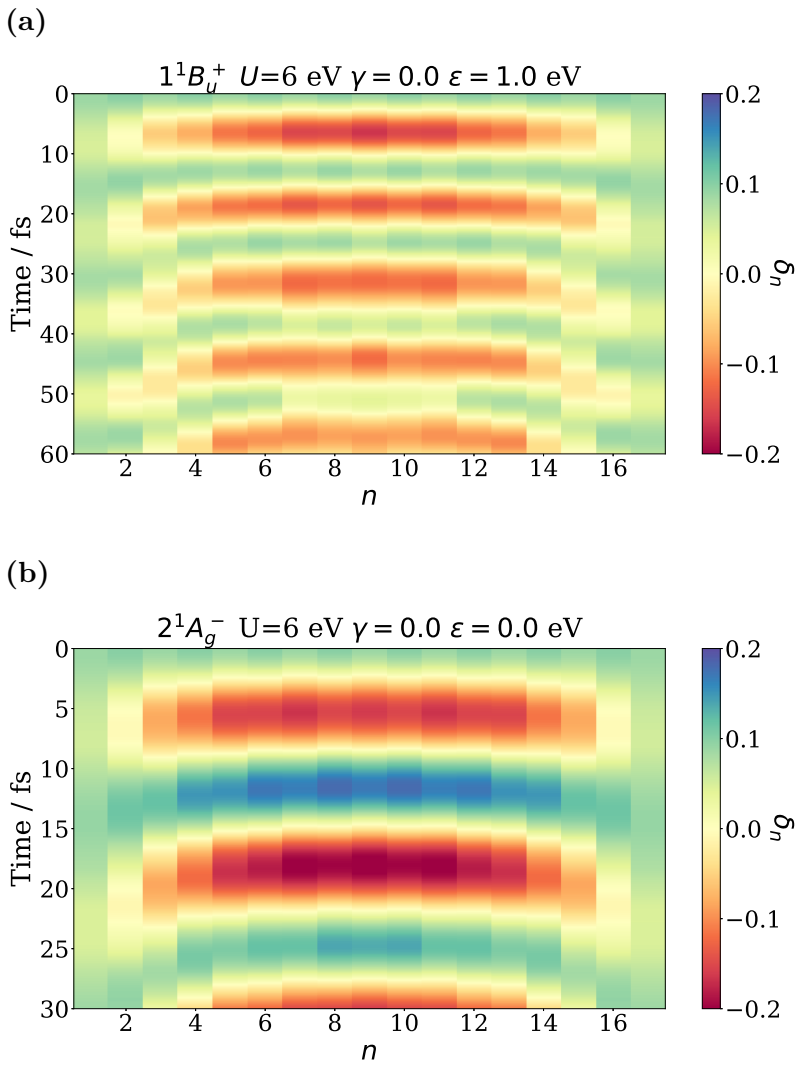


Figure 5.10: The dynamics of the (a) photoexcited state's staggered bond dimerisation for $U = 6$ eV compared with the $2^1A_g^-$ staggered bond dimerisation.

symmetry breaking and $U = 8$ eV, however leads to a different pattern (Fig. 5.11a). Indeed, the symmetry-broken $U = 8$ eV bond dimerisation resembles that of the $1^1B_u^-$ state (Fig. 5.11b). However, based on spin-spin correlation considerations, state interconversion to the $1^1B_u^-$ state has been ruled out. The symmetry broken photoexcited state bond dimerisation can alternatively be considered as a mixture of the $1^1B_u^+$ (Fig. 5.9) and $3^1A_g^-$ (Fig. 5.11c) bond dimerisations, which would likely result in the observed pattern. This again suggests that when $U = 8$ eV, state interconversion does not involve the $2^1A_g^-$ state.

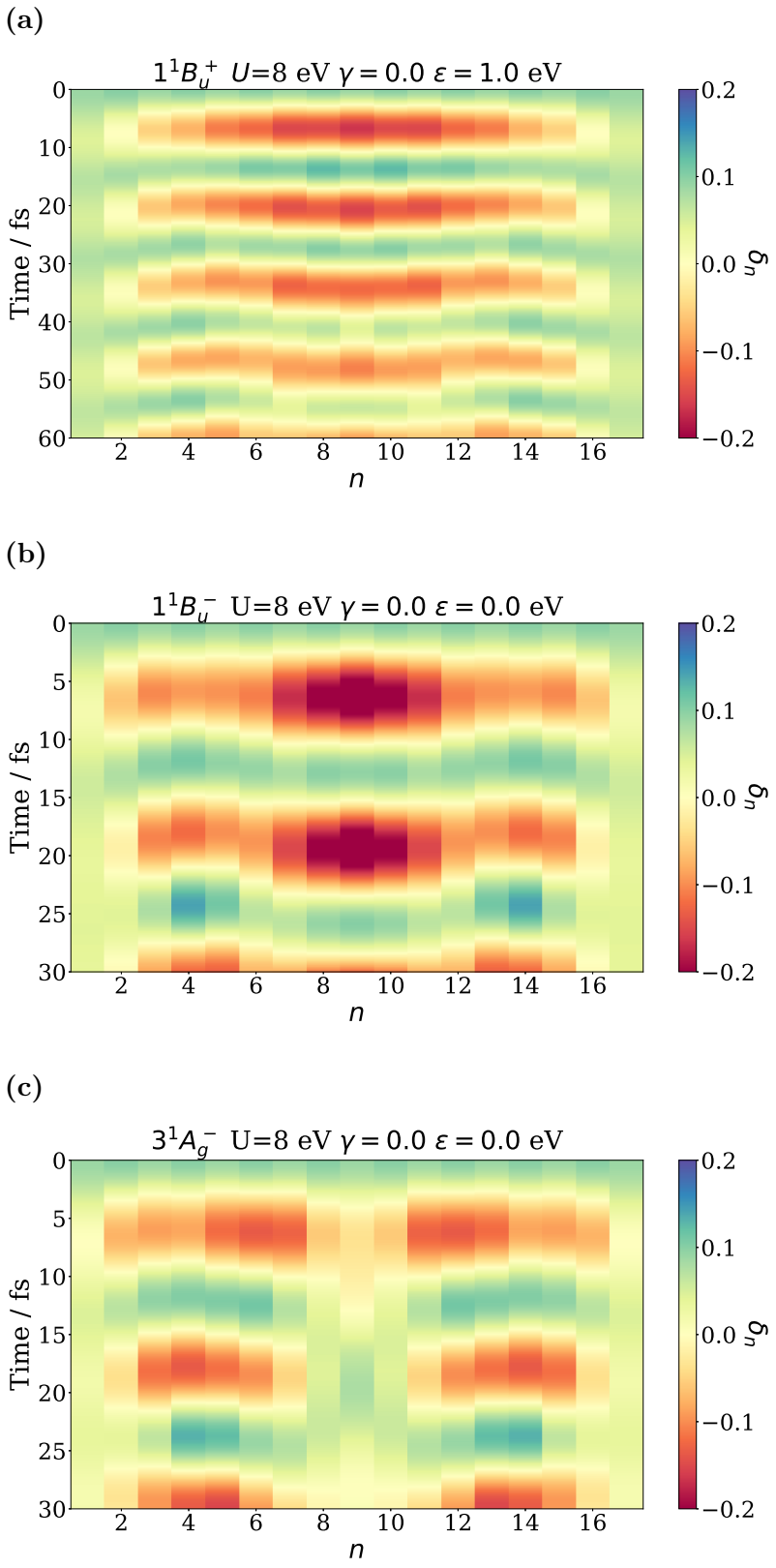


Figure 5.11: The dynamics of the (a) photoexcited state's staggered bond dimerisation for $U = 8$ eV compared to the (b) $1^1B_u^-$ and (c) $3^1A_g^-$ staggered bond dimerisation.

5.4 Conclusions

In this chapter, we set out to investigate the effect of the electronic environment on state interconversion. In addition, the potential energy surfaces of the low energy states were also explored. By calculating the relaxed bond dimerisation, the previously found solitonic structures of the $1^1B_u^+$, $1^1B_u^-$, $2^1A_g^-$, $3^1A_g^-$ and $1^5A_g^-$ states were corroborated. The bond dimerisation, ionicity and spin-spin correlations were established as identifying observables for the state interconversion process.

It was found that for all U values, state interconversion from the $1^1B_u^+$ photoexcited state to a triplet-pair state was fast with modest amounts of symmetry breaking ($\epsilon = 1$). In addition, which state the photoexcited state evolved into was found to be influenced by the strength of Coulombic interaction. When $U = 4$ eV, the $1^1B_u^+$ and $2^1A_g^-$ states were found to couple, and transfer between the states was observed. However, as the energy gap between the states is small, the evolved state fluctuated between $1^1B_u^+$ and $2^1A_g^-$ character, as most evident in the evolving ionicity.

Increasing U to 6 eV, was accompanied by a more consistent decrease in the ionicity for the evolving $\epsilon = 1.0$ eV state, implying state interconversion was more unidirectional than when $U = 4$ eV. In addition, the evolving bond dimerisation showed a large amount of $2^1A_g^-$ character, despite the close energetic proximity of the $1^1B_u^-$ state.

When $U = 8$, a sustained decrease in the ionicity was again observed. However, taking into account the spin-spin correlation results indicated that state interconversion was this time taking place between the $1^1B_u^+$ and $3^1A_g^-$ states.

These results suggest that changes in electronic environment can alter the state interconversion process. At low U the photoexcited state evolves into the $2^1A_g^-$

state, while at higher U the evolution results in a gain in $3^1A_g^-$ character. To the author's knowledge, this is the first work showing dynamics from the $1^1B_u^+$ state to the $3^1A_g^-$ state.

Since the $2^1A_g^-$ state is not thought to be involved in singlet fission and instead represents a deexcitation pathway to the ground state in carotenoids;[59] singlet fission may only proceed in polyene systems when state interconversion to the $3^1A_g^-$ state takes place. This suggests that the reason intramolecular carotenoid singlet fission has only been observed in photosynthetic bacteria may be that the electronic environment of these species facilitate $1^1B_u^+ \rightarrow 3^1A_g^-$ interconversion.

State interconversion to the higher energy $3^1A_g^-$ state can also help explain observations in longer conjugated polymers. As previously noted, for these systems, SF requires a higher energy mid-gap excitation.[117] This work suggests that the mid-gap excitation may lead to a $3^1A_g^-$ relaxation channel, and subsequently singlet fission.

It is worth noting that no interconversion from the $1^1B_u^+$ state to the $1^1B_u^-$ state was observed. In hindsight, this is because the symmetry breaking term is odd with respect to the C_2 and particle-hole symmetries, and therefore, only allows the mixing of the ${}^1A_g^-$ and ${}^1B_u^+$ symmetry sectors. Future work will investigate state interconversion with disordered site energies to completely break the symmetries.

Appendices

5.A Velocity Verlet

To model the classical motion of the nuclei, the damped velocity Verlet method is used.[160,161] Starting with the assumption that the force and acceleration are independent of velocity, from Newton's equations of motion:

$$\dot{x}(t) = v(t) \tag{5.17}$$

$$\dot{v}(t) = \frac{1}{m}F[x(t), t]. \tag{5.18}$$

Taking a Taylor expansion of the displacement, $x(t)$,

$$x(t + \Delta t) = x(t) + v(t)\Delta t + \frac{1}{2}a(t)\Delta t^2 + \frac{1}{6}\dot{a}(t)\Delta t^3 + O(\Delta t^4), \tag{5.19}$$

and considering time-reversible dynamics

$$x(t - \Delta t) = x(t) - v(t)\Delta t + \frac{1}{2}a(t)\Delta t^2 - \frac{1}{6}\dot{a}(t)\Delta t^3 + O(\Delta t^4). \tag{5.20}$$

Combining Eqs. 5.19 and 5.20 gives the Verlet equation for displacement:

$$x(t + \Delta t) = 2x(t) - x(t - \Delta t) + a(t)\Delta t^2 + O(\Delta t^4) \tag{5.21}$$

often expressed as $x_{n+1} = 2x_n - x_{n-1} + \frac{1}{2}a_n\Delta t^2$. To keep track of velocity, $v(t)$ is defined as

$$v(t) = \frac{x(t + \Delta t) - x(t - \Delta t)}{2\Delta t}. \tag{5.22}$$

Adding $x(t + \Delta t)$ to both sides of Eq. 5.21 and using the definition of velocity, the equation for displacement in the velocity Verlet algorithm

$$x(t + \Delta t) = x(t) + v(t)\Delta t + \frac{1}{2}a(t)\Delta t^2 \tag{5.23}$$

is obtained. To use this equation the velocity must also be integrated. By taking Eq. 5.21 for x_{n+1} and x_{n+2}, summing and rearranging:

$$x_{n+2} - x_{n-1} = x_{n+1} - x_{n-1} + \Delta t^2(a_{n+1} + a_n) \tag{5.24}$$

Using the definition of velocity:

$$v_{n+1} = v_n + \frac{1}{2}\Delta t(a_{n+1} + a_n) \tag{5.25}$$

Thus the two equations making up the velocity Verlet algorithm are given as:

$$x_{n+1} = x_n + v_n\Delta t + \frac{1}{2}a_n\Delta t^2 \tag{5.26}$$

$$v_{n+1} = v_n + \frac{1}{2}\Delta t(a_{n+1} + a_n) \tag{5.27}$$

The velocity Verlet integration has a local single step displacement error of $O(\Delta t^4)$. However, over a number of time steps, these errors accumulate, and the overall error for this integration scheme is $O(\Delta t)$.

In deriving the velocity Verlet algorithm, it is assumed that the force and therefore, the acceleration does not depend on velocity. However, in the case that acceleration depends on velocity, $a_{n+1}(x_{n+1}, v_{n+1}, t_{n+1})$, this integration scheme cannot be used. This is because of the updated velocity at $n + 1$ in Eq. (5.25) depends on the acceleration, and therefore, the velocity at $n + 1$. One possible solution is to calculate an approximate velocity, v'_{n+1} using an acceleration based on a velocity of

$v_n + a_n \Delta t$ and then correcting so that the Verlet update scheme becomes:

$$x_{n+1} = x_n + v_n \Delta t + \frac{1}{2} a_n \Delta t^2 \tag{5.28}$$

$$v'_{n+1} = v_n + \frac{1}{2} \Delta t \left[a_n + a(x_{n+1}, v + a_n \Delta t, t_{n+1}) \right] \tag{5.29}$$

$$v_{n+1} = v_n + \frac{1}{2} \Delta t \left[a_n + a(x_{n+1}, v'_{n+1}, t_{n+1}) \right] \tag{5.30}$$

However, the damped velocity Verlet integration scheme can be simplified for the case of linear damping. In this case, the acceleration can be written as

$$a_n = \frac{1}{m} \left[F_n(x_n, t_n) - \gamma m v_n \right] \tag{5.31}$$

where $\gamma v = (x_{n+1} - x_{n-1})/2\Delta t$. Subbing into Eqn. 5.24 and rearranging gives:

$$x_{n+1} = x_n + v_n \Delta t + \frac{1}{2} a_n \Delta t^2 \tag{5.32}$$

$$v_{n+1} = \frac{1}{1 + \Delta t \gamma / 2} \left[v_n (1 - \Delta t \gamma / 2) + \frac{\Delta t}{2m} (F_{n+1} + F_n) \right] \tag{5.33}$$

5.B Spin-spin correlation

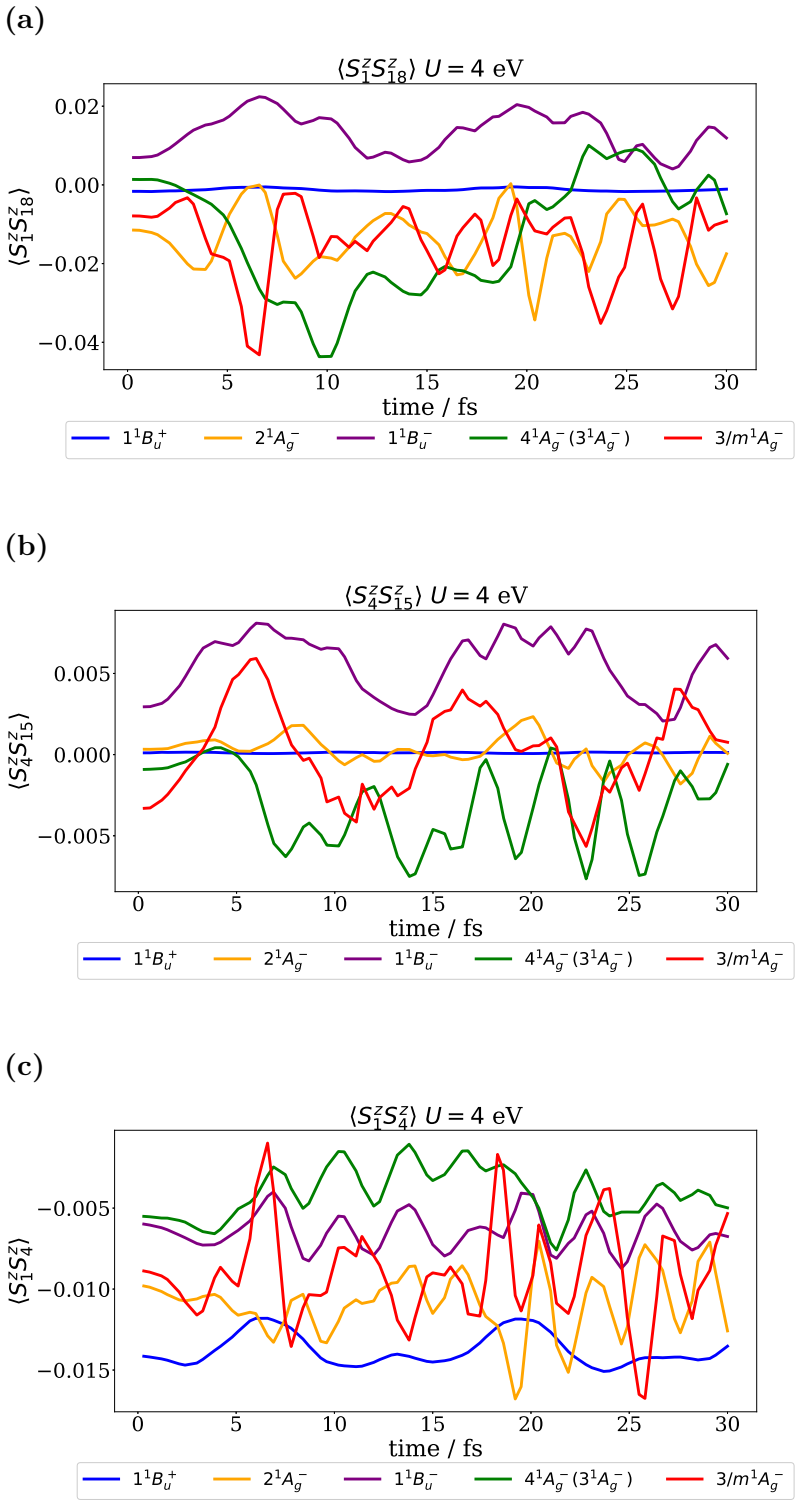


Figure 5.B.1: Evolution of $\langle S_1 S_{18} \rangle$, $\langle S_4 S_{15} \rangle$ and $\langle S_1 S_4 \rangle$ correlations for the low energy states with $U = 4$ eV.

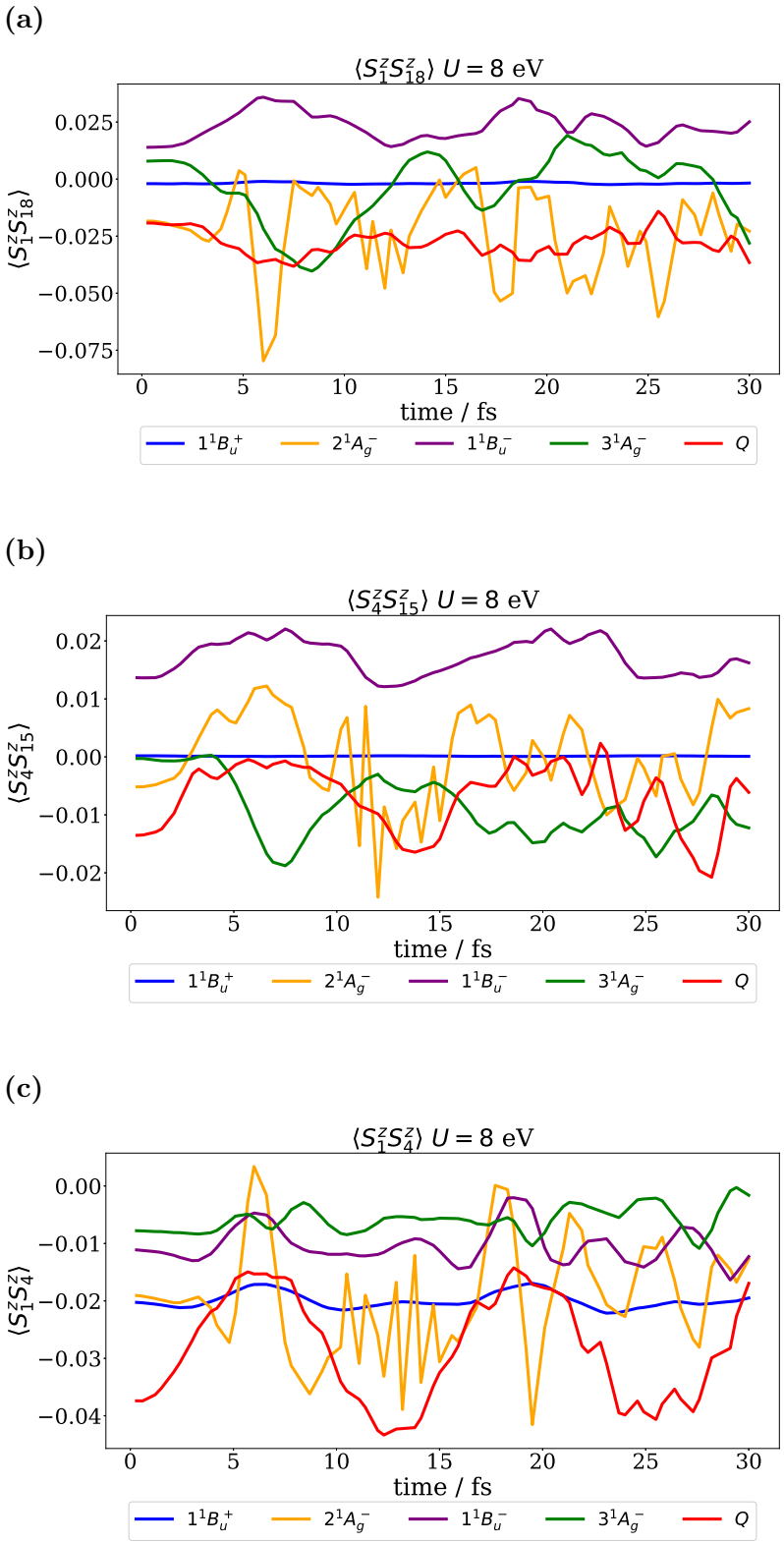


Figure 5.B.2: Evolution of $\langle S_1 S_{18} \rangle$, $\langle S_4 S_{15} \rangle$ and $\langle S_1 S_4 \rangle$ correlations for the low energy states with $U = 8$ eV.

5.C Dynamics of bond dimerisation of low energy states

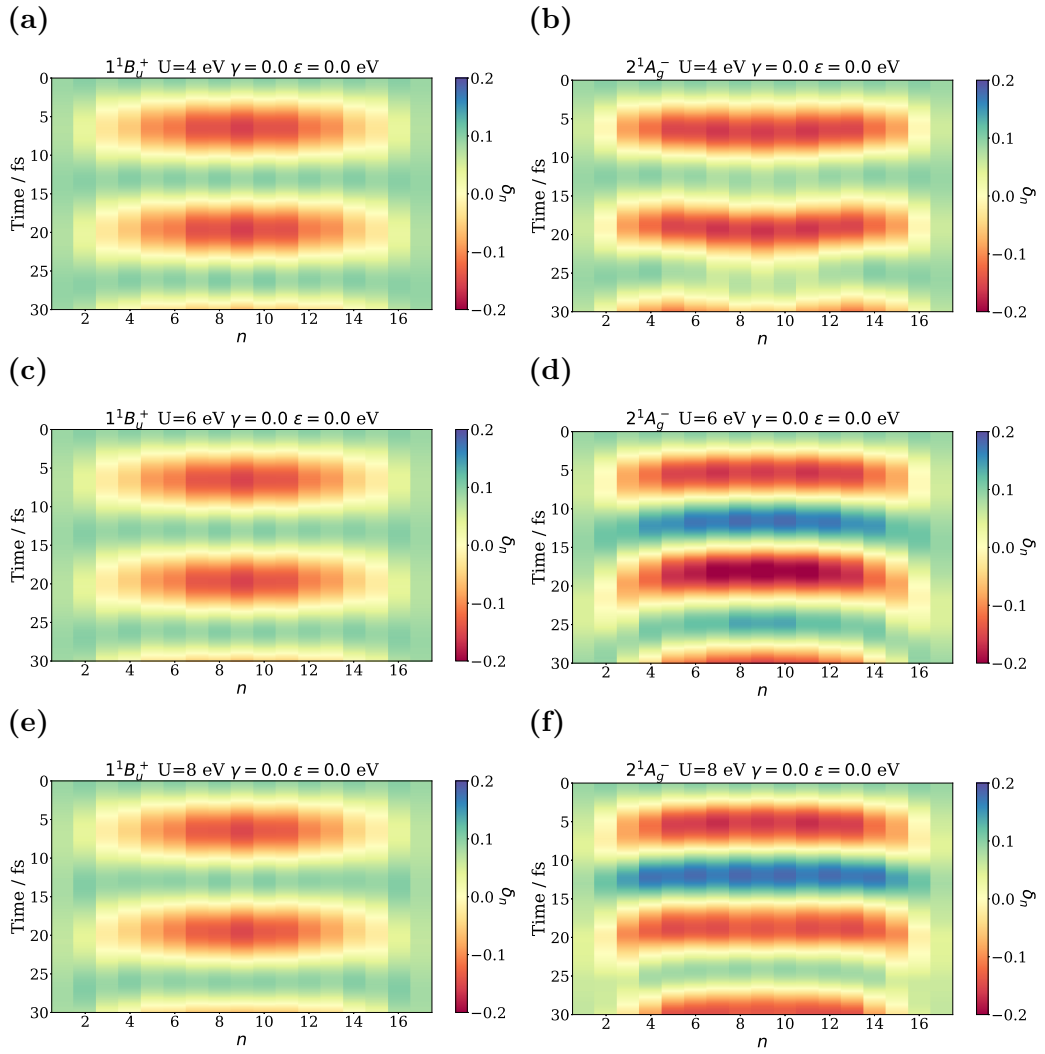


Figure 5.C.1: Staggered bond dimerisation of the $1^1B_u^+$ and $2^1A_g^-$ states without symmetry breaking, for $U = 4, 6, 8$ eV.

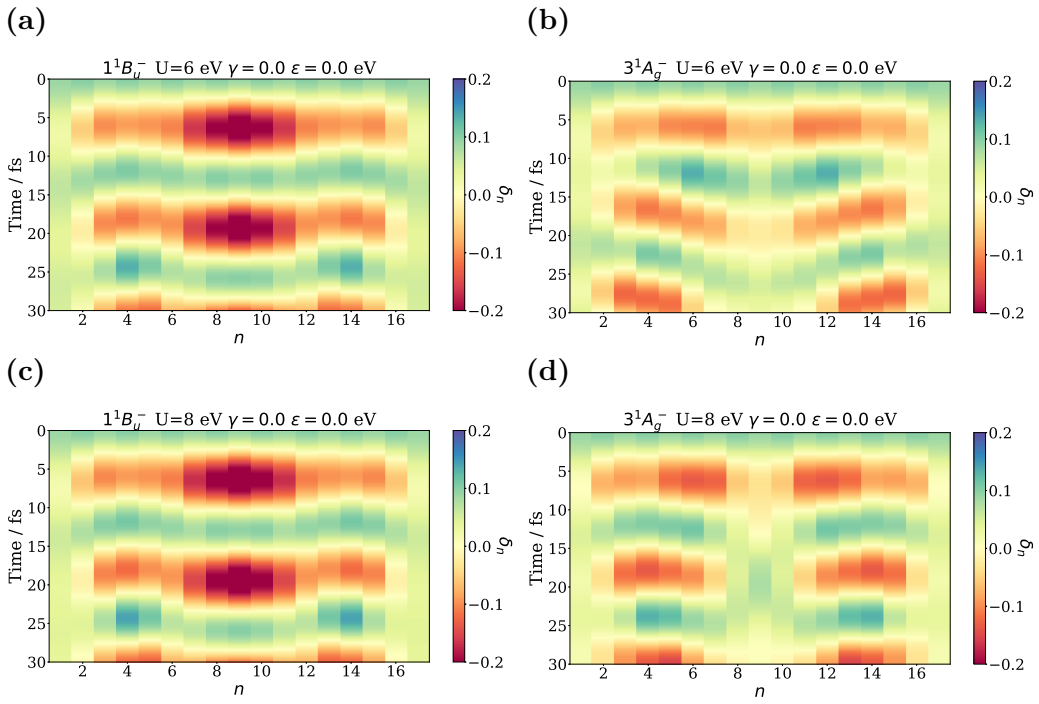


Figure 5.C.2: Staggered bond dimerisation of the $1^1B_u^-$ and $3^1A_g^-$ states without symmetry breaking, for $U = 6, 8$ eV.

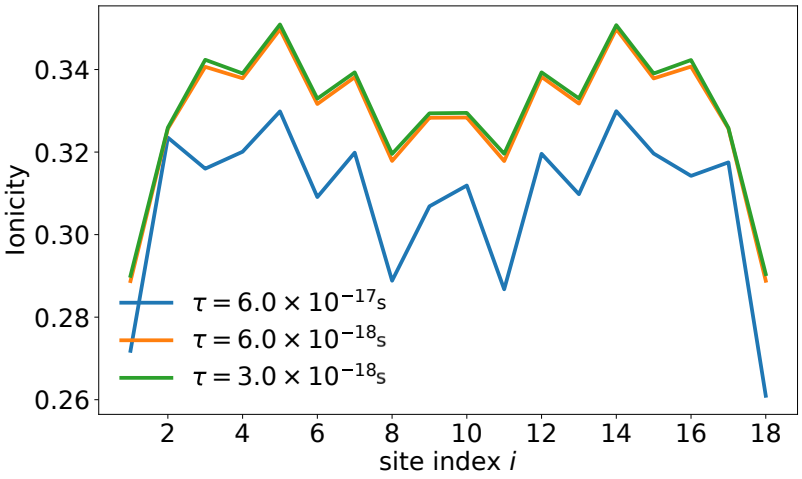
5.D Convergence of t-DMRG parameters

In this appendix, the values of the t-DMRG parameters used in this thesis are justified. For simplicity, all results presented in this section correspond to evolution of the $1^1B_u^+$ state with symmetry breaking ($\epsilon = 1$ eV). t-DMRG calculation suffer from two main errors: truncation error, which is reduced by increasing the number of retained states, m, during the DMRG truncation steps , and Trotter error, which is reduced by used a smaller time-step, τ.

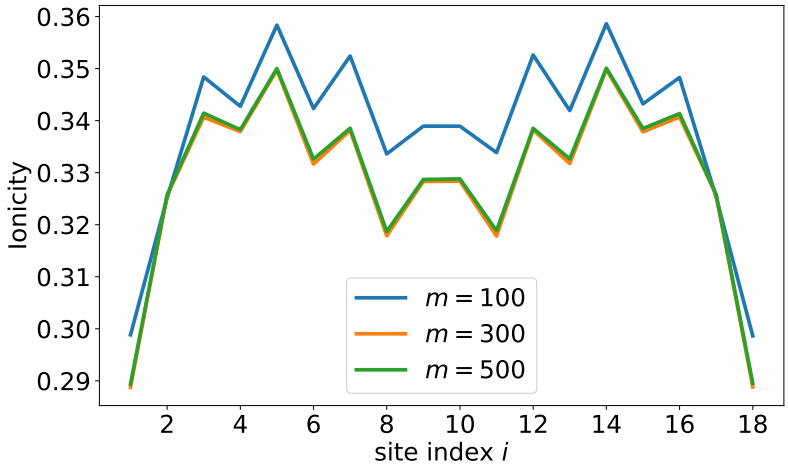
We first consider the Ehrenfest dynamics of the UV-Peierls model used in Chapter 5. Dynamics of a short chain of $L = 6$, for which all states can be retained, were first considered. The results converged for a time step of $\tau = 3 \times 10^{-18}$ s. Then, a larger system, $L = 18$, was simulated, with $m = 500$ value to reduce truncation error. The ionicity after 60 fs, across the chain for a range of time steps in shown in Fig. 5.D.1a. The curves for a time steps of $\tau = 3 \times 10^{-18}$ s and $\tau = 6 \times 10^{-18}$ s lie on top of one another, confirming that $\tau = 3 \times 10^{-18}$ s produces accurate results.

Finally, the number of retained states is tuned so that the computational cost of the calculations is made as small as possible. Dynamics with time step of $\tau = 3 \times 10^{-18}$ s and a range of m values is shown in Fig. 5.D.1b and it can be seen that an m value of 300 produces both accurate results while minimizing computational cost.

Similar analysis was carried out for a chain of length, $L = 14$, however this time with quantized phonons were used. The results are shown in Fig. 5.D.2. Again it was found that results are converged for $m = 300$ and $\tau = 3 \times 10^{-18}$ s.

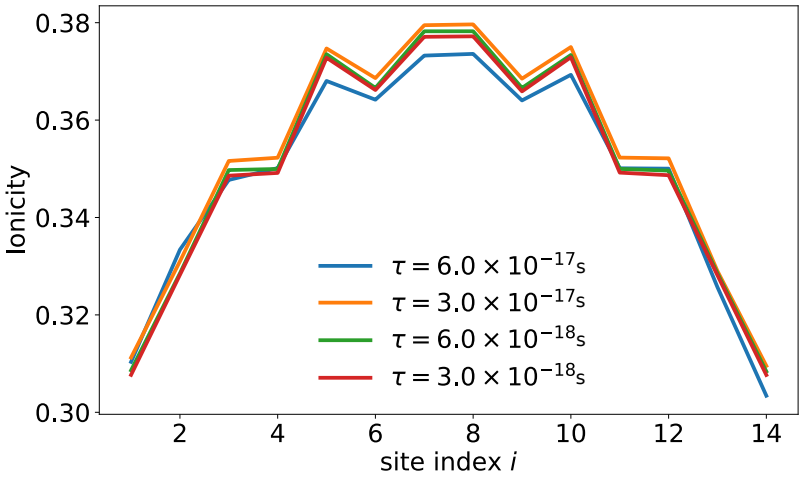


(a)

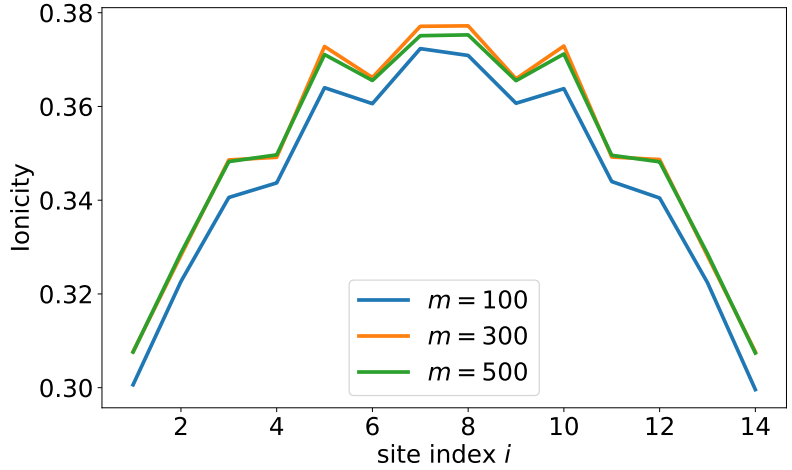


(b)

Figure 5.D.1: The ionicity after 60 fs for a 18 site UV-Peierls model evolved under Ehrenfest dynamics for a range of **(a)** time-step values, τ and **(b)** retained state values, m



(a)



(b)

Figure 5.D.2: The ionicity after 60 fs for a 14 site quantised UV-Peierls for a range of **(a)** time-step values, τ in seconds and **(b)** retained state values, m

Chapter 6

State interconversion: Quantised nuclear degrees of freedom

In the previous chapter, the initial state interconversion process of singlet fission was investigated by treating nuclear motion classically with the evolution of the photoexcited state described using Ehrenfest dynamics. While the results give a qualitative picture of which states the photoexcited state crossed over to, once the nuclear wavepacket has passed through a conical intersection, the motion is no longer accurately described due to the mean-field nature of Ehrenfest dynamics.[152,153] In addition, exciton decoherence which can be induced by electron-phonon coupling is absent in Ehrenfest dynamics.[154,156,162] To overcome these failures, in this chapter nuclear motion is treated quantum mechanically.

The classical treatment of nuclear motion also leads to the self-localisation of excitations. Self-localisation means that a particle (i.e. a spin, electron or hole) becomes coupled to a local distortion of nuclei. A distinction needs to be made between self-trapping and self-localisation. Self-trapping refers to the coupling of local displacements to a particle, which together delocalise across the chain; solitons are examples of self-trapping. Self-localisation can be seen as a consequence of the adiabatic treatment of the nuclei. Since nuclei distortions can now only be repre-

sented by one configuration, the particle coupled to that distortion is localised in space, leading to static solitons such as found with the Hellmann-Feynman procedure (Chapter 4).

Self-localisation leads to the saturation of excitation energy with inverse conjugation as seen in Chapter 4. Treating the nuclear degrees of freedom quantum mechanically leads to the formation of a band of solitons,[58] and quantum fluctuations mean that the particles are no longer localised. This can lead to an increase in soliton width, which is most evident for the triplet $1^3B_u^-$ state.[125] However, there remains an additional mechanism of localisation: disorder. Even with a weak amount of disorder, excitations will localise in a one-dimensional system and indeed disorder is expected to be the dominant cause of localisation.[163] Taking this into account, the work presented in the previous chapter can still be viewed as qualitative. This is because localisation was included albeit via the classical treatment of nuclear motion and not via disorder.[129,163]

Using the observables established in the previous chapter, state interconversion is investigated with the quantum treatment of phonons. Quantization of the nuclear degrees of freedom is presented in the next section, followed by a discussion of which initial state to use in the dynamics. Finally the results of t-DMRG evolutions are discussed.

6.1 Quantisation of the nuclear degrees of freedom

In this chapter the fully quantized UV-Peierls model is used, which is given by

$$\hat{H} = \hat{H}_{UV} + \hat{H}_{el-ph} + \hat{H}_{ph}, \tag{6.1}$$

where H_{UV} is the electronic UV-Hamiltonian (extended-Hubbard) as given in Eq. (5.2). H_{el-ph} is as given previously in Eq. (5.4), while the phonon Hamiltonian is

$$\hat{H}_{ph} = \sum_{n=1}^{N} \frac{P_n^2}{2M} + \frac{K}{2} \sum_{n=1}^{N} \left(u_{n+1} - u_n\right)^2, \tag{6.2}$$

where M is the CH unit mass, K is the elastic spring constant. These are used to define a bare phonon frequency $\omega_0 = \sqrt{K/M}$.

Taking the limit $M \to \infty$ ($\omega_0 \to 0$), leads to the Born-Oppenheimer treatment of nuclear degrees of freedom. However, when quantising the nuclear degrees of freedom, it is useful to rewrite Eq. (6.2), as

$$\hat{H}_{ph} = \sum_{n=1}^{N} \frac{P_n^2}{2M} + \frac{\tilde{K}}{2} \sum_{n=1}^{N} u_n^2 - \frac{\tilde{K}}{2} \sum_{n=1}^{N-1} u_{n+1} u_n, \tag{6.3}$$

where $\tilde{K} = 2K$. The first two terms on the right-hand side of Eq. (6.3), represent N independent harmonic oscillators with spring constant $\tilde{K}$, while the final term represents coupling between nearest neighbour oscillators.

A system of independent oscillators can be diagonalised by the introduction of the phonon creation and annihilation operators given as,[164]

$$\hat{b}_n^\dagger = \left(\frac{M\omega_D}{2\hbar}\right)^{1/2} u_n - i \left(\frac{1}{2M\hbar\omega_D}\right)^{1/2} P_n, \tag{6.4}$$

and

$$\hat{b}_n = \left(\frac{M\omega_D}{2\hbar}\right)^{1/2} u_n + i \left(\frac{1}{2M\hbar\omega_D}\right)^{1/2} P_n, \tag{6.5}$$

respectively, where $\hat{b}_n^\dagger$ ($\hat{b}_n$) creates (destroys) a quantum of energy, $\hbar\omega_D$, in the harmonic oscillator at site n, where

$$\omega_D = \sqrt{\tilde{K}/M} = \sqrt{2}\omega_0. \tag{6.6}$$

The inverse definitions are

$$u_n = \left(\frac{\hbar}{2M\omega_D}\right)^{1/2} (\hat{b}_n^\dagger + \hat{b}_n), \tag{6.7}$$

and

$$P_n = i\left(\frac{M\hbar\omega_D}{2}\right)^{1/2} (\hat{b}_n^\dagger - \hat{b}_n). \tag{6.8}$$

Using these expressions and substituting them into Eq. (6.3) leads to

$$H_{ph} = \hbar\omega_D \sum_n \left(\hat{b}_n^\dagger \hat{b}_n + \frac{1}{2}\right) - \frac{\hbar}{2}\omega_D \sum_n \hat{B}_{n+1}\hat{B}_n, \tag{6.9}$$

where,

$$\hat{B}_n = \frac{(\hat{b}_n^\dagger + \hat{b}_n)}{\sqrt{2}} \tag{6.10}$$

is the dimensionless displacement of the nth oscillator. H_{el-ph} is therefore,

$$H_{el-ph} = tg \sum_{n\sigma} \left(\hat{B}_{n+1} - \hat{B}_n\right) \left(\hat{c}_{n+1\sigma}^\dagger \hat{c}_{n\sigma} + \hat{c}_{n\sigma}^\dagger \hat{c}_{n+1\sigma}\right), \tag{6.11}$$

where g is an electron-phonon coupling constant and given by $\left(\frac{\hbar\omega_D \pi\lambda}{4t}\right)^{1/2}$, with $\lambda = 0.248$. Dynamics of the full Hamiltonian were calculated using the t-DMRG method. However, this means that the number of phonon levels per site will need to be fixed. In this work one phonon degree of freedom was used per site. This value was used primarily to ensure the dynamics could be calculated in a timely manner with modest computational resources, and, in addition, only a 14 site chain was considered for similar reasons. Previous work on π-conjugated systems has found that this limited number of phonons can give qualitative insights.[165,166] In this work, $\hbar\omega_0 = 0.2$ eV, $g = 0.18/\sqrt{(2)} \approx 0.127$ and $t = 2.4$ eV. A discussion of why these parameters were chosen is presented in Appendix 6.A.

6.1.1 Initial state

In the previous chapter the vertical $1^1B_u^+$ state was used as the initial state for interconversion dynamics. However, when using the quantized UV-Peierls Hamiltonian and targeting excited states by symmetry, the calculated states have a relaxed geometry ($\langle B_n \rangle$) and it is not possible to calculate a vertical eigenstate. To probe a vertically-excited, initial state, we first start from first-order time-dependent perturbation theory, which states that the first order correction to the wavefunction evolving under Hamiltonian, $H = H_0 + V(t)$, is given by ($\hbar = 1$)

$$|\Psi(t)\rangle^{(1)} = -\frac{i}{\hbar}\int_0^t e^{-iH_0(t-t')}V(t')e^{-iH_0t'}\,|GS\rangle\,dt', \tag{6.12}$$

where H_0 is unperturbed quantum UV-Peierls Hamiltonian, and $V(t)$ is the perturbation. Suppose that the perturbation was due to the interaction of the molecule with an electric field produced from a narrow instantaneous pulse applied at $t' = 0$. Therefore,

$$V(t') = -\hat{\mu}\epsilon(t') = -\hat{\mu}\epsilon_{\mathbf{0}}\delta(t'), \tag{6.13}$$

where ϵ_0 is the instantaneous electric field, $\hat{\mu}$ is the transition dipole operator given by

$$\hat{\mu} = \sum_i x_i(\hat{N}_i - 1), \tag{6.14}$$

where x_i is the displacement of the nuclei i relative to the centre of the chain, and $(\hat{N}_i - 1)$ is the density operator. Eq. (6.12) becomes

$$\begin{aligned} |\Psi(t)\rangle^{(1)} &= \frac{i}{\hbar} e^{-iH_0 t} \hat{\mu} \epsilon_{\mathbf{0}} |GS\rangle \\ |\Psi(t)\rangle^{(1)} &= \frac{i}{\hbar} e^{-iH_0 t} \underbrace{\sum_n |\Psi_n\rangle \langle \Psi_n|}_{\hat{1}} \hat{\mu} \epsilon_{\mathbf{0}} |GS\rangle \\ |\Psi(t)\rangle^{(1)} &= \frac{i\epsilon_0}{\hbar} e^{-iH_0 t} \sum_n \mu_{0n} e^{-iE_n t} |\Psi_n\rangle \,, \end{aligned} \tag{6.15}$$

where $|\Psi_n\rangle$ is an eigenstate of the Hamiltonian H_0 with energy E_0, and $\mu_{n0} = \langle \Psi_n | \hat{\mu} | GS \rangle$ is the transition dipole moment connecting the ground state with state Ψ_n. The final line of Eq. (6.15) indicates that the probability that an eigenstate, $|\Psi_n\rangle$ contributing to the initial state $|\Psi(0)\rangle$ is proportional to $|\mu_{n0}|^2$.

Therefore the initial state $|\mu\rangle$ is defined as

$$|\mu\rangle = \hat{\mu} |GS\rangle \,. \tag{6.16}$$

This state is included in the reduced density matrix during the initial finite DMRG routine and represents a photoexcited state produced by a narrow instantaneous pulse at $t = 0$.[167] Calculating $|\mu\rangle$ only requires knowledge of the ground state and therefore symmetries are not needed. In this chapter, dynamics are started from the vertical $|\mu\rangle$ state and the relaxed $1^1B_u^+$ state. For the $|\mu\rangle$ state the symmetry-breaking terms was included in the finite DMRG routine, i.e. when calculating the ground state; while for the $1^1B_u^+$ state, symmetry breaking was introduced to the Hamiltonian only during dynamics.

6.2 Results

6.2.1 Dynamics of photoexcited state

The ionicity and spin-spin correlation were used to keep track of the electron-hole and spin-wave character of both the evolving photoexcited state and the relaxed $1^1B_u^+$ state. Again, the effect of the environment of state interconversion was probed by varying the Coulombic parameter. This work focused on the cases: $U = 6$ eV, when Ehrenfest results indicated state interconversion was from $1^1B_u^+ \rightarrow 2^1A_g^-$, and $U = 8$ eV, when state interconversion was found to be $1^1B_u^+ \rightarrow 3^1A_g^-$.

Ionicity

As with the Ehrenfest dynamics, the ionicity of the evolving states was found to decrease when symmetry breaking is introduced, as illustrated in Fig. 6.1. This indicates that the evolving state loses electron-hole character and gains character of a different state.

It is worth noting that the $|\mu\rangle$ state has a lower initial ionicity than the relaxed $1^1B_u^+$ state. Considering that the $|\mu\rangle$ state is a superposition of ${}^1B_u^+$ states (of which $1^1B_u^+$ dominates), the higher energy ${}^1B_u^+$ states, therefore, have a lower ionicity than the $1^1B_u^+$ state and may indeed have some degree of spin-wave character.

For $U = 6$ eV and $\epsilon = 1.0$ eV, the ionicity decreases very rapidly in the first ≈ 20 fs, and then then oscillates with a time period close to the nuclear frequency. This is the case for both the $|\mu\rangle$ and $1^1B_u^+$ states. This oscillation is absent when $U = 8.0$ eV. To explain this oscillation, the energy gaps between interconverting states need to be considered. When $U = 6$ eV the $1^1B_u^+$ and $2^1A_g^-$ states are closer in energy, facilitating state interconversion, $1^1B_u^+ \rightarrow 2^1A_g^-$. After the rapid state interconversion (≈ 20 fs), some portion of the evolving state returns to the

initial bright state and the ionicity increases. This would suggest that, when there is sufficient symmetry breaking, electron-phonon non-adiabatic couplings are the main drivers of state interconversion and dynamics, rather than the symmetry breaking term. When $U = 8$ eV, state interconversion is predominately in one direction, and a steady decrease in the ionicity is observed. The energy gap between the destination triplet-pair state and the $1^1B_u^+$ state is larger and back-conversion is hindered. As the transition energy between a pair of stationary states increases, the magnitude and period of the Rabi-type oscillations of the non-stationary state decreases.

Spin-spin correlation

In discussing the spin-spin correlations, two types are considered: long-range correlations, for which the distance between spins is greater than half the chain length, e.g. for $N = 14$ S_1S_{14}, and mid-range correlations where the distance between spins is just less than half the chain length, e.g. for $N = 14$ S_1S_6. Triplet-pair states generally show strong long-range correlations as was found in Chapter 4.

If singlet fission proceeds on a single chain, when the triplet-pair state ($^1(TT)$) decoheres into two separate triplets (T_1+T_1), the long-range correlations will vanish. However mid-range spin-spin correlations should be present in both the $^1(TT)$ and $T_1 + T_1$ states.

Comparable to the results from the previous chapter, changing the Coulombic parameter, U, distinctly affects the evolution of the spin-spin correlations as illustrated in Figs. 6.2- 6.3. When $U = 6$ eV and with $\epsilon = 1$ eV, there is a large increase in magnitude of the $\langle S_1S_{14}\rangle$ correlation (the correlations become negative), in contrast to when $U = 8$ eV. Furthermore when $U = 6$ eV, after the $\langle S_1S_{14}\rangle$ correlation initially increases in magnitude, there is a distinct oscillation of the order of the phonon frequency, similar to what was found for the ionicity. This again

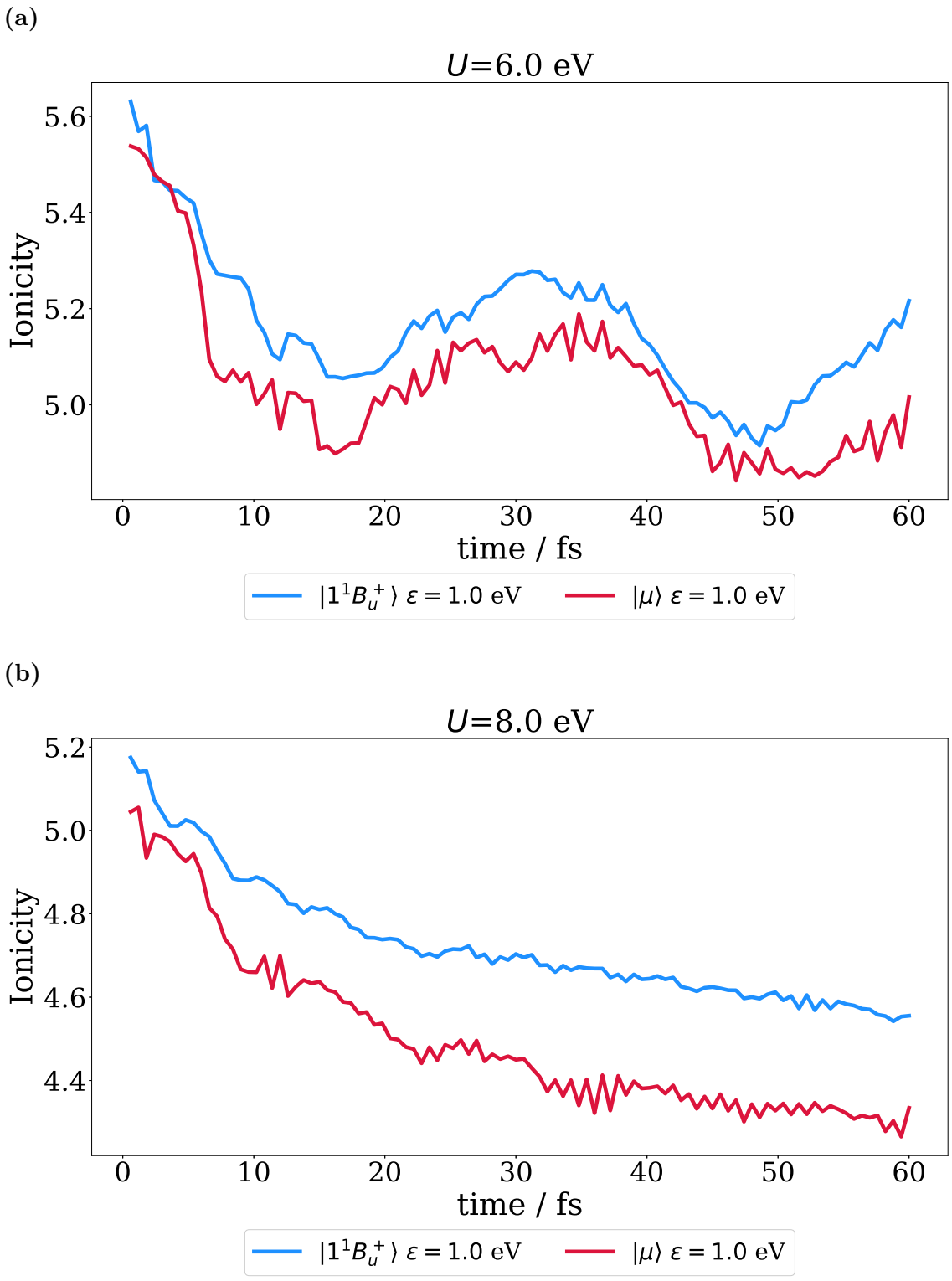


Figure 6.1: Evolution of ionicity of the $|\mu\rangle$ and $1^1B_u^+$ states for (a) $U = 6$ and (b) $U = 8$.

indicates there is a continued phonon driven coupling between the photoexcited and triplet-pair states.

In the first 5 fs of the dynamics, the $|\mu\rangle$ state rapidly shows fluctuations in the long-range correlations, this is regardless of symmetry breaking and is absent in the $1^1B_u^+$ results (Fig. 6.2a). The fluctuation is larger when $U = 8$ eV. However, from 10 fs onwards the $|\mu\rangle$ and $1^1B_u^+$ correlations broadly evolve in the same manner for the same symmetry breaking and Coulombic value. This suggests that the initial fluctuation is due to higher ${}^1B_u^+$ contributions to the $|\mu\rangle$ state which rapidly relaxes, and as such the $|\mu\rangle$ state is well approximated by the $1^1B_u^+$ state, despite having different starting geometries.

Turning now to the mid-range correlations, there is a large increase in the magnitude of the $\langle S_1 S_6\rangle$ correlations only when $U = 8.0$ eV. In addition the increase in magnitude is larger for the $|\mu\rangle$ compared to the $1^1B_u^+$ state. During the first 5 fs of the dynamics while the $1^1B_u^+$ state and $|\mu\rangle$ results differ, there are no sharp fluctuations in the correlations as was found with the long-range correlations.

Again, the $U = 8$ eV correlations broadly follow the $U = 8$ eV ionicity results, with no distinct oscillations that could be attributed to the phonon frequency.

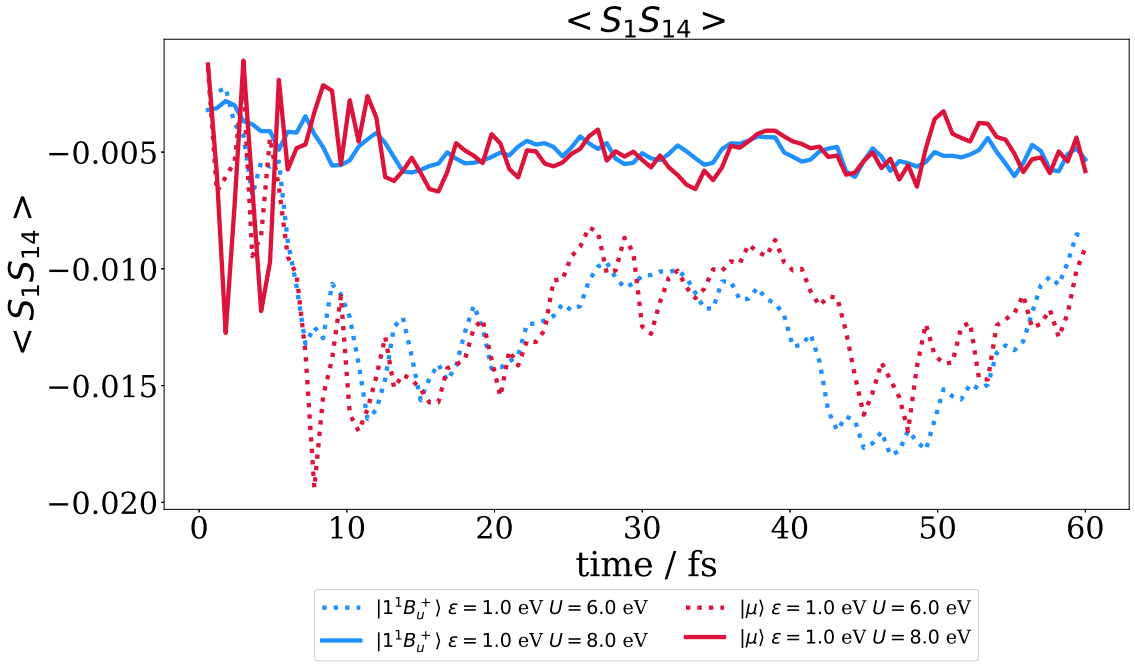
Additional long-range ($S_1 S_{12}$) and mid-range ($S_3 S_8$) correlations were also analysed and followed the same patterns. However they have not been included here to prevent the repetition of discussion.

Overall, we see that U affects the state interconversion. When $U = 6$ eV, the increase in the long-range spin correlations indicates that state interconversion takes place from the $1^1B_u^+$ state to the $2^1A_g^-$ state, as was found before.

However when $U = 8$ eV, rather than a gain in long-range correlations there is an increase in mid-range correlations. At this Coulomb parameter value, the change in spin-spin correlation pattern does not resemble that of the $2^1A_g^-$ state or the

$3^1A_g^-$ and $1^1B_u^-$ states, when compared to single state Ehrenfest dynamics results. The use of quantum phonons may mean that the solitons of the $1^1B_u^-$ and $3^1A_g^-$ states are not "self-trapped" which would lead to a different spin-spin correlation pattern, it would be expected that this effect would be most substantial for the six soliton $3^1A_g^-$ state. However, it is not possible to calculate the relaxed $3^1A_g^-$ state with quantum phonons in a DMRG framework. This is due to the $^1A_g^-$ sector being populated by many vibrationally hot $1^1A_g^-$ states.

(a)



(b)

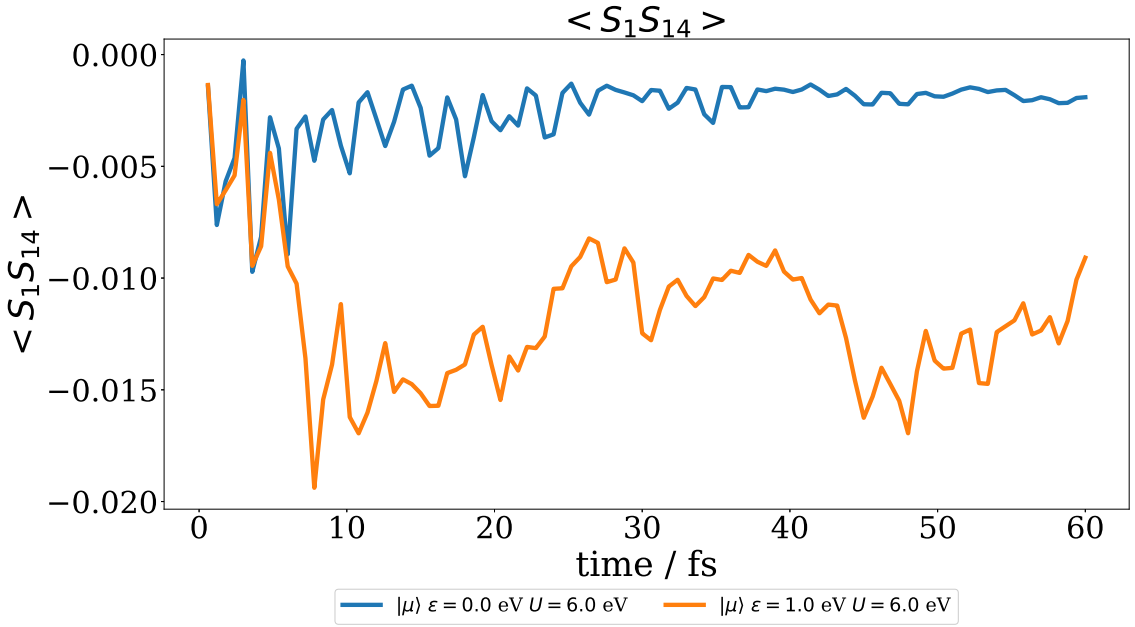


Figure 6.2: Evolution of the long-range spin-spin correlations $\langle S_1 S_{14} \rangle$ for the $1^1B_u^+$and $|\mu\rangle$ states, (a) with symmetry breaking ($U = 6$ eV is denoted by a dashed line, $U = 8$ eV is denoted by a solid line) and (b) without.

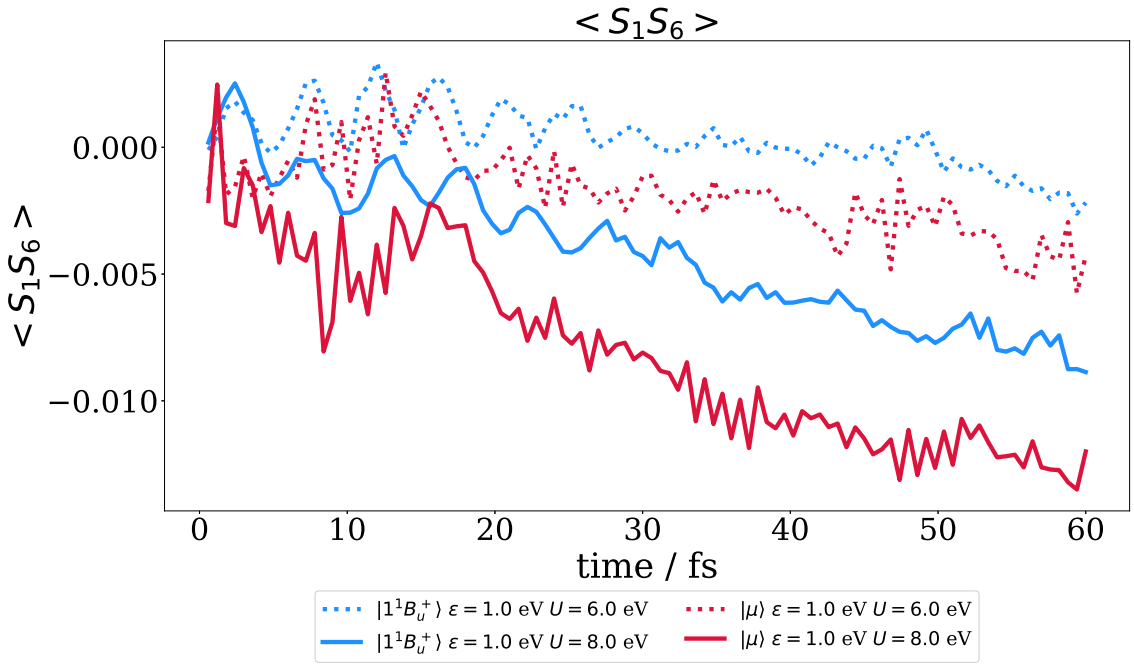


Figure 6.3: Evolution of the mid-range spin-spin correlation, $\langle S_1 S_6 \rangle$ for the $1^1B_u^+$and $|\mu\rangle$ states with symmetry breaking. $U = 6$ eV is denoted by a dashed line, $U = 8$ eV is denoted by a solid line.

6.3 Summary

This aim of this work was to correct for some of the deficiencies of treating state-interconversion with Ehrenfest dynamics. Overall the results with quantum phonons agreed qualitatively with the Ehrenfest results. State interconversion was found to be ultrafast occurring in 10 fs. In addition, changing the Coulombic parameter affected which state the photoexcited and $1^1B_u^+$ states evolved into. When $U = 6$ eV, the spin-spin correlation indicated that the initial state evolved into the $2^1A_g^-$ state, as was previously found.

However, when $U = 8$ eV, state interconversion still takes place, but the destination state could not be ascertained. Increasing U saw the magnitude of long-range correlations decrease; this may also be due in part to greater decoherence facilitated by electron-phonon coupling. Additionally, we also saw a gain in mid-range spin-spin correlations, this could be interpreted as increasing U leads to a more fissioned triplet-pair state, as long-range correlation are diminished while mid-range

spin correlations increase, which could be attributed to individual triplets. Thus, at higher U singlet fission proceeds directly from a $1^1B_u^+$ state to a configuration of individual triplets. This agrees with experimental work on carotenoids in solution which found that individual triplets formed directly from the $1^1B_u^+$ state, however, only detected intermolecular singlet fission.[59] Further work is needed to interpret the state interconversion results with quantised phonons.

Appendices

6.A Parameter selection for the quantum UV-Peierls model

The quantum UV-Peierls model is given by

$$\hat{H} = \hat{H}_{UV} + \hat{H}_{el-ph} + \hat{H}_{ph} \tag{6.17}$$

where $\hat{H}_{UV}$ is the electronic UV-Hamiltonian (extended-Hubbard) as given in Eq. (5.2). The phonon term is given by

$$\hat{H}_{ph} = \hbar\omega_D \sum_n \left(\hat{b}_n^\dagger \hat{b}_n + \frac{1}{2}\right) - \frac{\hbar}{2}\omega_D \sum_n \hat{B}_{n+1}\hat{B}_n \tag{6.18}$$

where $\omega_D = \sqrt{2}\omega_0$ and the electron phonon coupling is given by

$$\hat{H}_{el-ph} = tg \sum_{n\sigma} \left(\hat{B}_{n+1} - \hat{B}_n\right)(\hat{c}_{n+1\sigma}^\dagger \hat{c}_{n\sigma} + \hat{c}_{n\sigma}^\dagger \hat{c}_{n+1\sigma}\Big) \tag{6.19}$$

and g is the electronic-phonon coupling $\left(\frac{\hbar\omega_D \pi\lambda}{4t}\right)^{1/2}$. In this thesis a t value of 2.4 eV was used. This value for the hopping integral was introduced by Mazumdar and Chandross[122] to model *screened* polyacetylene and has since been used to study a number of π-conjugated systems.[73]

The bare phonon frequency, ω_0 was parametrized by typical C-C bond stretching frequencies and a value of $\hbar\omega = 0.2$ eV[168] was used.

To parametrize g, we are interested in values when the $1^1B_u^+$ and $2^1A_g^-$ state are

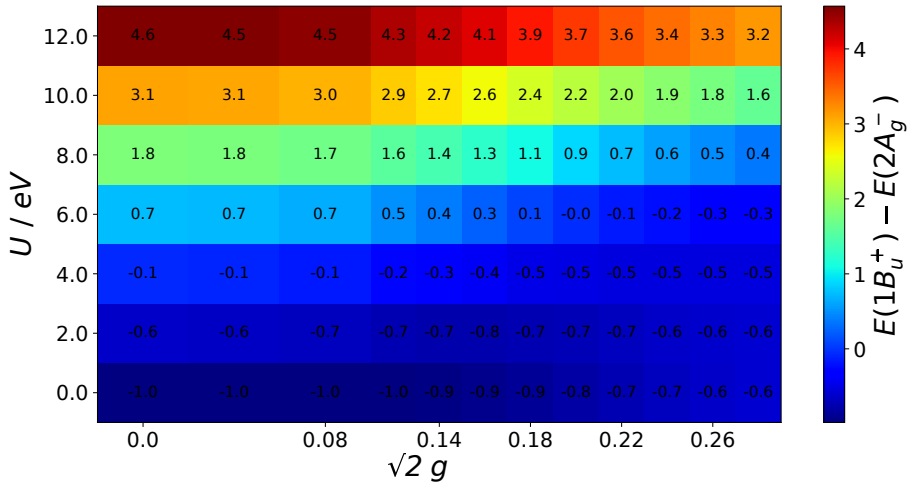


Figure 6.A.1: Energy difference of the $2^1A_g^-$and $1^1B_u^+$ states for a range of U and g.

close in energy. To find such a value, the ground states of the quantum UV-Peierls model for a range of U and g values were calculated. In the quantum model, it is not possible to target the $2^1A_g^-$ state, due to the number of vibrational hot ground state replicas. To target the $2^1A_g^-$ state, we must use a classical nuclei model. We replace the phonon displacement operator, B_n in Eq. (6.20) with expectation for the ground state, $\langle B_n \rangle$. Thus the electronic-phonon coupling becomes

$$\hat{H}_{el-ph} = tg \sum_{n\sigma} \left(\left\langle \hat{B}_{n+1} \right\rangle - \left\langle \hat{B}_n \right\rangle \right) (\hat{c}^\dagger_{n+1\sigma} \hat{c}_{n\sigma} + \hat{c}^\dagger_{n\sigma} \hat{c}_{n+1\sigma}) \tag{6.20}$$

By doing this, the energy of excited states in an approximate ground state geometry can be calculated. In Fig. 6.A.1 the difference between the vertical energy for the $1^1B_u^+$ and $2^1A_g^-$ states is shown as a function of U and g for a 14 site chain.

Parameters of $g = 0.18/\sqrt{2}$ and $U = 6, 8$ eV were selected. When $g = 0.18/\sqrt{2}$ and $U = 6.0$ eV, the vertical energy difference between the states was found to be small. Increasing U to 8 eV increased the energetic gap between the states and this allows us to investigate two different electronic environments.

Chapter 7

Conclusions and future work

Singlet fission represents one avenue to increase solar cell efficiency, which is necessary to mitigate the effects of climate change.[3] This work investigated one of the most promising classes of singlet fission materials; linear π-conjugated polyenes,[20] and focussed on the first step of singlet fission, state interconversion, where an optically excited singlet state undergoes internal conversion to a triplet-pair state; studying dynamics and the nature of the triplet-pair states involved.

Using the Pariser-Parr-Pople-Parr Hamiltonian, the $2^1A_g^-$, $1^1B_u^-$ and $3^1A_g^-$ singlet states and the $1^5A_g^-$ quintet state were investigated as candidate triplet-pair states for the singlet fission intermediates. Using energetic criteria for intramolecular singlet fission in linear systems: for a state to be involved in singlet fission on a chain of length N, its relaxed energy must be greater than the twice the triplet excitation energy for a chain of length $N/2$, and a state's vertical energy must lie above the relaxed $1^1B_u^+$ energy to allow efficient crossover. It was found that the $1^1B_u^-$ and $3^1A_g^-$ states are candidates for the SF $^1(TT)$ intermediate state.

Furthermore, the nature of the triplet-pair states was investigated by considering the solitonic structure, spin-spin correlations and triplet overlap of the wavefunction. The $2^1A_g^-$, $1^1B_u^-$ and $1^5A_g^-$ states were found to be four soliton states, while the $3^1A_g^-$ state was has a more complicated geometry.

Considering spin-spin correlations, energy in the long-chain limit and electron-hole wave functions, it was found the $2^1A_g^-$, $3^1A_g^-$and $1^1B_u^-$ states belong to the same

family of states with the $3^1A_g^-$ and $1^1B_u^-$ states being higher momentum replicas of the $2^1A_g^-$ state. This result has fundamental consequences for the design of singlet fission materials. The $2^1A_g^-$ state is a bound triplet-pair state from which singlet fission does not occur. Instead, the $2^1A_g^-$ surface acts as a relaxation channel to the ground state. For an efficient SF linear polyene material, relaxation from the higher momentum replicas, $1^1B_u^-$ and $3^1A_g^-$ states to the $2^1A_g^-$ state, must be hindered.

Having established the $3^1A_g^-$ and $1^1B_u^-$ states as candidate SF intermediate states, the dynamics of the state interconversion process were investigated. In the extended polyene systems, singlet fission is intramolecular. However, in shorter polyene systems, intramolecular singlet fission has only been observed in the photosynthetic reaction centres of cyanobacteria.[145,146] In solution, singlet fission is detected only when carotenoids aggregates form.

To investigate how changes in the electronic environment affect singlet fission, the Coulombic parameter, U, was varied. Ehrenfest dynamics of the vertical $1^1B_u^+$ state were calculated with a symmetry breaking end-site on-site energy term introduced to allow dynamics to explore all states and simulate state interconversion. The dynamics were calculated using time-dependent density matrix renormalisation group. Using the spin-spin correlations, ionicity, and the staggered bond dimerisation, the character of the state was tracked. It was found that for all U values, state interconversion was fast with the evolving state gaining some triplet-pair state character in the first 10 fs. When $U = 4$ eV, the energy gap between the $1^1B_u^+$ and $2^1A_g^-$ states is small, and the evolving state oscillated between $2^1A_g^-$ and $1^1B_u^+$ character. Increasing U to 6 eV, the $2^1A_g^-$ relaxed energy falls below the relaxed $1^1B_u^+$ energy, while the $3^1A_g^-$ relaxed energy lies below the vertical $1^1B_u^+$ energy. Despite this, the calculated observables indicated that the evolving state gains $2^1A_g^-$ and not $3^1A_g^-$ character.

However, when the Coulombic parameter, U, was increased further to 8 eV, the state interconversion is found to be from the $1^1B_u^+$ state to the $3^1A_g^-$ state. Thus varying the electronic environment has a strong influence on state interconversion.

These results further the claim that the $3^1A_g^-$ state could be the $^1(TT)$ intermediate of singlet fission, with conversion to the $2^1A_g^-$ state representing a competing relaxation pathway. To the author's knowledge, these results are the first calculations of state interconversion from the $1^1B_u^+$ state to the $3^1A_g^-$ state. This pathway may only be available to carotenoids in photosynthetic bacteria and may help explain why carotenoid intramolecular singlet fission is only observed in that environment.

Ehrenfest dynamics, however, has drawbacks including an inadequate description of dynamics that pass through a conical intersection and the self-localisation of solitons along the chain; these deficiencies are due to the mean-field treatment of the electron-phonon interactions and the classical treatment of the nuclei. To probe the robustness of the Ehrenfest results, UV-Peierls dynamics were calculated with quantised nuclear degrees of freedom. These results again indicate that state interconversion is ultrafast, and additionally, it was still found that changing the Coulombic parameter changes the destination state. For $U = 4$, 6 eV state interconversion takes place between the $1^1B_u^+$ and $2^1A_g^-$ states. Furthermore, when U is increased to 8 eV, the dynamics lead to crossover to a different state to the $2^1A_g^-$state. However, identifying this new destination state proved difficult, as with quantised nuclear degrees of freedom it is not possible to target excited states in the ^1A_g sector (as there are multiple hot ground state eigenstates). The $3^1A_g^-$ state, in particular, is the sum of a number of different triplet-triplet combinations and as such its spin-spin correlation and relaxed geometry will likely differ from those found via the classical treatment of nuclei.

Future work

When investigating singlet fission intermediates, this thesis primarily considered singlet triplet-pair states. However, it was also found that the $1^5A_g^-$ quintet state can be regarded as an unbound pair of T_1 triplets. The possibility of a quintet singlet fission intermediate has been experimentally investigated in acene SF materials. Through the use of time-resolved electron spin resonance spectroscopies,

a quintet SF intermediate has been detected in bridged pentacene dimers.[43] Spin mixing can couple the $2^1A_g^-$ and $1^5A_g^-$ states,[19,44] for example, and this may mean a mixed quintet state may represent an alternative SF channel (to the $3^1A_g^-$) in linear polyenes. Physically motivated spin-mixing terms include intra-triplet and inter-triplet dipole terms,[19] a study could investigate how these terms can induce static couplings between the quintet and triplet-pair eigenstates and the effect of these terms on dynamics.

To further investigate the Ehrenfest results, the overlap of the evolving states with triplet-pair eigenstates, such as the $2^1A_g^-$, $3^1A_g^-$ states, should be calculated to obtain quantum yields; this can be achieved in two ways. Firstly the desired eigenstate can be rotated and included in the reduced density matrix during the evolution with the t-DMRG scheme. An alternative option is to find eigenstates of the evolving Hamiltonian on-the-fly. This would allow us to quantify better the $1^1B_u^+ \rightarrow 2^1A_g^-$ and $1^1B_u^+ \rightarrow 3^1A_g^-$ state interconversion for $U = 6$ and 8 eV, respectively.

In addition to state interconversion, the spin decoherence step of SF will be explored following work by Marcus and Barford[33] which investigated a Heisenberg spin-chain. Their work linked the populations of the triplet-pair eigensector with a quantum information framework and probed spin-decoherence of triplet-pair states. Using a more realistic UV-Peierls model, a full description of singlet fission beyond state interconversion and including spin decoherence is the ultimate aim of the proposed work.

In this thesis, dynamics with quantised nuclear degrees of freedom were additionally used to treat state interconversion. To implement this model, only one phonon was allowed per site, and while this can give qualitative insight, there will be errors due to the truncation of single-site phonon states. To overcome this without significantly increasing computational cost, the mixed quantum Ehrenfest method developed by Mannouch should be used.[165,166] In this technique, the nuclei's centre of masses are evolved classically; however, quantum fluctuations around the evolving centre are included. Using this method, a more accurate description of the state

interconversion process can be achieved. This future work will use and build upon, the t-DMRG code developed for the work presented in this thesis.

Bibliography

(1) IPCC, *Global warming of 1.5°C*, 2018.

(2) MacKay, D. J. C. Sustainable Energy - without the hot air. *UIT Cambridge Ltd.* **2008**.

(3) Rao, A.; Friend, R. H. Harnessing singlet exciton fission to break the Shockley–Queisser limit. *Nature Reviews Materials* **2017**, *2*, 17063.

(4) Lewis, N. S. Research opportunities to advance solar energy utilization. *Science* **2016**, *351*.

(5) Shockley, W.; Queisser, H. J. Detailed balance limit of efficiency of p-n junction solar cells. *Journal of Applied Physics* **1961**, *32*, 510–519.

(6) Hanna, M. C.; Nozik, A. J. Solar conversion efficiency of photovoltaic and photoelectrolysis cells with carrier multiplication absorbers. *Journal of Applied Physics* **2006**, *100*, 074510.

(7) Smith, M. B.; Michl, J. Singlet fission. *Chemical Reviews* **2010**, *110*, 6891–6936.

(8) Ehrler, B.; Musselman, K. P.; Böhm, M. L.; Friend, R. H., et al. Hybrid pentacene/a-silicon solar cells utilizing multiple carrier generation via singlet exciton fission. *Applied Physics Letters* **2012**, *101*, 153507.

(9) Casanova, D. Theoretical Modeling of Singlet Fission. *Chemical Reviews* **2018**, *118*, 7164–7207.

(10) Thompson, N. J.; Congreve, D. N.; Goldberg, D.; Menon, V. M., et al. Slow light enhanced singlet exciton fission solar cells with a 126% yield of electrons per photon. *Applied Physics Letters* **2013**, *103*, 263302.

(11) Congreve, D. N.; Lee, J.; Thompson, N. J.; Hontz, E., et al. External quantum efficiency above 100% in a singlet-exciton-fission-based organic photovoltaic cell. *Science* **2013**, *340*, 334–337.

(12) Lee, S.; Hwang, D.; Jung, S. I.; Kim, D. Electron Transfer from Triplet State of TIPS-Pentacene Generated by Singlet Fission Processes to CH3NH3PbI3 Perovskite. *Journal of Physical Chemistry Letters* **2017**, *8*, 884–888.

(13) Yu, J.; Fu, L. M.; Yu, L. J.; Shi, Y., et al. Carotenoid Singlet Fission Reactions in Bacterial Light Harvesting Complexes As Revealed by Triplet Excitation Profiles. *Journal of the American Chemical Society* **2017**, *139*, 15984–15993.

(14) Klenina, I. B.; Makhneva, Z. K.; Moskalenko, A. A.; Gudkov, N. D., et al. Singlet-triplet fission of carotenoid excitation in light-harvesting LH2 complexes of purple phototrophic bacteria. *Biochemistry (Moscow)* **2014**, *79*, 235–241.

(15) Cogdell, R. J.; Land, E. J.; Truscott, T. G. The Triplet Extinction Coefficients of Some Bacterial Carotenoids. *Photochemistry and Photobiology* **1983**, *38*, 723–725.

(16) Gradinaru, C. C.; Kennis, J. T.; Papagiannakis, E.; Van Stokkum, I. H., et al. An unusual pathway of excitation energy deactivation in carotenoids: Singlet-to-triplet conversion on an ultrafast timescale in a photosynthetic antenna. *Proceedings of the National Academy of Sciences of the United States of America* **2001**, *98*, 2364–2369.

(17) Musser, A. J.; Liebel, M.; Schnedermann, C.; Wende, T., et al. Evidence for conical intersection dynamics mediating ultrafast singlet exciton fission. *Nature Physics* **2015**, *11*, 352–357.

(18) Weiss, L. R.; Bayliss, S. L.; Kraffert, F.; Thorley, K. J., et al. Strongly exchange-coupled triplet pairs in an organic semiconductor. *Nature Physics* **2017**, *13*, 176–181.

(19) Musser, A. J.; Al-Hashimi, M.; Heeney, M.; Clark, J. Heavy-atom effects on intramolecular singlet fission in a conjugated polymer. *Journal of Chemical Physics* **2019**, *151*, 044902.

(20) Miyata, K.; Conrad-Burton, F. S.; Geyer, F. L.; Zhu, X. Y. Triplet Pair States in Singlet Fission. *Chemical Reviews* **2019**, *119*, 4261–4292.

(21) Kim, H.; Zimmerman, P. M. Coupled double triplet state in singlet fission. *Physical Chemistry Chemical Physics* **2018**, *20*, 30083–30094.

(22) Sanders, S. N.; Pun, A. B.; Parenti, K. R.; Kumarasamy, E., et al. Understanding the Bound Triplet-Pair State in Singlet Fission. *Chem* **2019**, *5*, 1988–2005.

(23) Marian, C. M. Spin-orbit coupling and intersystem crossing in molecules. *Wiley Interdisciplinary Reviews: Computational Molecular Science* **2012**, *2*, 187–203.

(24) Singh, S.; Jones, W. J.; Siebrand, W.; Stoicheff, B. P., et al. Laser generation of excitons and fluorescence in anthracene crystals. *The Journal of Chemical Physics* **1965**, *42*, 330–342.

(25) Swenberg, C. E.; Stacy, W. T. Bimolecular radiationless transitions in crystalline tetracene. *Chemical Physics Letters* **1968**, *2*, 327–328.

(26) Johnson, R. C.; Merrifield, R. E. Effects of magnetic fields on the mutual annihilation of triplet excitons in anthracene crystals. *Physical Review B* **1970**, *1*, 896–902.

(27) Smith, M. B.; Michl, J. Recent Advances in Singlet Fission. *Annual Review of Physical Chemistry* **2013**, *64*, 361–386.

(28) Lanzani, G.; Stagira, S.; Cerullo, G.; De Silvestri, S., et al. Triplet exciton generation and decay in a red polydiacetylene studied by femtosecond spectroscopy. *Chemical Physics Letters* **1999**, *313*, 525–532.

(29) Lanzani, G.; Cerullo, G.; Zavelani-Rossi, M.; De Silvestri, S., et al. Triplet-exciton generation mechanism in a new soluble (red-phase) polydiacetylene. *Physical Review Letters* **2001**, *87*, 1874021–1874024.

(30) Musser, A. J.; Al-Hashimi, M.; Maiuri, M.; Brida, D., et al. Activated singlet exciton fission in a semiconducting polymer. *Journal of the American Chemical Society* **2013**, *135*, 12747–12754.

(31) Teichen, P. E.; Eaves, J. D. Collective aspects of singlet fission in molecular crystals. *Journal of Chemical Physics* **2015**, *143*, 044118.

(32) Scholes, G. D. Correlated Pair States Formed by Singlet Fission and Exciton-Exciton Annihilation. *Journal of Physical Chemistry A* **2015**, *119*, 12699–12705.

(33) Marcus, M.; Barford, W. Triplet-triplet decoherence in singlet fission. *Physical Review B* **2020**, *102*, 035134.

(34) Piland, G. B.; Burdett, J. J.; Dillon, R. J.; Bardeen, C. J. Singlet fission: From coherences to kinetics. *Journal of Physical Chemistry Letters* **2014**, *5*, 2312–2319.

(35) Burdett, J. J.; Bardeen, C. J. Quantum beats in crystalline tetracene delayed fluorescence due to triplet pair coherences produced by direct singlet fission. *Journal of the American Chemical Society* **2012**, *134*, 8597–8607.

(36) Pensack, R. D.; Ostroumov, E. E.; Tilley, A. J.; Mazza, S., et al. Observation of Two Triplet-Pair Intermediates in Singlet Exciton Fission. *Journal of Physical Chemistry Letters* **2016**, *7*, 2370–2375.

(37) Stern, H. L.; Cheminal, A.; Yost, S. R.; Broch, K., et al. Vibronically coherent ultrafast triplet-pair formation and subsequent thermally activated dissociation control efficient endothermic singlet fission. *Nature Chemistry* **2017**, *9*, 1205–1212.

(38) Krishnapriya, K. C.; Musser, A. J.; Patil, S. Molecular Design Strategies for Efficient Intramolecular Singlet Exciton Fission. *ACS Energy Letters* **2019**, *4*, 192–202.

(39) Kollmar, C.; Sixl, H.; Benk, H.; Denner, V., et al. Theory of two coupled triplet states - electrostatic energy splittings. *Chemical Physics Letters* **1982**, *87*, 266–270.

(40) Stern, H. L.; Musser, A. J.; Gelinas, S.; Parkinson, P., et al. Identification of a triplet pair intermediate in singlet exciton fission in solution. *Proceedings of the National Academy of Sciences of the United States of America* **2015**, *112*, 7656–7661.

(41) Chan, W. L.; Ligges, M.; Jailaubekov, A.; Kaake, L., et al. Observing the multiexciton state in singlet fission and ensuing ultrafast multielectron transfer. *Science* **2011**, *334*, 1541–1545.

(42) Walker, B. J.; Musser, A. J.; Beljonne, D.; Friend, R. H. Singlet exciton fission in solution. *Nature Chemistry* **2013**, *5*, 1019–1024.

(43) Tayebjee, M. J.; Sanders, S. N.; Kumarasamy, E.; Campos, L. M., et al. Quintet multiexciton dynamics in singlet fission. *Nature Physics* **2017**, *13*, 182–188.

(44) Merrifield, R. E. Magnetic effects on triplet exciton interactions. *Pure and Applied Chemistry* **1971**, *27*, 481–498.

(45) Basel, B. S.; Zirzlmeier, J.; Hetzer, C.; Phelan, B. T., et al. Unified model for singlet fission within a non-conjugated covalent pentacene dimer. *Nature Communications* **2017**, *8*, 1–8.

(46) Zimmerman, P. M.; Bell, F.; Casanova, D.; Head-Gordon, M. Mechanism for singlet fission in pentacene and tetracene: From single exciton to two triplets. *Journal of the American Chemical Society* **2011**, *133*, 19944–19952.

(47) Berkelbach, T. C.; Hybertsen, M. S.; Reichman, D. R. Microscopic theory of singlet exciton fission. I. General formulation. *Journal of Chemical Physics* **2013**, *138*, 114102.

(48) Berkelbach, T. C.; Hybertsen, M. S.; Reichman, D. R. Microscopic theory of singlet exciton fission. II. Application to pentacene dimers and the role of superexchange. *Journal of Chemical Physics* **2013**, *138*, 114103.

(49) Scholes, G. D.; Fleming, G. R.; Olaya-Castro, A.; Van Grondelle, R. Lessons from nature about solar light harvesting. *Nature Chemistry* **2011**, *3*, 763–774.

(50) Liebel, M.; Schnedermann, C.; Kukura, P. Vibrationally coherent crossing and coupling of electronic states during internal conversion in β-carotene. *Physical Review Letters* **2014**, *112*, 198302.

(51) Wilson, M. W.; Rao, A.; Clark, J.; Kumar, R. S. S., et al. Ultrafast dynamics of exciton fission in polycrystalline pentacene. *Journal of the American Chemical Society* **2011**, *133*, 11830–11833.

(52) Ramanan, C.; Smeigh, A. L.; Anthony, J. E.; Marks, T. J., et al. Competition between singlet fission and charge separation in solution-processed blend films of 6,13-bis(triisopropylsilylethynyl)pentacene with sterically-encumbered perylene-3,4:9,10-bis(dicarboximide)s. *Journal of the American Chemical Society* **2012**, *134*, 386–397.

(53) Lukman, S.; Chen, K.; Hodgkiss, J. M.; Turban, D. H., et al. Tuning the role of charge-transfer states in intramolecular singlet exciton fission through side-group engineering. *Nature Communications* **2016**, *7*, 1–13.

(54) Sanders, S. N.; Kumarasamy, E.; Pun, A. B.; Trinh, M. T., et al. Quantitative Intramolecular Singlet Fission in Bipentacenes. *Journal of the American Chemical Society* **2015**, *137*, 8965–8972.

(55) Lim, S. H.; Bjorklund, T. G.; Spano, F. C.; Bardeen, C. J. Exciton Delocalization and Superradiance in Tetracene Thin Films and Nanoaggregates. *Physical Review Letters* **2004**, *92*, 107402.

(56) Khan, S.; Mazumdar, S. Free Triplets Versus Bound Triplet-Triplet Biexciton in Intramolecular Singlet Fission Materials: Structure-Property Correlations. *Journal of Physical Chemistry C* **2020**, *124*, 1171–1177.

(57) Rademaker, H.; Hoff, A. J.; Van Grondelle, R.; Duysens, L. N. Carotenoid triplet yields in normal and deuterated Rhodospirillum rubrum. *Biochimica et Biophysica Acta - Bioenergetics* **1980**, *592*, 240–257.

(58) Barford, W., *Electronic and optical properties of conjugated polymers*; Oxford University Press: 2013.

(59) Musser, A. J.; Maiuri, M.; Brida, D.; Cerullo, G., et al. The nature of singlet exciton fission in carotenoid aggregates. *Journal of the American Chemical Society* **2015**, *137*, 5130–5139.

(60) Ren, J.; Peng, Q.; Zhang, X.; Yi, Y., et al. Role of the Dark 2Ag State in Donor–Acceptor Copolymers as a Pathway for Singlet Fission: A DMRG Study. *The Journal of Physical Chemistry Letters* **2017**, *8*, 2175–2181.

(61) Polívka, T.; Sundström, V. Dark excited states of carotenoids: Consensus and controversy. *Chemical Physics Letters* **2009**, *477*, 1–11.

(62) Trinh, M. T.; Zhong, Y.; Chen, Q.; Schiros, T., et al. Intra- to intermolecular singlet fission. *Journal of Physical Chemistry C* **2015**, *119*, 1312–1319.

(63) Wang, C.; Tauber, M. J. High-yield singlet fission in a zeaxanthin aggregate observed by picosecond resonance Raman spectroscopy. *Journal of the American Chemical Society* **2010**, *132*, 13988–13991.

(64) Klenina, I. B.; Makhneva, Z. K.; Moskalenko, A. A.; Kuzmin, A. N., et al. Singlet-triplet excitation fission in light-harvesting complexes of photosynthetic bacteria and in isolated carotenoids. *Biophysics (Russian Federation)* **2013**, *58*, 43–50.

(65) Papagiannakis, E.; Das, S. K.; Gall, A.; Van Stokkum, I. H., et al. Light harvesting by carotenoids incorporated into the B850 light-harvesting complex from Rhodobacter sphaeroides R-26.1: Excited-state relaxation, ultrafast triplet formation, and energy transfer to bacteriochlorophyll. *Journal of Physical Chemistry B* **2003**, *107*, 5642–5649.

(66) Klenina, I. B.; Makhneva, Z. K.; Moskalenko, A. A.; Gudkov, N. D., et al. Singlet-triplet fission of carotenoid excitation in light-harvesting LH2 complexes of purple phototrophic bacteria. *Biochemistry (Moscow)* **2014**, *79*, 235–241.

(67) Rademaker, H.; Hoff, A. J.; Van Grondelle, R.; Duysens, L. N. Carotenoid triplet yields in normal and deuterated Rhodospirillum rubrum. *Biochimica et Biophysica Acta - Bioenergetics* **1980**, *592*, 240–257.

(68) Wang, C.; Schlamadinger, D. E.; Desai, V.; Tauber, M. J. Triplet excitons of carotenoids formed by singlet fission in a membrane. *ChemPhysChem* **2011**, *12*, 2891–2894.

(69) Mukhopadhyay, T.; Musser, A. J.; Puttaraju, B.; Dhar, J., et al. Is the Chemical Strategy for Imbuing "Polyene" Character in Diketopyrrolopyrrole-Based Chromophores Sufficient for Singlet Fission? *Journal of Physical Chemistry Letters* **2017**, *8*, 984–991.

(70) Musser, A. J.; Al-Hashimi, M.; Heeney, M.; Clark, J. Heavy-atom effects on intramolecular singlet fission in a conjugated polymer. *The Journal of Chemical Physics* **2019**, *151*, 044902.

(71) Zhai, Y.; Sheng, C.; Vardeny, Z. V. Singlet fission of hot excitons in π -conjugated polymers. *Philosophical Transactions of the Royal Society A: Mathematical, Physical and Engineering Sciences* **2015**, *373*, 20140327.

(72) Busby, E.; Xia, J.; Wu, Q.; Low, J. Z., et al. A design strategy for intramolecular singlet fission mediated by charge-transfer states in donor-acceptor organic materials. *Nature Materials* **2015**, *14*, 426–433.

(73) Barford, W.; Bursill, R. J.; Lavrentiev, M. Y. Density-matrix renormalization-group calculations of excited states of linear polyenes. *Physical Review B - Condensed Matter and Materials Physics* **2001**, *63*, 195108.

(74) Tavan, P.; Schulten, K. Electronic excitations in finite and infinite polyenes. *Physical Review B* **1987**, *36*, 4337–4358.

(75) Schmidt, M.; Tavan, P. Electronic excitations in long polyenes revisited. *Journal of Chemical Physics* **2012**, *136*.

(76) Peierls, R. E., *Quantum theory of solids*; Clarendon Press: 2001.

(77) Roth, S.; Carroll, D., *One-dimensional metals: Conjugated polymers, organic crystals, carbon nanotubes and graphene*; Wiley: 2015.

(78) Anderson, P. W., *Basic notions of condensed matter physics*; CRC Press: 2018.

(79) Mazumdar, S.; Campbell, D. K. Broken Symmetries in a One-Dimensional Half-Filled Band with Arbitrarily Long-Range Coulomb Interactions. *Physical Review Letters* **1985**, *55*, 2067–2070.

(80) Ooshika, Y. A Semi-empirical Theory of the Conjugated Systems, III. Bond Alternation and Electron Fixation. *Journal of the Physical Society of Japan* **1959**, *14*, 747–749.

(81) Longuet-Higgins, H. C.; Salem, L. The Alternation of Bond Lengths in Long Conjugated Chain Molecules. *Proceedings of the Royal Society of London. Series A, Mathematical and Physical Sciences* **1959**, *251*, 172–185.

(82) Race, A.; Barford, W.; Bursill, R. J. Density matrix renormalization calculations of the relaxed energies and solitonic structures of polydiacetylene. *Physical Review B* **2003**, *67*, 245202.

(83) Bursill, R. J.; Barford, W. Electron-lattice relaxation, and soliton structures and their interactions in polyenes. *Physical Review Letters* **1999**, *82*, 1514–1517.

(84) Pople, J. A.; Walmsley, S. H. Bond alternation defects in long polyene molecules. *Molecular Physics* **1962**, *5*, 15–20.

(85) Affleck, I. In *Dynamical Properties of Unconventional Magnetic Systems*; Springer Netherlands: 1998, pp 123–131.

(86) White, S. R. Density matrix formulation for quantum renormalization groups. *Physical Review Letters* **1992**, *69*, 2863–2866.

(87) *Strongly Correlated Systems*; Avella, A., Mancini, F., Eds.; Springer Series in Solid-State Sciences, Vol. 176; Springer Berlin Heidelberg: Berlin, Heidelberg, 2013.

(88) White, S. R.; Feiguin, A. E. Real-time evolution using the density matrix renormalization group. *Physical Review Letters* **2004**, *93*, 076401.

(89) Daley, A. J.; Kollath, C.; Schollwöck, U.; Vidal, G. Time-dependent density-matrix renormalization-group using adaptive effective Hilbert spaces. *Journal of Statistical Mechanics: Theory and Experiment* **2004**, *2004*, 4005.

(90) White, S. R.; Noack, R. M. Real-space quantum renormalization groups. *Physical Review Letters* **1992**, *68*, 3487–3490.

(91) Wilson, K. G. The renormalization group: Critical phenomena and the Kondo problem. *Reviews of Modern Physics* **1975**, *47*, 773–840.

(92) Jeckelmann, E. Dynamical density-matrix renormalization-group method. *Physical Review B - Condensed Matter and Materials Physics* **2002**, *66*, 1–16.

(93) White, S. R.; Martin, R. L. Ab initio quantum chemistry using the density matrix renormalization group. *Journal of Chemical Physics* **1999**, *110*, 4127–4130.

(94) Legeza; Sólyom, J. Optimizing the density-matrix renormalization group method using quantum information entropy. *Physical Review B - Condensed Matter and Materials Physics* **2003**, *68*, 195116.

(95) Legeza; Röder, J.; Hess, B. A. Controlling the accuracy of the density-matrix renormalization-group method: The dynamical block state selection approach. *Physical Review B - Condensed Matter and Materials Physics* **2003**, *67*, 10.

(96) Chan, G. K. L.; Head-Gordon, M. Highly correlated calculations with a polynomial cost algorithm: A study of the density matrix renormalization group. *Journal of Chemical Physics* **2002**, *116*, 4462–4476.

(97) Lang, J.; Antalík, A.; Veis, L.; Brandejs, J., et al. Near-Linear Scaling in DMRG-Based Tailored Coupled Clusters: An Implementation of DLPNO-TCCSD and DLPNO-TCCSD(T). *Journal of Chemical Theory and Computation* **2020**, *16*, 3028–3040.

(98) Brandejs, J.; Višňák, J.; Veis, L.; Maté, M., et al. Toward DMRG-tailored coupled cluster method in the 4c-relativistic domain. *Journal of Chemical Physics* **2020**, *152*, 174107.

(99) Vidal, G. Efficient classical simulation of slightly entangled quantum computations. *Physical Review Letters* **2003**, *91*, 147902.

(100) Vidal, G. Efficient simulation of one-dimensional quantum many-body systems. *Physical Review Letters* **2004**, *93*, 040502.

(101) Schollwöck, U. The density-matrix renormalization group. *Reviews of Modern Physics* **2005**, *77*, 259–315.

(102) Schollwöck, U. The density-matrix renormalization group in the age of matrix product states. *Annals of Physics* **2011**, *326*, 96–192.

(103) Feynman, R. P., *Statistical mechanics: A set of lectures*; CRC Press: 2018.

(104) Noack, R. M.; White, S. R. In *Density-Matrix Renormalization*; Springer Berlin Heidelberg: 1999, pp 27–66.

(105) Feiguin, A. E. In *Strongly Correlated Systems*; Springer, Berlin, Heidelberg: 2013, pp 31–65.

(106) White, S. R. Spin Gaps in a Frustrated Heisenberg Model for CaV4O9. *Physical Review Letters* **1996**, *77*, 3633–3636.

(107) Eisert, J.; Cramer, M.; Plenio, M. B. Colloquium: Area laws for the entanglement entropy. *Reviews of Modern Physics* **2010**, *82*, 277–306.

(108) Hastings, M. B. An area law for one-dimensional quantum systems. *Journal of Statistical Mechanics: Theory and Experiment* **2007**, *2007*, 08024.

(109) Verstraete, F.; Cirac, J. I. Matrix product states represent ground states faithfully. *Physical Review B - Condensed Matter and Materials Physics* **2006**, *73*, 094423.

(110) Cazalilla, M. A.; Marston, J. B. Time-Dependent Density-Matrix Renormalization Group: A Systematic Method for the Study of Quantum Many-Body Out-of-Equilibrium Systems. *Physical Review Letters* **2002**, *88*, 4.

(111) Suzuki, M. Decomposition formulas of exponential operators and Lie exponentials with some applications to quantum mechanics and statistical physics. *Journal of Mathematical Physics* **1985**, *26*, 601–612.

(112) Trotter, H. F. On the Product of Semi-Groups of Operators. *Proceedings of the American Mathematical Society* **1959**, *10*, 545–551.

(113) Daley, A. J. Quantum trajectories and open many-body quantum systems. 2014.

(114) Ren, J.; Peng, Q.; Zhang, X.; Yi, Y., et al. Role of the Dark 2Ag State in Donor-Acceptor Copolymers as a Pathway for Singlet Fission: A DMRG Study. *Journal of Physical Chemistry Letters* **2017**, *8*, 2175–2181.

(115) Aryanpour, K.; Dutta, T.; Huynh, U. N.; Vardeny, Z. V., et al. Theory of Primary Photoexcitations in Donor-Acceptor Copolymers. *Physical Review Letters* **2015**, *115*, 267401.

(116) Aryanpour, K.; Shukla, A.; Mazumdar, S. Theory of singlet fission in polyenes, acene crystals, and covalently linked acene dimers. *Journal of Physical Chemistry C* **2015**, *119*, 6966–6979.

(117) Antognazza, M. R.; Lüer, L.; Polli, D.; Christensen, R. L., et al. Ultrafast excited state relaxation in long-chain polyenes. *Chemical Physics* **2010**, *373*, 115–121.

(118) Taffet, E. J.; Lee, B. G.; Toa, Z. S. D.; Pace, N., et al. Carotenoid Nuclear Reorganization and Interplay of Bright and Dark Excited States. *The Journal of Physical Chemistry B* **2019**, *123*, 8628–8643.

(119) Hashimoto, H.; Uragami, C.; Yukihira, N.; Gardiner, A. T., et al. Understanding/unravelling carotenoid excited singlet states. *Journal of The Royal Society Interface* **2018**, *15*, 20180026.

(120) Weiss, L. R.; Bayliss, S. L.; Kraffert, F.; Thorley, K. J., et al. Strongly exchange-coupled triplet pairs in an organic semiconductor. *Nature Physics* **2017**, *13*, 176–181.

(121) Ohno, K. Some remarks on the Pariser-Parr-Pople method. *Theoretica Chimica Acta* **1964**, *2*, 219–227.

(122) Chandross, M.; Mazumdar, S. Coulomb interactions and linear, nonlinear, and triplet absorption in poly(para-phenylenevinylene). *Physical Review B* **1997**, *55*, 1497–1504.

(123) Timár, M.; Barcza, G.; Gebhard, F.; Legeza, Ö. Optical phonons for Peierls chains with long-range Coulomb interactions. *Physical Review B* **2017**, *95*, 085150.

(124) Timár, M.; Barcza, G.; Gebhard, F.; Veis, L., et al. Hückel-Hubbard-Ohno modeling of Π-bonds in ethene and ethyne with application to: Trans - polyacetylene. *Physical Chemistry Chemical Physics* **2016**, *18*, 18835–18845.

(125) Barford, W.; Bursill, R. J.; Lavrentiev, M. Y. Breakdown of the adiabatic approximation in trans-polyacetylene. *Physical Review B - Condensed Matter and Materials Physics* **2002**, *65*, 1–5.

(126) Barford, W.; Bursill, R. J.; Smith, R. W. Theoretical and computational studies of excitons in conjugated polymers. *Physical Review B - Condensed Matter and Materials Physics* **2002**, *66*, 1152051–11520512.

(127) Kurashige, Y.; Nakano, H.; Nakao, Y.; Hirao, K. The π-π excited states of long linear polyenes studied by the CASCI-MRMP method. *Chemical Physics Letters* **2004**, *400*, 425–429.

(128) Wilson, M. W.; Rao, A.; Johnson, K.; Gélinas, S., et al. Temperature-independent singlet exciton fission in tetracene. *Journal of the American Chemical Society* **2013**, *135*, 16680–16688.

(129) Tozer, O. R.; Barford, W. Localization of large polarons in the disordered Holstein model. *Physical Review B - Condensed Matter and Materials Physics* **2014**, *89*, 155434.

(130) Heeger, A. J.; Kivelson, S.; Schrieffer, J. R.; Su, W. P. Solitons in conducting polymers. *Reviews of Modern Physics* **1988**, *60*, 781–850.

(131) Hayden, G. W.; Mele, E. J. Correlation effects and excited states in conjugated polymers. *Physical Review B* **1986**, *34*, 5484–5497.

(132) Su, W. P. Lattice relaxation of even-parity singlet excited states in polyacetylene and four-soliton bound state. *Physical Review Letters* **1995**, *74*, 1167–1170.

(133) Ball, R.; Su, W. P.; Schrieffer, J. R. Photoproduction of neutral verus charged solitons in trans (CH)x. *Le Journal de Physique Colloques* **1983**, *44*, C3–429–C3–435.

(134) Campbell, D. K.; Bishop, A. R. Solitons in polyacetylene and relativistic-field-theory models. *Physical Review B* **1981**, *24*, 4859–4862.

(135) Hu, W.; Chan, G. K.-L. Excited-State Geometry Optimization with the Density Matrix Renormalization Group, as Applied to Polyenes. *Journal of Chemical Theory and Computation* **2015**, *11*, 3000–3009.

(136) Harris, A. B. Alternating linear Heisenberg antiferromagnet: The exciton limit. *Physical Review B* **1973**, *7*, 3166.

(137) Uhrig, G. S.; Schulz, H. Magnetic excitation spectrum of dimerized antiferromagnetic chains. *Physical Review B - Condensed Matter and Materials Physics* **1996**, *54*, R9624–R9627.

(138) Barford, W. Excitons in conjugated polymers: A tale of two particles. *Journal of Physical Chemistry A* **2013**, *117*, 2665–2671.

(139) Barford, W.; Paiboonvorachat, N. Excitons in conjugated polymers: Wavefunctions, symmetries, and quantum numbers. *Journal of Chemical Physics* **2008**, *129*, 164716.

(140) Rissler, J.; Gebhard, F.; Jeckelmann, E. Optical excitations of Peierls-Mott insulators with bond disorder. *Journal of Physics Condensed Matter* **2005**, *17*, 4093–4110.

(141) Polak, D. W.; Musser, A. J.; Sutherland, G. A.; Auty, A., et al. Band-edge Excitation of Carotenoids Removes S* Revealing Triplet-pair Contributions to the S1 Absorption Spectrum. *arXiv 1901.04900* **2019**.

(142) Barford, W.; Paiboonvorachat, N.; Yaron, D. Second-order dispersion interactions in -conjugated polymers. *Journal of Chemical Physics* **2011**, *134*, 234101.

(143) Pandya, R.; Gu, Q.; Cheminal, A.; Chen, R. Y., et al. Optical Projection and Spatial Separation of Spin-Entangled Triplet Pairs from the S1 (21 Ag–) State of Pi-Conjugated Systems. *Chem* **2020**, *6*, 2826–2851.

(144) Cogdell, R. J.; Gardiner, A. T. Functions of Carotenoids in Photosynthesis. *Methods in Enzymology* **1993**, *214*, 185–193.

(145) Gradinaru, C. C.; Kennis, J. T.; Papagiannakis, E.; Van Stokkum, I. H., et al. An unusual pathway of excitation energy deactivation in carotenoids: Singlet-to-triplet conversion on an ultrafast timescale in a photosynthetic antenna. *Proceedings of the National Academy of Sciences of the United States of America* **2001**, *98*, 2364–2369.

(146) Yu, J.; Fu, L.-M.; Yu, L.-J.; Shi, Y., et al. Carotenoid Singlet Fission Reactions in Bacterial Light Harvesting Complexes As Revealed by Triplet Excitation Profiles. *Journal of the American Chemical Society* **2017**, *139*, 15984–15993.

(147) Wei, T.; Balevičius, V.; Polívka, T.; Ruban, A. V., et al. How carotenoid distortions may determine optical properties: Lessons from the orange carotenoid protein. *Physical Chemistry Chemical Physics* **2019**, *21*, 23187–23197.

(148) Kerfeld, C. A.; Melnicki, M. R.; Sutter, M.; Dominguez-Martin, M. A. Structure, function and evolution of the cyanobacterial orange carotenoid protein and its homologs. *New Phytologist* **2017**, *215*, 937–951.

(149) Kerfeld, C. A.; Sawaya, M. R.; Brahmandam, V.; Cascio, D., et al. The crystal structure of a cyanobacterial water-soluble carotenoid binding protein. *Structure* **2003**, *11*, 55–65.

(150) Hirsch, J. E. Charge-density-wave to spin-density-wave transition in the extended Hubbard model. *Physical Review Letters* **1984**, *53*, 2327–2330.

(151) Thompson, D. L.; Tully, J. C., *Nonadiabatic dynamics*; World Scientific: 1998.

(152) Bittner, E. R.; Rossky, P. J. Decoherent histories and nonadiabatic quantum molecular dynamics simulations. *Journal of Chemical Physics* **1997**, *107*, 8611–8618.

(153) Prezhdo, O. V.; Rossky, P. J. Mean-field molecular dynamics with surface hopping. *Journal of Chemical Physics* **1997**, *107*, 825–834.

(154) Mannouch, J. R.; Barford, W.; Al-Assam, S. Ultra-fast relaxation, decoherence, and localization of photoexcited states in π -conjugated polymers. *Journal of Chemical Physics* **2018**, *148*, 034901.

(155) Tozer, O. R.; Barford, W. Exciton dynamics in disordered poly(p-phenylenevinylene). 1. Ultrafast interconversion and dynamical localization. *Journal of Physical Chemistry A* **2012**, *116*, 10310–10318.

(156) Bittner, E. R.; Rossky, P. J. Quantum decoherence in mixed quantum-classical systems: Nonadiabatic processes. *The Journal of Chemical Physics* **1995**, *103*, 8130–8143.

(157) Kasai, Y.; Tamai, Y.; Ohkita, H.; Benten, H., et al. Ultrafast Singlet Fission in a Push-Pull Low-Bandgap Polymer Film. *Journal of the American Chemical Society* **2015**, *137*, 15980–15983.

(158) Prodhan, S.; Ramasesha, S. Exact wave packet dynamics of singlet fission in unsubstituted and substituted polyene chains within long-range interacting models. *Physical Review B* **2017**, *96*, 075142.

(159) Boman, M.; Bursill, R. J. Identification of excitons in conjugated polymers: A density-matrix renormalization-group study. *Physical Review B* **1998**, *57*, 15167–15176.

(160) Press, W. H.; Teukolsky, S. A.; Vettering, W. T.; Flannery, B. P., *NUMERICAL RECIPES The Art of Scientific Computing (3rd ed.)* Cambridge University Press: 2007.

(161) Verlet, L. Computer "experiments" on classical fluids. I. Thermodynamical properties of Lennard-Jones molecules. *Physical Review* **1967**, *159*, 98–103.

(162) Bedard-Hearn, M. J.; Larsen, R. E.; Schwartz, B. J. Mean-field dynamics with stochastic decoherence (MF-SD): A new algorithm for nonadiabatic mixed quantum/classical molecular-dynamics simulations with nuclear-induced decoherence. *Journal of Chemical Physics* **2005**, *123*, 234106.

(163) Barford, W.; Marcus, M.; Tozer, O. R. Polarons in π-Conjugated Polymers: Anderson or Landau? *Journal of Physical Chemistry A* **2016**, *120*, 615–620.

(164) Cohen-Tannoudji, C., *Quantum Mechanics*, 3rd; Wiley: 2019.

(165) Barford, W.; Mannouch, J. R. Torsionally induced exciton localization and decoherence in π -conjugated polymers. *Journal of Chemical Physics* **2018**, *149*, 214107.

(166) Mannouch, J. Exciton Dynamics in π-Conjugated Polymer Systems., DPhil Thesis, University of Oxford, 2019.

(167) Mukamel, S., *Principles of nonlinear optical spectroscopy,* Oxford University Press: New York, 1995.

(168) Karabunarliev, S.; Bittner, E. R. Polaron-excitons and electron-vibrational band shapes in conjugated polymers. *Journal of Chemical Physics* **2003**, *118*, 4291–4296.